The 2016 Nobel Prize in Physics was awarded to David Thouless, F. Haldane, and J. Kosterlitz for "theoretical discoveries of topological phase transitions and topological phases of matter." Since then, new opportunities have emerged, e.g., the robust edge states in topological insulators could significantly reduce heat generation due to their reduced resistance in electrical devices. In this dissertation we will focus, moreover, on the application of edge states as waveguides in an electron quantum optical setup. When the waveguides are attached to a chaotic cavity one expects the emergence of universal signatures of chaotic scattering, explored in this thesis for the first time in this topological scenario. We go beyond extensive simulations based on numerical techniques, and present semiclassical results. Together with experimental results, a holistic view of universal scattering correlators in various systems ranging from trivial to nontrivial insulators is presented here.

Universität Regensburg
UNIVERSITÄTSBIBLIOTHEK

ISBN 978-3-88246-477-1

Universal HOM-type S-matrix correlations in chaotic (non-)trivial topological insulators and an improved model for the AFM and STM characteristics in Cu-based quantum corrals

Andreas Bereczuk

Andreas Bereczuk

Universal HOM-type S-matrix correlations in chaotic (non-)trivial topological insulators and an improved model for the AFM and STM characteristics in Cu-based quantum corrals

Eine Publikation der
Universitätsbibliothek Regensburg

UNIVERSAL HOM-TYPE S-MATRIX CORRELATIONS IN CHAOTIC (NON-)TRIVIAL TOPOLOGICAL INSULATORS AND AN IMPROVED MODEL FOR THE AFM AND STM CHARACTERISTICS IN CU-BASED QUANTUM CORRALS

Dissertation

zur Erlangung des Doktorgrades
der Naturwissenschaften (Dr. rer. nat.)
der Fakultät für Physik
der Universität Regensburg

vorgelegt von

Andreas Bereczuk

aus
München

September 2022

Erstgutachter (Betreuer): Prof. Dr. Juan-Diego Urbina

Zweitgutachter: Prof. Dr. Andrea Donarini

Tag der Prüfung: 22. November 2022

ISBN (Print): 978-3-88246-477-1
ISBN (PDF): 978-3-88246-478-8

DOI: 10.5283/epub.53446
Link zur Online-Version: https://epub.uni-regensburg.de/53446

Satz und Layout: Andreas Bereczuk
Umschlaggestaltung: Peter Brünsteiner
Herstellung: Universitätsbibliothek Regensburg

Erscheinungsort: Regensburg, 2023
Druck und Bindung: Digital Print Group o. Schimek GmbH, Nürnberg

List of used acronyms:

1D – One-dimensional/one dimension
2D – Two-dimensional/two dimensions
3D – Three-dimensional/three dimensions
HOM – Hong-Ou-Mandel
QPC – Quantum point contact
EQO – Electron quantum optics
TI – Topological insulator
BHZ – Bernevig-Hughes-Zhang
RMT – Random matrix theory
GOE – Gaussian orthogonal ensemble
GUE – Gaussian unitary ensemble
COE – Circular orthogonal ensemble
CUE – Circular unitary ensemble
CSE – Circular symplectic ensemble
LDOS – Local density of states
STM – Scanning tunneling microscopy
AFM – Atomic force microscopy
DFT– Density matrix theory

Contents

1. Introduction

The measurement of the celebrated Hong-Ou-Mandel (HOM) effect was done in 1987 [1]. Two photons hit with a certain time delay between each other a beamsplitter and leave the setup at two possible exits. A detector is measuring the coinciding counts of both particles outgoing at the same exit. For large time delays the classical situation is present, namely 25% probability at each exit. In the setting of vanishing time delay, when both photons encounter the beamsplitter simultaneously, constructive interference leads to the boson-bunching: The probability of detecting both photons in one of two exists increases to 100%, the probability of detecting the photons in separate exists reduces to zero. This is caused by the vanishing phase aquired by the two-particle wavefunction when interchanging both photons, in other words the symmetric wavefunction for indistinguishable bosons. The classical to quantum transition appears when tuning the time delay between these extrema, yielding a probability form depending on the convolution of the shape of the two incoming wavepackets. Thereby, an crucial ingredient is the coherency and indistinguishability of both photons, originally established by a nonlinear crystal, where one photon entering the crystal split into two coherent photons exiting with frequencies adding up to the incoming one.
A plurality of alike measurements has been investigated with other quantum systems involving plasmons, phonons and even atoms [2–8]. A generalization to a multiparticle version in a multichannel setup includes the computation of the permanent (unsigned determinant) of a complex matrix and deals with an exponentially growing Hilbert space. Solving this so-called Boson-sampling problem by computing the output probability distribution is exponentially time or energy consuming for a classical computer, therefore it represents a promising candidate for demonstrating quantum supremacy [8, 9]. So far all (quasi)-particles obeyed the Bose-Einstein statistic. When considering electrons satisfying the Fermi-Dirac statistic, an anti-bunching effect due to the Pauli principle is expected. Here we focus ourselves into the topic of electron quantum optics (EQO), an emerging field with single to few electron excitations in a ballistic conductor attempting to transfer optical techniques to electronic setups. Beside quantum statistic effects, the presence of the Fermi sea and Coulomb interaction are the major differences in comparison to optical setups. Building EQO analogs to waveguides and beamsplitter was necessary to experimentally realize the electronic analogue of the HOM effect. It becomes apparent that working in the integer quantum Hall regime at very low temperatures combined with an adjusted quantum point contact (QPC) to achieve equal outgoing probabilities is a promising experimental setup [10]. The difficulty of generating two coherent and indistinguishable single-particle wave packets is in turn solved by triggered ac emitters.

As we will see, orientating towards chaotic systems can be achieved by replacing the QPC by a chaotic cavity. It is important to mention now, at first glance, chaos in quantum mechanics seems to be a contraction, e.g. due to the linearity of the Schrödinger equation. Nevertheless, quantum signatures of irregular motion are present, such as the spacing distribution of quantum energy levels: This distribution of a classically integrable generic[1] system follows an exponential function [16], the uncorrelated levels tend to cluster.
In contrast, classical chaotic systems experience correlated quantum energy levels with a repulsion strength depending on the underlying symmetry [17]. By generating random elements of the Hamiltonian matrix fulfilling only the specific symmetry, Random matrix theory (RMT) provides statistical accordance of the level spacing distributions [18]. For half-integer spin systems, in the presence of time-reversal symmetry with (without) spin-rotational symmetry the Hamiltonian is chosen real symmetric (self-dual) and is part of the Gaussian orthogonal (symplectic) ensemble (GOE/ GSE). In the case of broken time-reversal symmetry the Hamiltonian is hermitian and the ensemble class is called Gaussian unitary ensemble (GUE). A link to number theory is present, the pair correlation of zeros of Riemann's zeta function obeys the GUE statistic, too [17, 19]. The generation of Circular ensembles to simulate scattering (S)-matrices of chaotic systems provides us with the benefit of S-matrix statistics, with according classes, Circular orthogonal ensemble (COE), Circular symplectic ensemble (CSE) and Circular unitary ensemble (CUE) of importance in the following investigations [20–22]. The inclusion of energy-dependent Hamiltonians using the Heidelberg approach enables the study of energy-dependent four-point S-matrix correlators within RMT. These objects are relevant to consider, when the previously introduced HOM effect is modified by replacing the QPC by a chaotic cavity. The HOM form, previously given by the convolution of the two incoming wavepackets turns out to be dependent on the ratio of dwell time τ_D and wavepacket width τ_s and on the shape of the four-point S-matrix correlators [23]. For $\tau_D \gg \tau_s$, the wavepackets remain in the cavity for such long times, that the information of the wavepacket form is lost. Therefore, the HOM shape aquires a shape with exponential tails, independent on the incoming wavepacket form.
In this thesis we will focus on large systems compared to the Fermi wavelength and therefore the semiclassical approach is a powerful tool to invest these S-matrix correlators in the post-Ehrenfest time: Due to the saddle point approximation and the introduction of Sieber-Richter orbit pairs, the computation of these correlators is reduced to a combinatorial task [24–27]. Only for action differences in the order of $\hbar$ for each trajectory quadruplet the contribution is present after averaging, otherwise the strongly oscillating phase account for a vanishing term. The minimal action difference is achieved by separating the quadruplet structure in encounters and links, in the former trajectories differ slightly and in the latter at least two trajectories are identical, therefore no action difference is present. To address the computation semiclassically the generation of relevant quadruplets and their contribution to the four-point correlator is the relevant

[1] The term "generic" refers to an ongoing investigation of integrable systems providing level statistics not following the Berry-Tabor conjecture [11], the exponential form [12–15].

task, in which permutations play the major role. These permutations have an one-to-one correspondence to a pair of Young diagrams, well known in RMT [18,28]. For reasons of completeness here we want to mention the relation to the zero-dimensional sigma model of quantum field theory, in which the topological analogy is given between encounters and links with vertices and propagator lines of the Feynman diagrams [29–34].
The semiclassical and numerical analysis of S-matrix correlators is the main focus in chapter 2, delving the following main topics: The semiclassical analysis results in an approximated S-matrix correlator by a series expansion in orders of the inverse number of open modes. To which extend is this computational accessible? Is a numerical implementation of a chaotic cavity realizable, such that universal S-matrix correlators appear? In the extreme limit of few open modes is the semiclassical approximation still applicable and corresponding to numerical investigations? The extensive study includes due to an collaboration also correlator result by the Heidelberg approach and experimental realizations in microwave billiards.
In EQO the application of topology insulators (TIs) with helical edge states serving as waveguides seems promising, whereby the few open modes regime is still present. We extend our previous work by studying correlations in non-trivial TIs, substantiated by experimental accessible current current correlations. The main focus lies on the difference to trivial TIs and implications to the HOM effect in chaotic TI-based systems.

Experiments of chaotic cavities experiencing universal S-matrix correlations are rare. Besides the experimental realization of a chaotic cavity by microwave billiards, a possibility one might think of is the two-dimensional electronic confinement on copper surfaces. Since manipulating positions of atoms on a substrate is one key feature to build confinement structures in a controlled manner, in 1990 [35] Eigler and Schweizer paved the way for M. F. Crommie, C. P. Lutz and D. M. Eigler in 1993 [36] to utilize the circular arrangement of iron atoms on a copper surface as a confinement for electrons. The standing wave pattern in the local density of states (LDOS) was then measured by scanning tunneling microscopy (STM). Afterwards a plurality of different confinement forms, from triangulars, squares to billiard shapes [37, 38] and even fractal have been investigated. Also with the study in Ref. [39] a different direction was introduced: the 'quantum mirages', in which magnetic adatoms give rise to the spectroscopic signature of the Kondo effect [40]. Plenty of different experiments and theoretical studies for the quantum mirages [41–44] and the quantum corrals followed [44–49]. The search for fingerprints of quantum chaos in stadium shaped corrals [37, 38] was ended by Ref. [50]. It was shown that the corral is too leaky and therefore it is likely that no eigenstate is ergodic and no quantum chaos as long time phenomena can be expected.

However, it was not only the motivation of an experimental realization of chaotic cavities, but also measurements of the original quantum corral by STM and atomic force microscopy (AFM) gave further reasons for studying this setup [51]. Some of the questions which arise in this context will be studied in chapter 4. Can the elementary model with hard wall boundary conditions used in Ref. [36] be applied also in case of an additional adatom in the quantum corral? How does the position of this additional adatom influence the local density of states? Exploring bonding characteristics by AFM measurements gives rise to further questions. Are the forces between mesoscopic surface states of the artificial atom and the tip orbital mainly controlled by electrostatic Coulomb interaction? If not, does the linear combination of atomic orbitals method describe the chemical bonding between the tip orbital and the quantum corral eigenstates?

Outline of the thesis

In the following we summarize the topics investigated in the individual chapters:
Chapter 2 devotes to the computation of energy-dependent four-point S-matrix correlators for a two-dimensional electron gas (2DEG). First the link of S-matrix correlators to the HOM probability will be derived. The semiclassical analysis of S-matrix products at different energies is then transformed into a mainly combinatorial task of generating all relevant families of quadruplets contributing for a given order in inverse number of modes. To increase the complexity step by step, we first consider a two-point correlator with vanishing energy difference. The diagonal approximation, in which only identical trajectories are considered yields the first order contribution. By introducing the Sieber-Richter pairs a diagrammatic rule yields a general rule to compute the contribution of any trajectory pair family. Extending this to energy-dependent two- and four-point correlators is the final step to estimate the relevant correlators within the semiclassical approximation.
Besides this analytical approach, we will implement a numerical tight-binding model, such that universal S-matrix correlations are expected. The comparison of both methods for low number of open modes will shed light on the validity of the semiclassical approach in this regime. Finally, thanks to the collaborations with Barbara Dietz group the experimental data of microwave billiards and RMT results within the Heidelberg approach enables the extensive study of energy-dependent four-point correlators.

Based on the previous investigations, in chapter 3 we now concentrate on universal S-matrix correlations in TI-based materials, the 2D HgTe-CdTe heterostructure. For numerical adjustments we first solve the Schrödinger equation for a 2D waveguide described by Bernevig-Hughes-Zhang (BHZ) Hamiltonian. Afterwards we extend the electron coherence formalism for energy-dependent S-matrices, linking the four-point S-matrix correlators to an experimental measurable observable, the current current correlation. In the next step we concentrate on the numerical implementation of a chaotic cavity experiencing universal S-matrix correlations, whereby step wise increasing the amount of contributing orbitals. Finally the conclusion for the HOM effect in a TI-based chaotic cavity is drawn by computing the current current correlation.

In chapter 4 the quantum corral is studied in different facets and motivated by both, AFM and STM experiments done in a collaborating group in Regensburg. First we will set the base by recapturing the experimental setting and the fundamental properties of the measurement procedures. We recapture the first theoretical approach, the hard wall model which describes the appearing local density of states (LDOS) for atomic force microscopy (AFM) and scanning tunneling microscopy (STM) measurements. Intro-

ducing another iron atom inside the corral leads to standing wave patterns not predictable by the hard wall model. Therefore we want to adjust a tight-binding setup with the exact scattering phase to simulate the LDOS more accurate. In the last part we concentrate on the AFM measurements, experiencing a strong decaying force with increasing tip-sample distance. The classical Coulomb interaction and first steps into a chemical bonding description will be made.

2. Universal S-matrix correlations in non-interacting many-body systems

For the electron analog to the optical HOM effect we consider two electrons, represented by localized wavepackets, passing through a QPC and interfering with each other. As we will see, replacing the QPC by a chaotic cavity requires the precise knowledge about the universal correlations of S-matrix elements at different energies. In the first section the connection between the two-particle probability and the S-matrix correlations is provided, whereby non-interacting particles are assumed [23]. The semiclassical approach enables us to approximate the relevant S-matrix correlations by a series expansion in orders of the inverse number of open modes $1/N$. In sec. 2.2 the detailed description of this technique, based on correlations of interfering classical paths is made explicit by applying combinatorics, following Ref. [29, 52]. Three types of energy-dependent four-point correlations will then be semiclassically work out in detail in sec. 2.2.5. These analytical results will then be compared in sec. 2.3 to a tight-binding model with a cavity of billiard-shaped form. Furthermore we will compare our results with experimental microwave billiards and RMT. The investigations of this extensive analysis as presented here follows our manuscript in Ref. [53][1].

2.1. Many-body wavepacket scattering

In the spirit of Landau and Büttiker the quantum transport of non-interacting electrons in a cavity correspond to scattering between leads [54, 55]. Asymptotically, each lead is by definition translation-invariant in the longitudinal direction thus supporting wave modes of plane wave type. For a two-dimensional (2D) system and a time-independent Hamiltonian quadratic in momentum,

$$\hat{H} = \frac{\hbar^2}{2m}\hat{\boldsymbol{k}}^2 + V(x, y), \tag{2.1}$$

and assuming hard wall boundary conditions in y-direction and a width of W yields normalized transversal functions $\phi_n(y)$ of the form

$$\phi_n(y) = \sqrt{\frac{2}{W}} \sin\left(\frac{\pi n y}{W}\right), \tag{2.2}$$

[1]

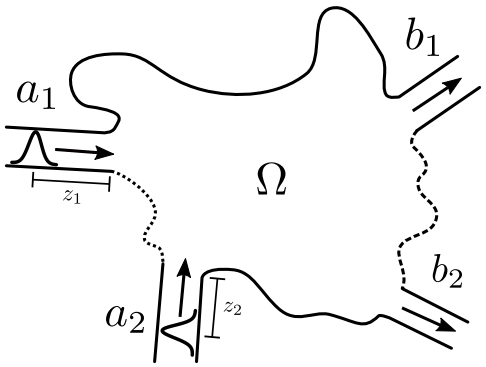

Figure 2.1: Sketch of the system illustrating the quantum state of two incoming fermions in (a_1, a_2) represented by wavepackets with a Gaussian form in longitudinal direction. The transition from effectively distinguishable particles to indistinguishable ones is tunable by the relative position $z_2 - z_1 = z$.

with n being an integer. The momentum k in x-direction is restricted by the total energy via

$$E = \frac{\hbar^2}{2m}\left(\frac{n^2\pi^2}{W^2} + k^2\right). \tag{2.3}$$

The wave modes, from now on called "channels" are therefore identified by the index n. Indeed, the plane wave solution in x-direction is only preserved if for a given energy E the channels in lead i are restricted to $n \in [1, N_i]$ with $N_i = \lfloor \frac{W}{\hbar\pi}\sqrt{2mE} \rfloor$, such that $k \in \mathcal{R}$ where $\lfloor \dots \rfloor$ is the floor function (largest integer less or equal than his argument), while otherwise the plane wave e^{ikx} will be deformed to an evanescent (non-propagating) solution. The summation over the number of open modes in each lead i determines the total number of open modes $N = \sum_{i=1} N_i$ and we assume from now on that all leads share the same number of them $N_i = N_1$. The transition amplitude from an incoming flux in channel a to the outgoing flux in b is governed by the matrix element $S_{b,a}$ of the $N \times N$ scattering matrix $S(E)$.

Now we consider an incoming wavepacket $|\zeta(E)\rangle$ at lead i with mean momentum $\bar{k} = mv/\hbar$ of the form

$$\zeta(x_i, y_i) \propto \int_{-\infty}^{\infty} dk\, e^{-ik(x_i - z)} X(k - \bar{k})\, \phi_a(y_i). \tag{2.4}$$

The particle is initially localized around $x_i = z$ such that the variance s^2 of the longitudinal normalized profile $X(x)$ fulfills $z \gg s$. This property enables us to write [23]

$$A_{b,a}(E) = \frac{1}{\sqrt{2\pi v_b}} e^{i(k_b - \bar{k})z} X(\bar{k} - k_b)\, S_{ba}(E) \tag{2.5}$$

as the probability amplitude to detect in channel b the electron with energy E which is entering the system in channel a and is represented by Eq. (2.4). Now we want to

study the two-particle scattering as a special case of n particles investigated in [23]: Two non-interacting electrons, both sharing the same mean momentum and wavepacket form X, differ in the incoming channel $\boldsymbol{a} = (a_1, a_2)$ and the mean x-position z_1, z_2 as illustrated in Fig. 2.1. When the two particles are distinguishable the many-body probability amplitude reads

$$A_{\boldsymbol{b},\boldsymbol{a}}(\boldsymbol{E}) = \prod_{i=1}^{2} \frac{1}{\sqrt{2\pi v_{b_i}}} e^{i(k_{b_i}-\bar{k})z_i}\, X\left(\bar{k} - k_{b_i}(E_i)\right)\, S_{b_i,a_i}(E_i), \tag{2.6}$$

while the energy is replaced by $\boldsymbol{E} = (E_1, E_2)$ to describe the energy in the outgoing channels $\boldsymbol{b} = (b_1, b_2)$ of both particles $i = 1, 2$. For identical fermions the indistinguishability demand an antisymmetric many-body state, given by the adapted probability amplitude

$$A'_{\boldsymbol{b},\boldsymbol{a}}(\boldsymbol{E}) = \sum_{\mathcal{P}} (-1)^{\mathcal{P}} A_{\mathcal{P}\boldsymbol{b},\boldsymbol{a}}(\mathcal{P}\boldsymbol{E}), \tag{2.7}$$

with the $2! = 2$ different permutations $\mathcal{P}$ acting on $\boldsymbol{b}$: $\mathcal{P}_1(b_1, b_2) = (b_1, b_2)$ and $\mathcal{P}_2(b_1, b_2) = (b_2, b_1)$. The probability of detecting the electrons at exits $\boldsymbol{b}$ regardless of their energies $\boldsymbol{E}$ is then given by

$$\begin{aligned} P_{\boldsymbol{b},\boldsymbol{a}} &= \frac{1}{\boldsymbol{a}!\,\boldsymbol{b}!} \int d\boldsymbol{E}\, |A'_{\boldsymbol{b},\boldsymbol{a}}(\boldsymbol{E})|^2 \\ &= \frac{1}{\boldsymbol{a}!\,\boldsymbol{b}!} \int d\boldsymbol{E} \sum_{\mathcal{P},\mathcal{P}'} (-1)^{\mathcal{P}+\mathcal{P}'} A_{\mathcal{P}\boldsymbol{b},\boldsymbol{a}}(\mathcal{P}\boldsymbol{E})\, A^*_{\mathcal{P}'\boldsymbol{b},\boldsymbol{a}}(\mathcal{P}'\boldsymbol{E}). \end{aligned} \tag{2.8}$$

The normalization of the probability to $\sum_{b_1=1}^{2}\sum_{b_2=1}^{2} P_{\boldsymbol{b},\boldsymbol{a}} = 1$ is provided by counting the multiplicity of the in- and outgoing channels $\boldsymbol{d}! = \prod_{i=1}^{n} mul(d_i)$. The summation over permutations in Eq. (2.8) yields then four terms

$$\begin{aligned} P_{\boldsymbol{b},\boldsymbol{a}} = \frac{1}{\boldsymbol{a}!\boldsymbol{b}!} \int d\boldsymbol{E} \Big[& A_{\boldsymbol{b},\boldsymbol{a}}(\boldsymbol{E})\, A^*_{\boldsymbol{b},\boldsymbol{a}}(\boldsymbol{E}) + A_{\mathcal{P}_2\boldsymbol{b},\boldsymbol{a}}(\mathcal{P}_2\boldsymbol{E})\, A^*_{\mathcal{P}_2\boldsymbol{b},\boldsymbol{a}}(\mathcal{P}_2\boldsymbol{E}) \\ & - A_{\mathcal{P}_2\boldsymbol{b},\boldsymbol{a}}(\mathcal{P}_2\boldsymbol{E})\, A^*_{\boldsymbol{b},\boldsymbol{a}}(\boldsymbol{E}) - A_{\boldsymbol{b},\boldsymbol{a}}(\boldsymbol{E})\, A^*_{\mathcal{P}_2\boldsymbol{b},\boldsymbol{a}}(\mathcal{P}_2\boldsymbol{E}) \Big]. \end{aligned} \tag{2.9}$$

Here, the first and second terms are the incoherent contributions, where two identical configurations ($\boldsymbol{b}, \boldsymbol{a}$ or $\mathcal{P}_2\boldsymbol{b}, \boldsymbol{a}$) are considered. The parameter that controls the degree of (effective) distinguishability, $z_2 - z_1 = z$ vanishes for such incoherent terms. On the contrary, the contributions in the second line are sensitive to interference between different configurations and are therefore denoted as "coherent" contributions. They do have a dependence on z. An ensemble average leads to an averaged probability $\langle P_{\boldsymbol{b},\boldsymbol{a}} \rangle$ depending on S-matrix correlators of the form

$$C^{=}(\Delta) = \langle |S_{b,a}(E_1)|^2\, |S_{d,c}(E_2)|^2 \rangle, \tag{2.10}$$

$$D^{x}(\Delta) = \langle S_{b,a}(E_1) S_{d,c}(E_2) S^*_{d,a}(E_2) S^*_{b,c}(E_1) \rangle, \tag{2.11}$$

with the energy difference $\Delta = (E_2 - E_1)/2$. In case of pure disorder only effective in the cavity, averaging is only acting on the S-matrices. This is also assumed to hold for energy averages, as long as this energy interval is small compared to the wavepacket width $v\hbar/s$. The chaotic cavity, with its strongly undulating S-matrices, exhibits universal signatures after averaging, semiclassically accessible in the considered regime. The detailed method will be described in the following sec.2.2, here we will stick to the results of the first order in $1/N$ for channels distinct from each other,

$$\begin{aligned} C^{=}(\Delta) &= \frac{1}{N^2}, \\ D^{x}(\Delta) &= -\frac{1}{N^3(1+\frac{2\Delta\tau_D}{\hbar})}, \end{aligned} \tag{2.12}$$

where τ_D is the dwell time at the mean energy $\bar{E} = (E_2 + E_1)/2$. The contribution to $C^{=}$ is in the first non-vanishing order independent on Δ such that the incoherent terms only contribute by a constant term proportional to N^{-2}. The relevant parameter to exhibit the transition from distinguishable to indistinguishable fermions, $z = z_2 - z_1$ is only present in coherent terms which share the same form:

$$\begin{aligned} P^{coh}_{\boldsymbol{b},\boldsymbol{a}} &= \frac{1}{\boldsymbol{a}!\boldsymbol{b}!}\int d\boldsymbol{E}\,\langle A_{\mathcal{P}_2\boldsymbol{b},\boldsymbol{a}}(\mathcal{P}_2\boldsymbol{E})\,A^{*}_{\boldsymbol{b},\boldsymbol{a}}(\boldsymbol{E})\rangle \\ &= \frac{1}{\boldsymbol{a}!\boldsymbol{b}!}\int d\boldsymbol{E}\,\langle A_{\boldsymbol{b},\boldsymbol{a}}(\boldsymbol{E})\,A^{*}_{\mathcal{P}_2\boldsymbol{b},\boldsymbol{a}}(\mathcal{P}_2\boldsymbol{E})\rangle \\ &= \frac{1}{\boldsymbol{a}!\boldsymbol{b}!}\int d\boldsymbol{E}\,\frac{|X\left(\bar{k}-k_{a_1}(E_1)\right)|^2|X\left(\bar{k}-k_{a_2}(E_2)\right)|^2}{4\pi v_{a_1}v_{a_2}N^3}\,e^{i(k_{a_1}-k_{a_2})z}\left(1+\frac{2\Delta\tau_D}{\hbar}\right)^{-1}. \end{aligned} \tag{2.13}$$

For a Gaussian incoming wavepacket form,

$$\tilde{X}(x) = \frac{1}{2\pi}\int dk\,X(k)\,e^{ikx} = \frac{1}{\sigma\sqrt{2\pi}}e^{-\frac{x^2}{2s}}, \tag{2.14}$$

with a width of the incoming wavepacket given by $s = v\tau_s$. As shown in Ref. [23], when tuning the ratio τ_D/τ_s from 0.1 to 5, the many-body transition probability changes from a convolution, given by $\int \tilde{X}(x)\tilde{X}(x-z)\,dx$ to a form with exponential, and therefore universal, tails. For a chaotic system with a larger dwell time $\tau_D \gg \tau_s$, the HOM probability is therefore independent on the form of the incoming wavepackets $X(x)$ [23].

2.2. Semiclassical approach of energy-dependent correlators in chaotic systems

As we have shown, the two-body scattering probability relevant for the HOM effect in a system, displaying chaos in the classical dynamics of single particles, is controlled by energy-dependent four-point S-matrix correlators D^x and $C^=$. In this section we will provide a method to approximate these correlators semiclassicaly, following well-stablished established methods [29, 52].

To get the four-point S-matrix correlators of Eq. (2.10) and (2.11) we will now operate in the semiclassical limit: The characteristic length of the system L is large compared to the Fermi wavelength λ. For the lead width W small compared to the system length L, the dwell time $\tau_D \propto \frac{L}{W}$ exceeds the Ehrenfest time $\tau_E \approx \lambda_{Ly}^{-1} \log(L/\lambda_F)$, the time required to spread a wave packet of initial size λ to sizes of orders of L under the classical chaotic flow with Lyaponov exponent λ_{Ly}. In this regime the S-matrix elements can be approximated by [24–26]

$$S_{b,a} \approx \frac{1}{\sqrt{T_H}} \sum_{\gamma: a \to b} A_\alpha e^{i\mathcal{S}_\gamma/\hbar}, \tag{2.15}$$

with the Heisenberg time $T_H = N\tau_D$. Both, the stability amplitude A_γ and the classical action $\mathcal{S}_\gamma = \int_\gamma \boldsymbol{p} \cdot d\boldsymbol{q}$, depend on the trajectory γ solving the classical Lagrange equation, where specular reflections are assumed at the hard-wall boundaries of the cavity. Each trajectory γ is starting in the incoming lead and mode a and ending in the outgoing lead and mode b as sketched in Fig. 2.2. The key point in deriving Eq. (2.15) is the application of the stationary phase approximation assuming the typical actions of the Feynman paths to be much greater than $\hbar$ [26], the so-called semiclassical regime.

In principle the S-matrix strongly depends on the detailed shape of the system. However, our purpose is to investigate the setup in case of a fully chaotic cavity whereby chaos is caused by the shape of the boundary. The appearing universal features enable us to study this system without the detailed knowledge of the system (the specific numerical values of the entries of the scattering matrix). It is worth to mention that we understand chaos in quantum systems as the appearing signatures in quantum system which exhibits classical chaotic motion in the classical limit [17]. For the definition of classical chaos we refer to a few of the numerous accessible literature [56–58]. For later reasons it is sufficient to know the implication of chaotic systems regarding ergodicity: A typical trajectory will approach arbitrarily close any point in phase space when given enough time.

Our focus in the following is to use the statistical properties of chaos to approximate two-point and four-point S-matrix correlators using the semiclassical S-matrix in

Eq. (2.15). The correlators, depending on two energies $E_\pm = \bar{E} \pm \Delta$ have the form

$$C_2(\Delta) = \langle S_{b,a}(E_+) S^*_{b,a}(E_-) \rangle, \tag{2.16a}$$
$$D^x(\Delta) = \langle S_{b,a}(E_+) S_{d,c}(E_-) S^*_{b,c}(E_+) S^*_{d,a}(E_-) \rangle, \tag{2.16b}$$
$$C^=(\Delta) = \langle |S_{b,a}(E_+)|^2 |S_{d,c}(E_-)|^2 \rangle \tag{2.16c}$$
$$B^=(\Delta) = \langle S_{b,a}(E_+) S_{d,c}(E_+) S^*_{b,a}(E_-) S^*_{d,c}(E_-) \rangle \tag{2.16d}$$

with $\{a, b, c, d\}$ being distinct open channels and an energy average over $\bar{E}$ is represented by $\langle \dots \rangle$. We will see that in chaotic systems these objects will acquire a universal form which is independent of the exact system shape. Only conservation or absence of time-reversal symmetry and spin-rotation symmetry, affect the correlator form. Here we will concentrate on two cases of half-integer spin particles, the orthogonal and the unitary one, where the time-reversal symmetry and the spin rotational symmetry is preserved or absent. Following Dyson's Threefold way [20] the S-matrices obey the statistics of the Circular Orthogonal Ensemble (COE) and the Circular Unitary Ensemble (CUE) in RMT.

To understand the semiclassical method we use to compute these correlators, we will start with the two-point correlator C_2 with $\Delta = 0$. Using Eq. (2.15) we get,

$$C_2(0) = \frac{1}{T_H} \Big\langle \sum_{\substack{\gamma: a \to b \\ \gamma': a \to b}} A_\gamma A^*_{\gamma'} \, e^{\frac{i}{\hbar}(\mathcal{S}_\gamma - \mathcal{S}_{\gamma'})} \Big\rangle, \tag{2.16}$$

while our restriction $a \neq b$ enforces the two trajectories γ, γ' to have to distinct endings, the case $a = b$ contains extra, so-called weak localization, effects that will be addressed later on. We will refer from now on to trajectory pairs in contrast to periodic orbit pairs which are closed. For most of these pairs the highly oscillating phase $(\mathcal{S}_\gamma - \mathcal{S}_{\gamma'})/\hbar$ yields vanishing contributions to C_2 when averaged. Only if the action difference is of the order of $\hbar$ this summand survive the averaging and contribute to the two-point correlator.

2.2.1. Diagonal approximation and Sieber-Richter orbit pairs

The diagonal approximation includes only trajectory pairs, such that the action difference $\Delta\mathcal{S} = \mathcal{S}_\gamma - \mathcal{S}_{\gamma'}$ vanishes. For systems without exact discrete symmetries this implies that both trajectories are equal, $\gamma = \gamma'$ [59], as illustrated in Fig. 2.2(a) by one exemplary pair. The contribution from such pairs to C_2 reads

$$C_2(0) \approx \frac{1}{T_H} \Big\langle \sum_{\gamma: a \to b} |A_\gamma|^2 \Big\rangle \tag{2.17}$$

and following [27], it can be evaluated to get

$$C_2(0) \approx \frac{1}{T_H} \frac{T_H}{N} = \frac{1}{N}. \tag{2.18}$$

The next order in the orthogonal case is the key point for generalizing the C_2 evaluation. The trajectory pairs contributing to C_2 for this order should share the same path for almost the total length, but containing a region where the two stretches differ, such that $\Delta\mathcal{S}$ is of the order of $\hbar$. This situation is called "2-encounter" and includes two stretches, displayed as a gray box in Fig. 2.2(b). Therein the adjacency of both trajectories enables to approximate their motion linearly [27] around the point where the γ (γ') trajectory exhibits an avoided crossing (self-crossing). The encounter separate regimes where γ and γ' coincide, named "links". In Fig. 2.2(b) three links and one 2-encounter appear. In the second link the velocities of γ and γ' are opposite, which can only occur in systems with time-reversal symmetry. For interested readers we refer to Ref. [17, 27, 29, 52] for more details, here we will concentrate on the major conclusion, the so called "diagrammatic rule", when evaluating the effect of these trajectory pairs on C_2: each link contribute by a factor of $1/N$ and each encounter by a factor of $-N$. For each link or encounter the Heisenberg time will cancel out, in analogy to Eq. (2.18). The trajectory pair with one $2-$encounter and three links, as depicted in Fig. 2.2(b) contribute therefore by $-\frac{N}{N^3} = -\frac{1}{N^2}$. In combination with Fig. 2.2(a) it results in $C_2(0)$ approximated by

$$C_2(0) \approx \frac{1}{N} - \frac{1}{N^2} + \mathcal{O}\left(N^{-3}\right). \tag{2.19}$$

in the orthogonal case and

$$C_2(0) \approx \frac{1}{N} + \mathcal{O}\left(N^{-3}\right). \tag{2.20}$$

in the unitary case.

2.2.2. Diagrammatic rule

To generalize this rule for higher orders in $1/N$ a detailed description of trajectory types is necessary. In the previous section, we dealt with a 2-encounter, which will now be generalized to a $l-$encounter where l stretches are involved. The corresponding structures with increased number of $l-$encounters and links substantially increases the complexity. It is known that also $l-$encounters contribute by a factor of $-N$ [29, 52]. Hence the ratio of links and $l-$encounters provides the contributing order in $1/N$ for each trajectory pair. To characterize all possible trajectory pairs we define some useful properties: The vector $\boldsymbol{v} = (v_2, v_3, \dots)$ specifies that γ and γ' differ in v_l $l-$encounters. The total amount of encounters is given by $V(\boldsymbol{v}) = \sum_{l\geq 2} v_l$, at which $L(\boldsymbol{v}) = \sum_{l\geq 2} l v_l$ encounter stretches appear. The number of links is limited to $L(\boldsymbol{v}) + 1$. In case of Fig. 2.2(b) it follows $\boldsymbol{v} = (1, 0, 0, \dots) = (1)$, $V = 1$, $L = 2$ and by applying the diagrammatic rule, the contribution to $C_2(0)$ is given by

$$(-N)^V N^{-L-1} = -\frac{1}{N^2}. \tag{2.21}$$

By knowing the number of links and encounters in each trajectory pair, we can therefore compute the contributing factor. However one major difficulty remains: What are the

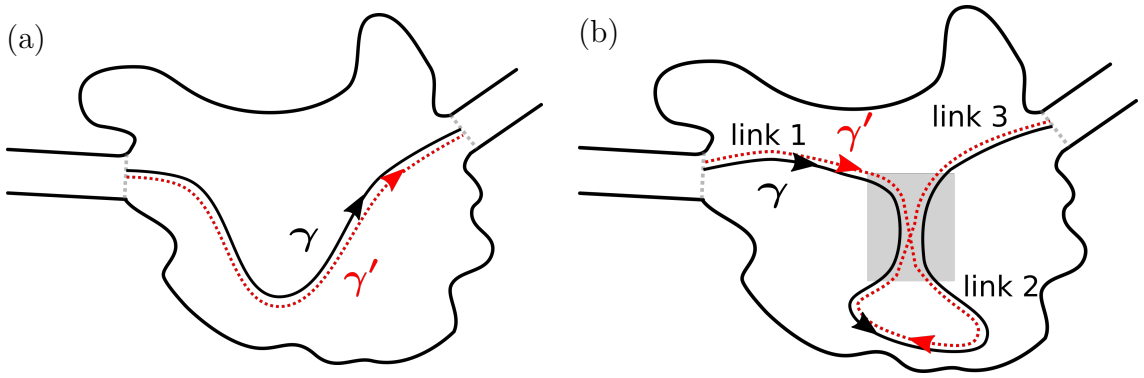

Figure 2.2: The trajectory pairs contributing in first order in $1/N$ to C_2 are illustrated in configuration space. In (a) we illustrate trajectory pairs of the diagonal approximation, where the two trajectories are identical across the whole path. In (b) trajectory pairs of the next order in $\Delta\mathcal{S}/\hbar$ are sketched. In each link the trajectories are again identically, however the links are separated by one 2−encounter, displayed in the grayish area. The opposite traverse directions in the second link require a system with time-reversal invariance.

number of possible trajectory pairs $\mathcal{N}(\boldsymbol{v})$ for a given vector? In the next section we will address this task of determining $\mathcal{N}(\boldsymbol{v})$ to estimate $C_2(0)$ by

$$C_2(0) = \frac{1}{N} + \sum_{\boldsymbol{v}} (-1)^{V(\boldsymbol{v})} \frac{1}{N^{L(\boldsymbol{v})+1-V(\boldsymbol{v})}} \mathcal{N}(\boldsymbol{v}). \tag{2.22}$$

2.2.3. Combinatorics

There exist a direct one-to-one correspondence between the periodic orbit pairs relevant in closed systems and the open trajectory pairs with ingoing channel a distinct from outgoing channel b [29,52]. Therefore we can use the recursive relation from Ref. [29] to compute $\mathcal{N}(\boldsymbol{v})$. However, we will use a method provided in Ref. [52] which is slightly more complex and time-consuming, but will straight the line for the energy-dependent four-point correlators where it is the only known method to compute the correlators in a semiclassical manner. In the following we will describe topologically different periodic orbit pairs by permutations and yield $\mathcal{N}(\boldsymbol{v})$ for these closed orbits. To begin with, we will picture the method of achieving $\mathcal{N}(\boldsymbol{v})$ for periodic orbits in the unitary case and afterwards for the more complicated orthogonal case. In sec. 2.2.3 we illustrate that the mapping from periodic orbit pairs to trajectory pairs results in an algorithm to construct $\mathcal{N}(\boldsymbol{v})$ for trajectory pairs. For four-point correlators the relevant quadruplets with four distinct endings will be generated in a more complex manner by periodic orbit pairs fulfilling specific criteria.

Unitary case

Each periodic orbit pair is classified by permutation operations. This mapping is trivial for the permutation P_{link} which describes the connections between stretches exiting a $l-$encounter and stretches entering the next $l-$encounter. In our chosen notation, it is given by

$$P_{\text{link}} = \begin{pmatrix} 1 & 2 & \dots & L-1 & L \\ 2 & 3 & \dots & L & 1 \end{pmatrix}, \tag{2.23}$$

where the upper (lower) row corresponds to individual stretches exiting (entering) an $l-$encounter. Both trajectories γ, γ' of a periodic orbit pair share the same path outside of a $l-$encounter and thus are described by the same P_{link}. The permutations of stretches in the encounters are on the other hand depending on the trajectories γ, γ'. We choose the notation such that the stretches are labeled in ascending order by $1, 2, \dots, L$ for the γ trajectory and thus results in a P^{γ}_{enc} given by

$$P^{\gamma}_{\text{enc}} = \begin{pmatrix} 1 & 2 & \dots & L-1 & L \\ 1 & 2 & \dots & L-1 & L \end{pmatrix}. \tag{2.24}$$

The $i-$th stretch entering an encounter at entrance i is leaving the encounter at exit port i, while the stretches of the trajectory γ' are differently connected in the encounters, in general given by

$$P^{\gamma'}_{\text{enc}} = \begin{pmatrix} 1 & 2 & \dots & L-1 & L \\ P_{\text{enc}}(1) & P_{\text{enc}}(2) & \dots & P_{\text{enc}}(L-1) & P_{\text{enc}}(L) \end{pmatrix}, \tag{2.25}$$

with $P^{\gamma'}_{\text{enc}}(i) \neq i$. To simplify the notation, we use from now on $P^{\gamma'}_{\text{enc}} = P_{\text{enc}}$. For a periodic orbit pair with only one $l-$encounter, the P_{enc} is a single cycle of length l. This means that right after l steps we end up again at the beginning. A permutation for two $2-$encounters has two cycles of length 2, e.g.

$$P_{\text{enc}} = \begin{pmatrix} 1 & 2 & 3 & 4 \\ 3 & 4 & 1 & 2 \end{pmatrix} \tag{2.26}$$

with the cycle $1 \to 3 \to 1$ and $2 \to 4 \to 2$. The entire path of γ' is the given by the composition of the two permutations,

$$P = P_{\text{link}} \circ P_{\text{enc}}. \tag{2.27}$$

In Fig. 2.3(a) the corresponding periodic orbit pair is displayed and we once explicitly compute the composition,

$$\begin{aligned} P &= P_{\text{link}} \circ P_{\text{enc}} \\ &= \begin{pmatrix} 1 & 2 & \dots & L-1 & L \\ 2 & 3 & \dots & L & 1 \end{pmatrix} \circ \begin{pmatrix} 1 & 2 & 3 & 4 \\ 3 & 4 & 1 & 2 \end{pmatrix}. \end{aligned} \tag{2.28}$$

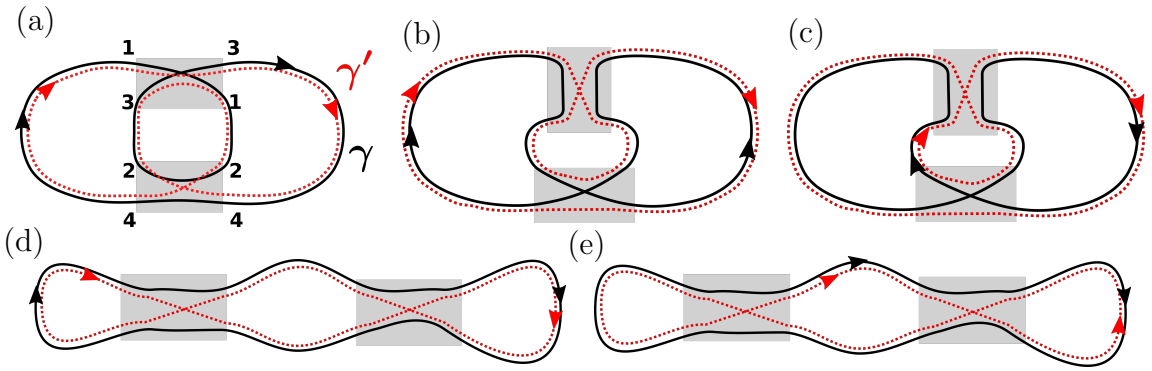

Figure 2.3: All periodic orbit pairs with two 2−encounters are sketched. In the unitary case the only periodic orbit pair contributing is displayed in (a) and described by the encounter permutation in Eq. (2.26). In systems with time-reversal invariance additionally the pairs in (b)-(e) are possible configurations at which opposite traverse directions in links appear.

The γ' trajectory is described by the $L(\boldsymbol{v})$ steps (encounter and link combined)

$$1 \overset{\text{enc}}{\to} 3 \overset{\text{link}}{\to} 4 \overset{\text{enc}}{\to} 2 \overset{\text{link}}{\to} 3 \overset{\text{enc}}{\to} 1 \overset{\text{link}}{\to} 2 \overset{\text{enc}}{\to} 4 \overset{\text{link}}{\to} 1, \tag{2.29}$$

with $L(\boldsymbol{v}=(2))=4$. The criteria for the permutations P_{enc} and P_{link} to describe physical relevant periodic orbit pairs are

- P_{enc} has v_l $l-$cycles,
- $P = P_{\text{link}} \circ P_{\text{enc}}$ has only one cycle with length $L(\boldsymbol{v})$.

Successive passing through all $L!$ possible P_{enc} and counting the permutations P fulfilling these criteria leads to all possible periodic orbit pairs.

Orthogonal case

In systems with time-reversal invariance the periodic orbits γ, γ' are able to traverse a link in opposite directions. This fact causes an increased number of possible periodic orbit pairs for a given vector $\boldsymbol{v}$ compared to the unitary case. As an example, in Fig. 2.3(b)-(e) are the additional periodic orbit pairs for $\boldsymbol{v}=(2)$ illustrated. To incorporate the freedom in directions we introduce

$$\boldsymbol{\sigma} = (\sigma_1, \sigma_2, \ldots, \sigma_L), \tag{2.30}$$

in which each $\sigma_i = \pm 1$ represents two possible traverse directions at stretch i. Only the relative direction between γ and γ' are physically relevant, such that the first $V(\boldsymbol{v})$ stretches will be chosen to $+1$. The remaining $\boldsymbol{\sigma}$ elements are representing $2^{L(\boldsymbol{v})-V(\boldsymbol{v})}$ possibilities to consider in addition to the unitary case. In accordance to the unitary case the restriction on P_{enc} is still that of having v_l $l-$cycles. However to detect all

combinations of P_{enc} and $\boldsymbol{\sigma}$ which fulfill the criteria of P having one cycle of length L is more time-consuming. In comparison to the unitary case with $L!$ possibilities of the permutation P_{enc}, now we deal with $2^{L(\boldsymbol{v})-V(\boldsymbol{v})}L!$ possibilities for $(P_{\text{enc}}, \boldsymbol{\sigma})$ combinations for each $\boldsymbol{v}$. The total permutation P is not anymore given by a pure composition $P_{\text{link}} \circ P_{\text{enc}}$ as all steps of γ' beginning at the first encounter, passing different links and further encounters and finally ending at the start, need to be considered gradually. Each step, following a link or passing an encounter, is thereby influenced by the previous step, σ_i and P_{enc}. The number of relevant tuples $(P_{\text{enc}}, \boldsymbol{\sigma})$ for a given vector $\boldsymbol{v}$ is then reproducing the number of allowed periodic orbit pairs.

Mapping to trajectory pairs and quadruplets

So far we have described an algorithm to find the number of periodic orbits for each given vector $\boldsymbol{v}$. Our correlators of interest however depend on trajectory pairs (two-point correlators) and quadruplets (four-point correlators). The former are directly mapped by periodic orbits: As shown in Ref. [52] there exist a one-to-one correspondence, cutting one link of each periodic orbit generates all relevant trajectory pairs. The only requirement is that both trajectories share the same traveling direction in this cut out link. In case of four-point correlators the relevant quadruplets are generated by periodic orbits with at least one 2−encounter. The directions inside the 2−encounter are chosen such that when cutting out this encounter, illustrated by the gray area in Fig. 2.4(a) the remaining ones will always have crossing trajectories and therefore at least one additional encounter. By introducing further encounters in the remaining quadruplet, all possible quadruplets of the so called "x-families" can be generated. These quadruplets are the relevant ones for the $D^x(0) = \langle S_{b,a}(\bar{E})S_{d,c}(\bar{E})S^*_{b,c}(\bar{E})S^*_{d,a}(\bar{E})\rangle$ correlator, where the crossing is forced by the interchange of $a \leftrightarrow c$ and $b \leftrightarrow d$. For $C^=(0) = \langle |S_{b,a}(\bar{E})|^2 |S_{d,c}(\bar{E})|^2\rangle$ and $B^=(0)$ the quadruplets of relevance are called "d-families". These families are equivalently generated by the periodic orbit depicted in Fig. 2.4(b), whereby the direction of motion of one trajectory is reversed such that all four share the same direction. The method is then used to compute four-point correlators by removing the contribution of the cut out 2−encounter.

2.2.4. Diagrammatic rule for energy depended correlators

So far all correlators were considered at the same energy E. The next step in rising complexity is introduced when considering the complete correlators of interest with $E_\pm = \bar{E} \pm \Delta$ from Eqs. (2.16a)-(2.16d). In the same manner as the previous diagrammatic rule of Eq. (2.22) was developed, in Ref. [52] a diagrammatic rule for energy-dependent correlators was established[2]. Here we will sketch it for the two-point correlator

$$C_2(\Delta) = \frac{1}{T_H}\Big\langle \sum_{\substack{\gamma:a\to b\\ \gamma':a\to b}} A_\gamma A^*_{\gamma'}\, e^{\frac{i}{\hbar}\left(\mathcal{S}_\gamma(E_+)-\mathcal{S}_{\gamma'}(E_-)\right)}\Big\rangle. \tag{2.31}$$

[2]In Ref. [52] this is also adapted to include magnetic fields.

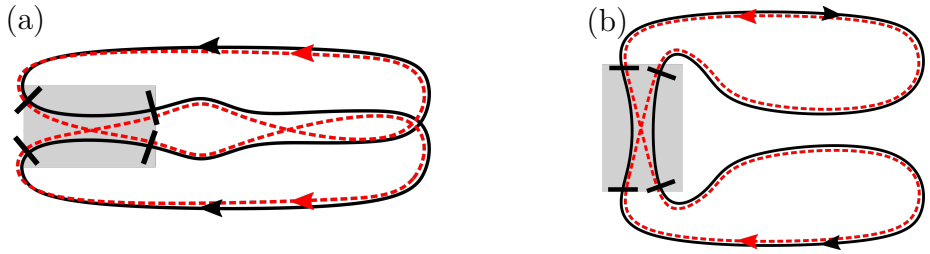

Figure 2.4: The method to calculate the number of periodic orbits can be applied also for four-point S-matrix correlators, where instead of pairs quadruplets are the relevant objects. To generate the required quadruplets for the D^x correlator, only periodic orbits with at least one 2−encounter are relevant. Cutting out the 2−encounter (gray background) of the periodic orbit in (a) produces for example the first order contribution to D^x. To gain instead the quadruplets for $C^=$ one cut out the 2−encounter of the periodic orbits of the shape illustrated in (b).

Both energies E_+, E_- can be expressed in terms of the dimensionless quantity η, which is rescaled by the dwell time $\tau_D = T_H/N$:

$$E_\pm = \bar{E} \pm \Delta = \bar{E} \pm \frac{\eta\hbar N}{2T_H} = \bar{E} \pm \frac{\eta\hbar}{2\tau_D}, \tag{2.32}$$

while we approximate the action difference by

$$\mathcal{S}_\gamma(E_+) - \mathcal{S}_{\gamma'}(E_-) \approx \mathcal{S}_\gamma(\bar{E}) - \mathcal{S}_{\gamma'}(\bar{E}) + \frac{\eta\hbar}{2\tau_D}\left(T_\gamma + T_{\gamma'}\right) \tag{2.33}$$

introducing the traveling time $T_\gamma = \frac{\partial \mathcal{S}_\gamma}{\partial E}$ of an individual trajectory γ. The summation of traveling times are expressible in terms of the time required for passing a link, t_i or an encounter t_{enc}:

$$T_\gamma + T_{\gamma'} = \sum_{i=1}^{L+1} \chi_i\, t_i + \sum_{\alpha=1}^{V} \kappa_\alpha\, t_{\text{enc}}. \tag{2.34}$$

Explicit analysis in Ref. [52] gives an adapted diagrammatic rule, where each link yields a factor of $N^{-1}\left(1 - \frac{i\chi_i\eta}{2}\right)^{-1}$ and each encounter a factor of $-N(1 - \frac{i\kappa_\alpha\eta}{2})$. The trajectory pair (γ, γ') will always share each link and both trajectories will also pass each $l-$encounter l times, such that $\chi_i = 2$ and $\kappa_\alpha = 2l$. Therefore, this results in an adjustment of the previous rule in Eq. (2.22) to

$$\frac{1}{N^{L+1}(1-i\eta)^{L+1}} \prod_{l=2}^{V} [-N(1-il\eta)]^{v_l}\, \mathcal{N}(\boldsymbol{v}), \tag{2.35}$$

contributing to $C_2(\Delta)$ for each given vector $\boldsymbol{v}$. Using this method the first orders of $C_2(\Delta)$ in the orthogonal case are given by [60, 61]

$$C_2(\Delta) = \frac{1}{N(1-i\eta)} - \frac{1-2i\eta}{N^2(1-i\eta)^3} + \frac{5(1-2i\eta)^2}{N^3(1-i\eta)^5} - \frac{4(1-i3\eta)}{N^3(1-i\eta)^4} + \mathcal{O}(N^{-4}), \tag{2.36}$$

where the vector $\boldsymbol{v}$ is (0), (1), (2) or (0, 1). In case of the unitary case the vectors contributing to the maximal order of N^{-3} are (0), (2), (0, 1). Applying Eq. (2.35) produces [60]

$$C_2(\Delta) = \frac{1}{N(1-i\eta)} + \frac{(1-2i\eta)^2}{N^3(1-i\eta)^5} - \frac{(1-3i\eta)}{N^3(1-i\eta)^4} + \mathcal{O}(N^{-4}). \tag{2.37}$$

For $\boldsymbol{v} = (2)$ the different prefactors for the term $\frac{(1-2i\eta)^2}{N^3(1-i\eta)^5}$ in Eqs. (2.36)-(2.37) are 5 and 1. This is exactly representing the number of possible trajectory pairs sketched in Fig. 2.3.
For quadruplets not every trajectory will pass each link and/or encounter, so that the parameters χ_i and κ_α are not only dependent on the vector $\boldsymbol{v}$ but also on P_{enc} and $\boldsymbol{\sigma}$. The knowledge of the exact path of each of the four trajectories, determined by P_{enc} and in the orthogonal case additionally by $\boldsymbol{\sigma}$, is required to identify these parameters. The benefit of our algorithm is based on this property and therefore is appropriate for energy-dependent four-point correlators.

2.2.5. Applying the method for energy-dependent four-point correlators

The above discussed method is now applied to carry on a semiclassical approach for the correlators

$$D^x(\Delta) = \langle S_{b,a}(E_+)S_{d,c}(E_-)S^*_{b,c}(E_+)S^*_{d,a}(E_-)\rangle, \tag{2.38}$$
$$C^=(\Delta) = \langle |S_{b,a}(E_+)|^2 |S_{d,c}(E_-)|^2\rangle, \tag{2.39}$$

with $E_\pm = \bar{E} \pm \Delta$. As described in sec. 2.1 these four-point correlators are relevant for the two-particle scattering. For reasons of completeness and comparison with numerical and experimental results later we will also investigate the semiclassical approximation of

$$B^=(\Delta) = \langle S_{b,a}(E_+)S_{d,c}(E_-)S^*_{b,a}(E_-)S^*_{d,c}(E_+)\rangle. \tag{2.40}$$

Key for later applications to topological systems, our intention is also to study these correlators for low number of open modes N such that we require a sufficient number of terms. At the beginning we are generating all possible vectors $\boldsymbol{v}$ with at least one 2-encounter, because these are relevant for four-point correlators. The achieved vectors are listed in Table 2.1, separated in contributing orders of $N^{-\alpha}$ with $\alpha = L(\boldsymbol{v}) - V(\boldsymbol{v}) + 1$. Thereby we use a short notation of vector $\boldsymbol{v}$: $(a)^b$ describes b a-encounters, such that $\boldsymbol{v} = (1, 0, 5)$ for example is then rewritten as $(2)^1(4)^5$. In the unitary case the permutations $P = P_{\text{link}} \circ P_{\text{enc}}$ fulfilling the two criteria of P_{enc} having v_l l-cycles and P having one $L(\boldsymbol{v})$ cycle are then describing relevant quadruplets for either $C^=$ and $B^=$ (d-families) or D^x (x-families). When we consider systems with time-reversal symmetry the possible quadruplets are described by the tuples $(P_{\text{enc}}, \boldsymbol{\sigma})$. Compared to the unitary case the amount of allowed quadruplets increase drastically, where the possibility of traversing

the same link in different directions (governed by $\boldsymbol{\sigma}$) allows here for extra quadruplets to exist. To illustrate the computational effort to achieve Table 2.1, focus on the row $\alpha = 6$ in the unitary case. By adding all possibilities of P_{enc} (given by $L(\boldsymbol{v})!$) for the five different vectors, we achieve around $4 \cdot 10^6$. However, only a fraction of it, 881 encounter permutations are of relevance for four-point correlators.
To compute now the contribution of each quadruplet we analyze the four trajectories of each correlator regarding their traveling times. For the C_2 correlator we extracted χ_i and κ_α by Eq. (2.34), whereby i and α are counting the links and encounters. In the same manner we are deriving the difference of traveling times ΔT of four trajectories $\gamma_1, \ldots, \gamma_4$:

$$\begin{aligned} \Delta T &= T_{\gamma_1} - T_{\gamma_2} - T_{\gamma_3} + T_{\gamma_4} \qquad \text{for } D^x \text{ and } C^=, \\ \Delta T &= T_{\gamma_1} + T_{\gamma_2} + T_{\gamma_3} + T_{\gamma_4} \qquad \text{for } B^=. \end{aligned} \tag{2.41}$$

The labeling of D^x and $B^=$ by the trajectories γ_i is given by their sequence in Eq. (2.38) and (2.40). In case of $C^=$ we explicitly write the four S-matrices in the form

$$C^=(\Delta) = \langle S_{b,a}(E_+) S_{d,c}(E_-) S^*_{b,a}(E_+) S^*_{d,c}(E_-) \rangle, \tag{2.42}$$

such that the notation is also governed by the sequence. By extracting χ_i and κ_α, the contribution of each link (encounter) is governed by $N^{-1}(1 - \frac{i\chi_i\eta}{2})^{-1}$ respectively $-N(1 - \frac{i\kappa_\alpha\eta}{2})$.

Following our method, we achieve finally a semiclassical approximation for the energy-dependent S-matrix correlators.

Orthogonal case

In the case of systems with time-reversal symmetry the resulting approximations for the HOM relevant correlators are given by

$$\begin{aligned} D^x(\Delta) = &-\frac{1}{N^3(1+\eta^2)} + \frac{2\eta^4 + 10\eta^2 + 4}{N^4(1+\eta^2)^3} - \frac{8\eta^8 + 30\eta^6 + 145\eta^4 + 56\eta^2 + 13}{N^5(1+\eta^2)^5} \\ &+ \frac{28\eta^{12} + 190\eta^{10} + 196\eta^8 + 2832\eta^6 + 392\eta^4 + 258\eta^2 + 40}{N^6(1+\eta^2)^7} \\ &- \frac{96\eta^{16} + 834\eta^{14} + 3694\eta^{12} - 10940\eta^{10}}{N^7(1+\eta^2)^9} \\ &- \frac{85701\eta^8 - 25490\eta^6 + 6108\eta^4 + 1012\eta^2 + 121}{N^7(1+\eta^2)^9} \\ &+ \mathcal{O}(N^{-8}) \end{aligned} \tag{2.43}$$

α	$\boldsymbol{v}$	unitary		orthogonal	
		d-families	x-families	d-families	x-families
2	$(2)^1$	1	0	1	0
3	$(2)^2$	0	1	2	1
4	$(2)^3; (2)(3)$	9	0	29	12
5	$(2)^4; (2)^2(3); (2)(4)$	0	57	470	277
6	$(2)^5; (2)^3(3); (2)^2(4);$ $(2)(3)^2; (2)(5)$	881	0	11.977	7.352
7	$(2)^6; (2)^4(3); (2)^3(4); (2)^2(5);$ $(2)^2(3)^2; (2)(6); (2)(3)(4)$	0	10.769	367.594	249.961

Table 2.1: For both symmetry classes and family types the number of contributing quadruplets to the four-point correlators are shown. For each order in $N^{-\alpha}$ we list the contributing vectors defined by fulfilling $L(\boldsymbol{v}) - V(\boldsymbol{v}) + 1 = \alpha$. For the unitary case without time-reversal symmetry, the number of permutations P describing a quadruplet is shown for D^x (x-families) and $C^=$, $B^=$ (d-families). In accordance, we itemize the number of tuples $(P_{\text{enc}}, \boldsymbol{\sigma})$ corresponding to individual quadruplets for the orthogonal case, too.

and

$$\begin{aligned} C^{=}(\Delta) = \frac{1}{N^2} - \frac{2}{N^3} + \frac{3\eta^2+5}{N^4\left(1+\eta^2\right)} - \frac{2\left(2\eta^6+9\eta^4+18\eta^2+7\right)}{N^5\left(1+\eta^2\right)^3} \\ + \frac{5\eta^{10}+47\eta^8+146\eta^6+404\eta^4+181\eta^2+41}{N^6\left(1+\eta^2\right)^5} \\ - \frac{2\left(3\eta^{14}+60\eta^{12}+323\eta^{10}+585\eta^8\right)}{N^7\left(1+\eta^2\right)^7} \\ - \frac{2\left(3417\eta^6+806\eta^4+393\eta^2+61\right)}{N^7\left(1+\eta^2\right)^7} \\ + \mathcal{O}(N^{-8}), \end{aligned} \tag{2.44}$$

with $\eta = 2\Delta\tau_D/\hbar$. As expected, both correlators are real. This can be directly seen for $C^{=}$ in Eq. (2.39). For D^x the complex conjugation and interchange of channels yields

$$D^{x^*}(\Delta) = \langle S_{b,c}(E_1)S_{d,a}(E_2)S^*_{b,a}(E_1)S^*_{d,c}(E_2)\rangle \overset{\substack{a\leftrightarrow c,\\ b\leftrightarrow d}}{=} D^x(\Delta), \tag{2.45}$$

such that this correlator has a vanishing imaginary part, too. Our results in Eqs. (2.43)-(2.44) share this characteristic for each order in $1/N$. The first order contribution to D^x stems from only one quadruplet illustrated in Fig. 2.5(a). The upper left link is only traversed by γ_1 and γ_4. With respect to the signs in Eq. (2.41) it follows $\chi_1 = 1 - 0 - 0 + 1 = 2$ and thus $N^{-1}(1-i\eta)^{-1}$. For the lower left link, only passed by γ_2 and γ_3 we get $\chi_2 = 0 - 1 - 1 + 0 = -2$ and therefore the contributing factor of $N^{-1}(1+i\eta)^{-1}$. In the encounter all trajectories take part, such that it results in a energy-independent factor of $-N$. In the two links after the encounter, each χ_i vanishes because of the trajectory pairs sharing the same energy. Thus each link contribute by a energy-independent factor of $1/N$. The overall contribution is then given by $-NN^{-4}(1-i\eta)^{-1}(1+i\eta)^{-1} = -N^{-3}(1+\eta^2)$. In case of $C^{=}$, Fig. 2.5(b) sketches the only quadruplet of first order contribution. This quadruplet has no encounter and only two links, in which two trajectories with the same energy appear. By that the total impact is again a real number and given by N^{-2}. It is important to mention, that in principle one quadruplet can give a contribution which has a non-vanishing imaginary part. Summing the contributions of all quadruplets for a given order in $1/N$ however yields for D^x and $C^{=}$ always a pure real number.

For $C^{=}$, at each order there exist quadruplets with two disconnected pairs as depicted in Fig. 2.5(b). When introducing a 2-encounter in one of these pairs, the energies of each pair will still be the same. In this scenario, there exist one 2-encounter and four links, such that the contribution is given by $-NN^{-4} = -N^{-3}$. By moving the 2-encounter to the other trajectory pair, the same result appears, such that we have a total contribution of $-2N^{-3}$ for this disconnected pairs. The summation over all separated pairs for all orders results in [62]

$$\frac{1}{(N+1)^2} = \frac{1}{N^2} - \frac{2}{N^3} + \frac{3}{N^4} + \dots. \tag{2.46}$$

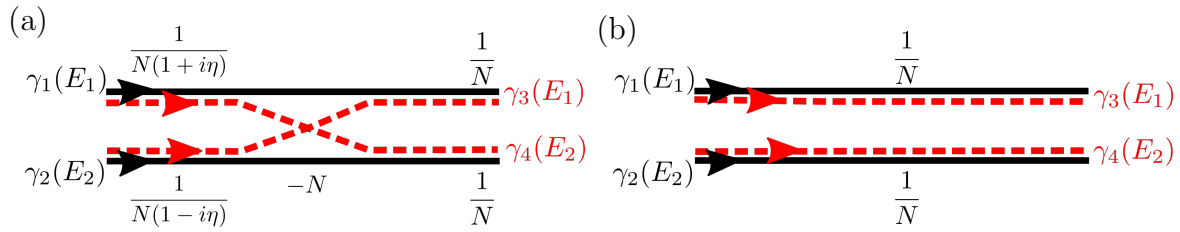

Figure 2.5: First order contributions to D^x and $C^=$. In (a) the quadruplet gives rise to the first term of $D^x(\Delta)$ in Eq. (2.43). The contributions of two links with different energies, the encounter and the two links (with coinciding energies) are resulting in a factor $-N^{-3}(1+\eta^2)^{-1}$. In (b) the first order contribution of $C^=(\Delta)$ is governed by two disconnected pairs sharing the same energy. Therefore the first term in Eq. (2.44), N^{-2} is independent of Δ.

Finally, this energy-independent term can be separated in Eq. (2.44), to reformulate $C^=$ by

$$C^=(\Delta) = \frac{1}{(N+1)^2} + \frac{2}{N^4(1+\eta^2)} - \frac{6\eta^4+24\eta^2+10}{N^5(1+\eta^2)^3} + \mathcal{O}(N^{-6}). \tag{2.47}$$

Our results enable for a prediction of the next order terms for $\Delta = 0$. To estimate $D^x(0)$,

$$\begin{aligned} D^x(0) &= \sum_{i=1}^{\infty} (-1)^i \frac{\mathcal{F}_i}{N^{i+2}} \\ \text{with } \mathcal{F}_0 &= 0; \qquad \mathcal{F}_i = 3\mathcal{F}_{i-1} + 1 \\ \Rightarrow (\mathcal{F}_0, &\mathcal{F}_1, \mathcal{F}_2, \mathcal{F}_3, \dots) = (0, 1, 4, 13, 40, 121, 364, \dots) \end{aligned} \tag{2.48}$$

seems reasonable. In Appendix A.1 we derive a closed form of this series and explicitly show that Eq. (2.48) converge to the RMT result of the COE [28],

$$D^x(0) = -\frac{1}{N(N+1)(N+3)}.$$

In case of the correlators $C^=(0) = B^=(0)$, [28] provides the RMT solution

$$C^=(0) = B^=(0) = \frac{N+2}{N(N+1)(N+3)}. \tag{2.49}$$

By analyzing Eq. (2.44), we suggest the series,

$$\begin{aligned} C^=(0) &= \sum_{i=0}^{\infty} (-1)^i \frac{\mathcal{G}_i}{N^{i+2}} \\ \text{with } \mathcal{G}_0 &= 1; \qquad \mathcal{G}_i = 3\mathcal{G}_{i-1} - 1 \\ \Rightarrow (\mathcal{G}_0, &\mathcal{G}_1, \mathcal{G}_2, \mathcal{G}_3, \dots) = (1, 2, 5, 14, 41, 122, 365, \dots), \end{aligned} \tag{2.50}$$

to coincide with Eq. (2.49). The detailed analysis in Appendix A.1 confirms that, too. For $\Delta \neq 0$, neither for $C^{=}$ nor for D^{x} is a pattern visible, such that higher orders terms are predictable.
The last four-point correlator of interest in the orthogonal case is $B^{=}$, which is governed by

$$\begin{aligned} B^{=}(\Delta) = &-\frac{1}{N^2(i+\eta)^2} + \frac{-2+4i\eta}{N^3(i+\eta)^4} + \frac{32\eta^2+20i\eta-5}{N^4(\eta+i)^6} \\ &+\frac{2\left(-152i\eta^3+99\eta^2+42i\eta-7\right)}{N^5(i+\eta)^8} \\ &+\frac{-3624\eta^4-1720i\eta^3+1140\eta^2+328i\eta-41}{N^6(i+\eta)^{10}} \\ &+\frac{2\left(25192i\eta^5-4516\eta^4-7768i\eta^3\right)}{N^7(i+\eta)^{12}} \\ &+\frac{2\left(2698\eta^2+610i\eta-61\right)}{N^7(i+\eta)^{12}} \\ &+\mathcal{O}(N^{-8}). \end{aligned} \tag{2.51}$$

In principle, $B^{=}$ is complex but for $\Delta = 0$ this correlator reproduces $C^{=}(0)$ as expected. A property, which only D^{x} and $C^{=}$ share, is the alternating sign. In the regime of many open modes, $N \gg 1$, this fact is mostly inconsequential, because terms of increasing order are significantly smaller. Certainly for low N both correlators show drastic oscillations, when considering different truncation orders in $1/N$. The correlator $B^{=}$ does not share this property and is therefore expected to converge faster. We will discuss these characteristics in combination with the correlators achieved in tight-binding implementations later in sec. 2.3.

Last but not least, we also provide the energy-dependent four-point correlators in case of chaotic systems without time-reversal invariance.

Unitary case

The semiclassical approximation of the three correlators is given by

$$D^{x}(\Delta) = -\frac{1}{N^3\left(1+\eta^2\right)} - \frac{2\eta^8+5\eta^6+21\eta^4+3\eta^2+1}{N^5\left(1+\eta^2\right)^5} + \mathcal{O}(N^{-6}), \tag{2.52}$$

$$C^{=}(\Delta) = \frac{1}{N^2} + \frac{1}{N^4\left(1+\eta^2\right)} + \frac{2\eta^8+5\eta^6+21\eta^4+3\eta^2+1}{N^6\left(1+\eta^2\right)^5} + \mathcal{O}(N^{-8}), \tag{2.53}$$

$$B^{=}(\Delta) = -\frac{1}{N^2(i+\eta)^2} + \frac{8\eta^2+4i\eta-1}{N^4(i+\eta)^6} - \frac{180\eta^4+16i\eta^3-32\eta^2-8i\eta+1}{N^6(i+\eta)^{10}} + \mathcal{O}(N^{-8}). \tag{2.54}$$

The alternating sign for D^x and $C^=$, visible in the orthogonal case, is not existing in the unitary case anymore. A series similar to the geometric series,

$$D^x(0) = -\sum_{i=1}^{\infty} N^{-(2i+1)} = N^{-1}\frac{1}{1-\frac{1}{N^2}} = -\frac{1}{(N-1)N(N+1)}, \tag{2.55}$$

is again coinciding with the RMT predictions for CUE from Ref. [28]. For the other two correlators we achieve from Eq. (2.53) again a geometric series,

$$C^=(0) = B^=(0) = \sum_{i=1}^{\infty} N^{-2i} = \frac{1}{1-\frac{1}{N^2}} = \frac{N^2}{(N+1)(N-1)}. \tag{2.56}$$

To complete the topic of approximating the four-point correlators by semiclassical analysis and combinatorics, some remarks are necessary: The previous description is intended for correlators with distinct channels $\{a, b, c, d\}$. When either the in- or the outgoing channels coincide, additionally pairs or quadruplets need to be considered. By doing so also the weak localization and coherent backscattering effects can be described [63, 64].
Another point is the asymptotic expansion we are dealing with: The semiclassical S-matrix in Eq. (2.15) is deduced by applying the stationary-phase approximation (SPA). The SPA is an asymptotic expansion and therefore diverges in general, but a finite number of terms give a reasonable approximation to the exact value [65, 66]. This is the general background of convergence issues for the semiclassical approach. However, generating for a S-matrix correlator stepwise higher orders in $1/N$ by using the diagrammatic rule is not based on SPA. Therefore the convergence of the computed series is expected and for $\Delta = 0$ we explicitly computed the limit.
The last remark we want to make are the cancellation effects when summing the contributions of individual quadruplets. In the unitary class and $\alpha = 4$ there exist according to Table 2.1 nine relevant quadruplets. However, the collective contribution for $C^=(\Delta)$ is only given by $N^{-4}\,(1+\eta^2)^{-1}$. Therefore most summands have to cancel each other out. In case of energy-dependent correlators there exist so far no approach to avoid counting these quadruplets. For energy-independent correlators of the form $\langle T\rangle = \langle t^\dagger t\rangle$ and their moments $M_n = \langle Tr[T^n]\rangle$, in Ref. [67] an improved technique was established[3]. Quadruplets differing only in one encounter (leading to a factor of $-N$) and one link (factor of N^{-1}) cancel out. By recursively converting quadruplets to their partner of cancellation, one obtains a closed form for M_n in accordance to RMT, whereby only relevant quadruplets are kept.

[3]Thereby t is the submatrix of the S-matrix describing only probability amplitudes between two different leads.

2.2.6. Summary

In this section we introduced a semiclassical method to approximate the two-point and four-point energy-dependent S-matrix correlators in a 2D chaotic system, mainly following the powerful machinnery of action correlations to describe quantum interference originally pioneered in Ref. [29,52]. First, we introduced the semiclassical approximation to the S-matrix, where a sum over classical trajectories connecting the leads appear. In sec. 2.2.1 this representation is used to approximate the two-point correlator $C_2(\Delta = 0)$ by identical classical trajectories, called the diagonal approximation, here the action difference of the two classical trajectories vanishes. The next contribution in orders of $1/N$ to $C_2(0)$ is computed for the orthogonal case. Out of it a diagrammatic rule is established, which replaces the problem of calculating the infinite sum over classical trajectory pairs by a pure combinatorical task: Each link (encounter) contributes by a factor of $1/N$ respectively $-N$ to $C_2(0)$. The knowledge about the number of trajectory pairs $\mathcal{N}(\boldsymbol{v})$ for a each encounter structure $\boldsymbol{v}$ yields $C_2(\Delta = 0)$ by Eq. (2.22). To get access to that we first consider periodic orbit pairs. In sec. 2.2.3 the method for generating all available periodic orbit pairs is explained for both symmetry classes. The mapping from periodic orbit pairs to the trajectory pairs relevant for the two-point correlators in the transport setup is specified in sec. 2.2.3, just as the mapping to quadruplets for four-point correlators. We discussed in sec. 2.2.4 the adapted diagrammatic rule for the energy-dependent S-matrices. In case of $C_2(\Delta)$, Eq. (2.35) gives the contribution for each vector $\boldsymbol{v}$. For the four-point correlators, after generating all possible quadruplets, which are characterized by the permutation P in the unitary case or by the tuple $(P_{\text{enc}}, \boldsymbol{\sigma})$ in the orthogonal case, the effect of each individual quadruplet has to be computed separately by extracting their traveling times. In sec. 2.2.5 we first applied the method to achieve the quadruplets for d- and x-families in both symmetry classes, followed by computing the contribution of each quadruplet for the $C^{=}(\Delta)$, $D^{x}(\Delta)$ and $B^{=}(\Delta)$ in the orthogonal case. An appearing alternating sign in D^{x} and $C^{=}$ will be of particular interest in sec. 2.3. The consistency to RMT is also shown for $\Delta = 0$. Finally the semiclassical approximated correlators in case of absent time-reversal symmetry are derived, whereby the agreement to RMT for $\Delta = 0$ is again present.

2.3. Implementations of chaotic cavities providing universal S-matrix correlators

Numerical tight-binding implementations with chaotic cavities display universal S-matrix correlators, therefor several tools are necessary, ranging from boundary shaping to introducing disorder. We will first develop two possibilities of estimating the elastic mean free path of uncorrelated-disordered waveguides in sec. 2.3.1. This enables us in sec. 2.3.2 to introduce a billard-shaped system with weak disorder, where universal correlators are expected. Further improvements in the system shape are preformed in sec. 2.3.3 and are linked to experimental realizations in microwave billiards and RMT data in sec. 2.3.4.

2.3.1. Mean free path in disordered systems

The elastic mean free path l_{el} is an important characteristic of the tight-binding implementation and defines the traveling distance before the initial momentum of the electron is completely randomized [68]. By that, it depends on the disorder strength and the spatial correlation of different disorder sites. Now we will illustrate two methods to estimate l_{el} in 2D for uncorrelated disorder used in the billiard setup. Moreover the methods are also applicable for correlated disorder, e.g. in Ref. [69]. First, by applying Fermi's golden rule we investigate an analytical expression for the mean free path. The second technique uses the averaged transmission or reflection to estimate l_{el} by numerical simulations.

Deducing mean free path by Fermi's golden rule

The elastic scattering time $\tau_k = l_{\mathrm{el}}/v_g$, with v_g being the group velocity, caused by the disorder $V(\boldsymbol{r})$ can be approximated by Fermi's golden rule [70],

$$\begin{aligned} \frac{\hbar}{\tau_k} &= 2\pi \int d\boldsymbol{k}'\ \delta(E_k - E_{k'})|\tilde{V}(k-k')|^2, \\ \tilde{V}(k) &= \frac{1}{A}\int d\boldsymbol{r}\ e^{-i\boldsymbol{k}\cdot\boldsymbol{r}} V(\boldsymbol{r}), \end{aligned} \tag{2.57}$$

with A being the total 2D scattering area. For the chosen uncorrelated case, disorder is expressible in terms of Heaviside step functions $\Theta(\dots)$ by

$$V(\boldsymbol{r}) = V_0 \sum_{i=1}^{N} \alpha_i \Theta\left(\frac{a}{2} - |x|\right)\ \Theta\left(\frac{a}{2} - |y|\right)$$

with $V_0 > 0$ characterizing the strength of the disorder, $\alpha_i \in [-1, 1]$ being a random number and N describing the number of sites in the area A with the lattice constant a.

Evaluating $\tilde{V}(k)$ and using the assumption of low energies $ka \ll 1$, it follows [71]

$$\begin{aligned}\tilde{V}(k) &= \frac{V_0}{A}\sum_{i=1}^{N}\alpha_i \int_{-a/2}^{a/2} dx\, e^{-ik_x x}\int_{-a/2}^{a/2} dy\, e^{-ik_y y} \\ &= \frac{V_0}{A}\sum_{i=1}^{N}\alpha_i \left(\frac{2}{k}\sin(ka/2)\right)^2 \\ &\approx \frac{V_0}{A}\sum_{i=1}^{N}\alpha_i a^2. \end{aligned} \tag{2.58}$$

Inserting Eq. (2.58) into Eq. (2.57) yields

$$\begin{aligned}\frac{\hbar}{\tau_k} &= \frac{2\pi V_0^2 a^4}{A^2}\left|\sum_{i=1}^{N}\alpha_i\right|^2 \int d\boldsymbol{k}'\, \delta(E_k - E_{k'}) \\ &= \frac{2\pi V_0^2 a^4}{A^2}\left|\sum_{i=1}^{N}\alpha_i\right|^2 D(E_k), \end{aligned} \tag{2.59}$$

with the density of states $D(E_k)$. The randomness of $\lim\limits_{N\to\infty}\frac{1}{N}\sum_{i=1}^{N}\alpha_i = 0$ allows us to approximate

$$\begin{aligned}\left|\sum_{i=1}^{N}\alpha_i\right|^2 &\overset{\alpha_i\in\mathcal{R}}{=} \left(\sum_{i=1}^{N}\alpha_i\right)^2 = \sum_{i=1}^{N}\alpha_i^2 + \sum_{i=1}^{N}\alpha_i\sum_{j\neq i}^{N}\alpha_j \\ &= N\left[\frac{1}{N}\sum_{i=1}^{N}\alpha_i^2 + \frac{1}{N}\sum_{i=1}^{N}\alpha_i\sum_{j\neq i}^{N}\alpha_j\right] \\ &\overset{N\gg 1}{\approx} \sum_{i=1}^{N}\alpha_i^2. \end{aligned}$$

The elastic mean free path is then deduced from

$$\begin{aligned}&\frac{\hbar}{\tau_k} = \frac{2\pi V_0^2 a^4}{A^2} D(E_k)\sum_{i=1}^{N}\alpha_i^2 = \frac{2V_0^2 A m^*}{\hbar^2 N^2}\sum_{i=1}^{N}\alpha_i^2, \\ &\Rightarrow l_{\mathrm{el}} = \frac{\hbar^2 N k}{V_0^2 a^2 m^*}\left(\sum_{i=1}^{N}\alpha_i^2\right)^{-1}, \end{aligned} \tag{2.60}$$

by substituting $A = Na^2$ and for the 2DEG the density of states $D(E_k) = Am^*/(\pi\hbar^2)$ and the group velocity $v_g = 2k/\hbar$. To conclude, the elastic mean free path l_{el} for a 2DEG with uncorrelated disorder is given by Eq. (2.60) and is thereby proportional to V_0^{-2}.

Determine mean free path by averaged transmission/reflection

Another method, applicable also for correlated disorder where no closed analytic form can be achieved, is based on the system length L dependency of the transmission and reflection coefficients [68, p. 203]:

$$\langle T\rangle = \Big\langle \frac{l}{L+l} - \frac{1}{N}\frac{L}{L+l}\Big\rangle, \qquad \langle R\rangle = \Big\langle \frac{L}{L+l} + \frac{1}{N}\frac{L}{L+l}\Big\rangle, \tag{2.61}$$

where the transmission T (reflection R) is averaged over different disorder configurations $\langle \dots \rangle$, N is the number of open modes and l being the characteristic length of the order of the mean free path l_{el} with the condition $L \gg l_{\mathrm{el}}$. Due to the weak localization effect the transmission (reflection) is reduced (increased) compared to the classical expectation. Implementing a waveguide using tight-binding method and computing the averaged transmission or reflection coefficient is then determining l_{el} by solving Eqs. (2.61)

$$l_{\mathrm{el}} \approx L\,\frac{\langle T\rangle + \frac{1}{N}}{1-\langle T\rangle} = \frac{L}{\langle R\rangle}\left(1+\frac{1}{N}-\langle R\rangle\right). \tag{2.62}$$

To conclude, we are able to determine the mean free path l_{el} for the uncorrelated disorder analytically by Eq. (2.60) or by numerical simulations using Eq. (2.62).

2.3.2. Cavity with smooth boundary

All numerical simulations are preformed using the tight-binding approach and the Kwant code [72]. We implement the 2DEG by the Hamiltonian $\hat{H} = \frac{\hbar^2}{2m_e}\boldsymbol{k}^2$ with the preserved time-reversal symmetry $\mathcal{T}^2 = 1$ and free electron mass m_e. Connecting a scattering region to two metallic contacts (leads) provides access to scattering properties by solving the underlying problem using the wave function approach [72]. One crucial adjustment in the Kwant code is thereby necessary: The lead transversal functions $\psi_n(y)$ are in general defined except for a multiplicative phase. In Kwant, for each energy this phases are random and thus the phases in the S-matrix, too. Observables, which are independent on the phase of $S_{b,a}(E)$ at different energies are not affected by that. Here on the contrary, this correlations are essential and we need to adjust the code for that. We redefine the transversal function by $\psi_n(y) \to \psi_n(y)e^{-i\zeta_n}$ with $\zeta_n = \phi\big(\langle\psi_n^*(y)|\psi_n(y)\rangle\big)/2$, whereby $\phi(\dots)$ gives the phase of the argument. It is important to note that this is only appropriate as long as transversal functions at different energies are not linked by physical relevant phases. In the case of the 2DEG, the transversal functions are given by Eq. (2.2) and are independent on the energy, such that this amendment is applicable and gives in general access to energy-dependent S-matrix correlations.

Now we can focus on shaping an adequate system. In Fig. 2.6(a) we sketch a system, for which we expect in the classical limit an ergodic and chaotic motion. To avoid direct paths between the two leads (red) we implemented a circular-formed obstacle. Additionally to that, uncorrelated weak disorder ($k_F \cdot l_{\mathrm{el}} \gg 1$) is introduced, such that the resulting elastic mean free path l_{el} is fulfilling the condition of ballistic scattering

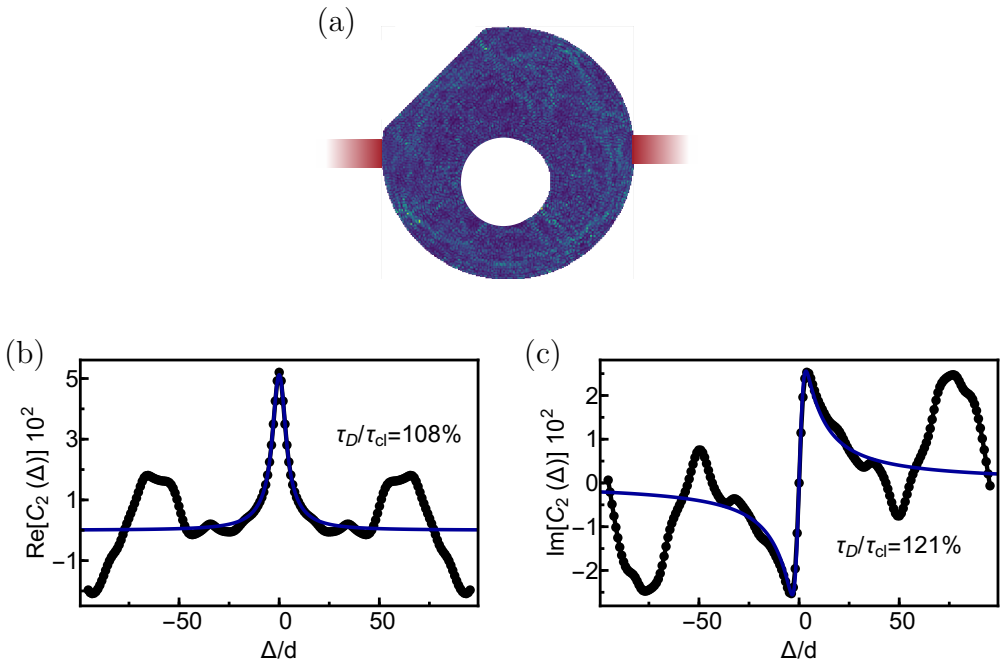

Figure 2.6: The two-point correlator $C_2(\Delta)$ of the sketched system with $N = 20$ features partial agreement to the semiclassical approach. (a) illustrates the system form and a representative LDOS, whereby bright (dark blue) spots correspond to high (low) densities. The numerical achieved real and imaginary part of $C_2(\Delta)$ (black) in (b) and (c) agree after the fitting of τ_D with the semiclassical prediction (blue) from Eq. (2.36) for $\Delta/d \lesssim 25$. Strong oscillations for $\Delta/d \gtrsim 25$ are present when 3000 averages (over $\bar{E}$ and disorder configurations) are performed.

($\lambda_F < L < l_{\mathrm{el}}$) in the non-localized regime ($L \lesssim N \cdot l_{\mathrm{el}}$) with $N = 20$ being the number of open modes and L the system length. Therefor we applied the methods introduced in subsec. 2.3.1 to get access to l_{el}. In Fig. 2.6(a) the local density of states (LDOS) is plotted, whereby high (low) intensities are given by bright (dark blue) spots. The smooth and uniform distribution supports the assumed ergodicity. The classical dwell time $\tau_{\mathrm{cl}} = \frac{\pi \mathcal{A}}{v_g \mathcal{C}}$, with scattering area $\mathcal{A}$, group velocity v_g and lead width $\mathcal{C}$ therefor seems to exceed the Ehrenfest time $\tau_{\mathrm{E}} \propto \frac{L}{\lambda_F}$. In this configuration τ_{cl} is given by $\tau_{\mathrm{cl}} \approx 11 \tau_{\mathrm{pass}}$ with $\tau_{\mathrm{pass}} = v_g L$. Asides from that, sec. 2.2 teaches us that a chaotic system experiences universal two- and four-point S-matrix correlations. The semiclassical approach of the two-point correlator $C_2(\Delta)$ in Eq. (2.36) with the first energy-dependent term proportional to N^{-1} is a landmark for chaotic scattering. The four-point correlators of interest contain at least energy-depended summands proportional to N^{-2}, such that a worse signal/noise ratio is expected.
To start with, the C_2 correlator,

$$C_2(\Delta) = \langle S_{b,a}(\bar{E} + \Delta) S^*_{b,a}(\bar{E} - \Delta) \rangle, \tag{2.63}$$

with averages over 300 different mean energies $\bar{E}$ and 100 disorder configurations is computed. We choose here one channel combination $(a, b) = (0, 1)$, but the correlators for different channels (a, b) share the same general form. The real and imaginary parts are plotted in Fig. 2.6(b) and (c) in black, with a rescaled axis by $d = \frac{\hbar^2}{m_e \mathcal{A}}$ being the mean level spacing. The fit of the dwell time τ_D in Eq. (2.36) to this data yields the semiclassical prediction plotted in blue. For $\Delta/d \leq 25$ the alignment of the semiclassical approach and the numerical data is visible. However, for bigger energy differences the data exhibits still drastic oscillations.

This lack of perfect agreement makes it reasonable to study further properties in connection to chaos, e.g. the statistical nature of the appearing S-matrices. For off-diagonal elements $S_{b,a}$ with $a \neq b$ a bivariate Gaussian distribution,

$$\begin{aligned} P(s) &= \frac{\pi}{2} s \exp\left[-\frac{\pi}{4} s^2\right], \\ P(\phi(S_{b,a})) &= \frac{1}{2\pi} \end{aligned} \tag{2.64}$$

with $s = |S_{b,a}| / \sqrt{\langle |S_{b,a}|^2 \rangle}$ is expected due to RMT [73–76]. The range of validity is given by the Ericson regime, $\Gamma/d \gg 1$ [77] this means that the average level width Γ in the cavity is much greater than the mean level spacing $d = \frac{\hbar^2}{m_e \mathcal{A}}$. Using $\Gamma \approx \hbar/\tau_{\mathrm{cl}}$ gives $\Gamma/d \approx 18$ and therefore legitimate Eq. (2.64) in our setup[4]. In Fig. 2.7 both, the RMT prediction (red) from Eq. (2.64) and histograms of $s_{b,a}$ and $\phi(S_{b,a})$ for almost $50 \cdot 10^3$ different S-matrices are compared. The agreement to a bivariate Gaussian distribution for absolute values of $S_{b,a}$ is visible in Figs. 2.7(a), (b). The uniform distribution of phases in (c) and (d) is in accordance with RMT plotted in red.

[4] An analytical result of the modulus and the phase of the S-matrix outside of the Ericson regime can be found in Ref. [78]. The statistic of $S_{a,a}$ is a bivariate Gaussian, too, as long as $\Gamma/d \gg 1$ and $|\langle S_{a,a} \rangle| \ll 1$ [79–81].

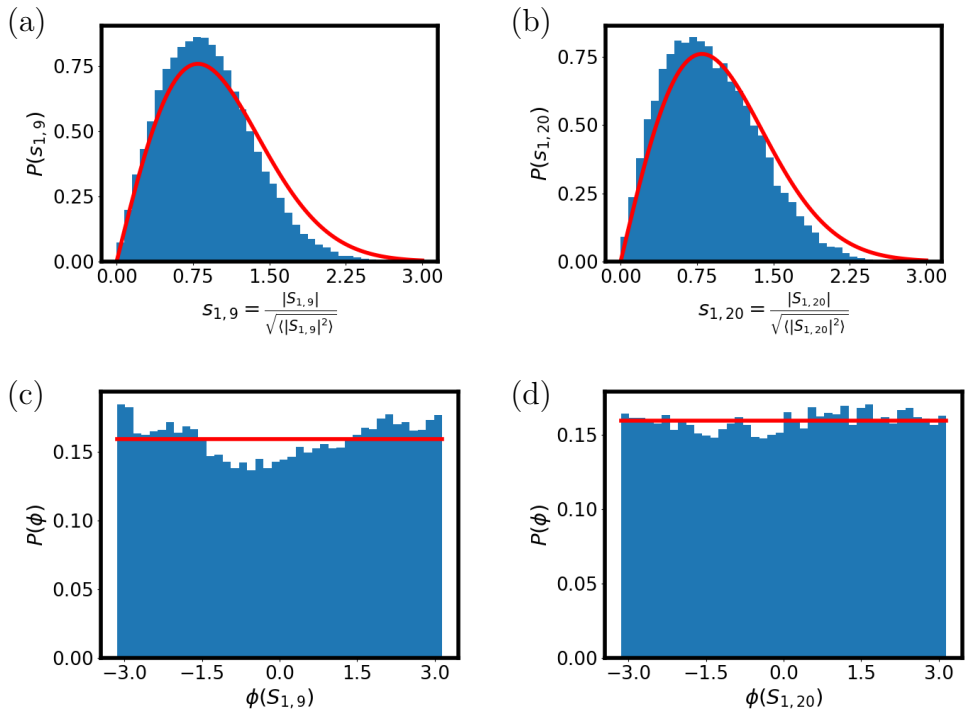

Figure 2.7: Comparison of RMT predictions with numerical S-matrix statistics. In (a) and (b) the histograms of the unfolded $s_{b,a}$ values (blue) for two channel combinations, $(b, a) = (1, 9), (1, 20)$ agree with bivariate Gaussian distributions of orthogonal matrices from Eq. (2.64). The uniform distributions of the phases $\phi(S_{b,a})$ in (c) and (d) is in accordance with RMT, too.

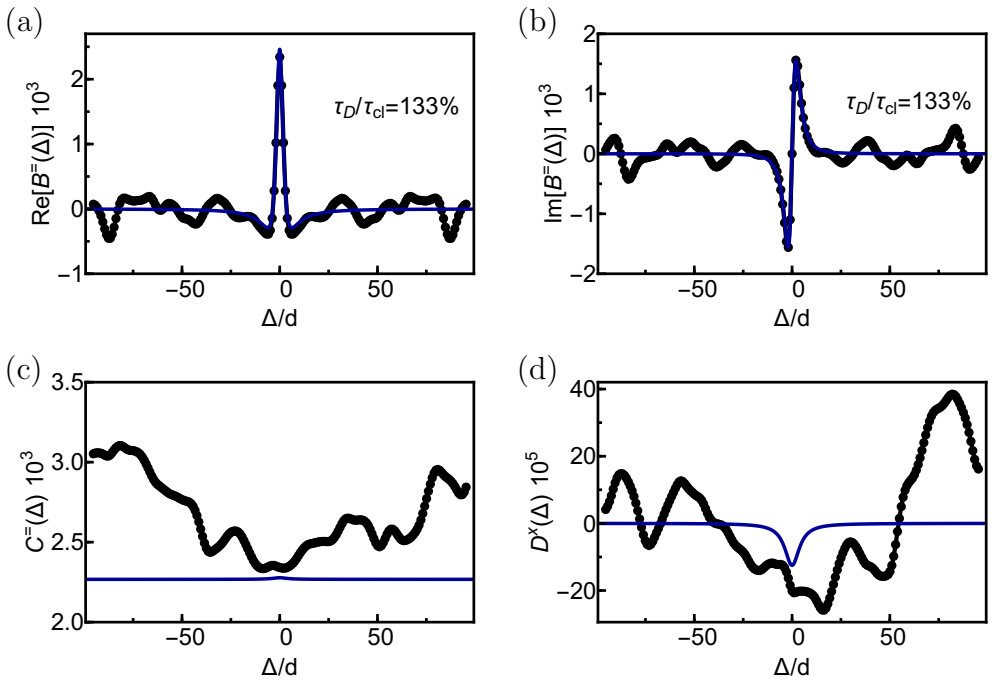

Figure 2.8: Numerical results for energy-dependent four-point correlators in comparison to semiclassical analysis. The fast convergence of $B^=(\Delta)$ originates the alignment of real and imaginary part (black) with the dwell time adapted to the semiclassical series (blue) in Eq. (2.51), illustrated in (a) and (b). Both numerical correlators (black), $C^=(\Delta)$ in (c) and $D^x(\Delta)$ in (d) exhibit a discrepancy to semiclassical predictions (blue), whereby Eqs. (2.43), (2.44) are plotted with $\tau_D = \tau_{\rm cl}$.

Thus the S-matrix statistics support the general assumption of chaotic behavior. To proceed, we analyze the four-point correlators with the same averaging process as used for $C_2(\Delta)$. In Figs. 2.8(a), (b) the real and imaginary parts of the $B^=(\Delta)$ correlator are plotted in black. A dwell time fitting of the semiclassical formula from Eq. (2.51) (blue), yields reasonable agreements. It illustrates the alignment for small energy differences and the low oscillation amplitude for larger Δ/d. Compared to the $C_2(\Delta)$ in Figs. 2.6(b) and (c), $B^=(\Delta)$ exhibits lower undulations for $\Delta/d > 25$. For $C^=(\Delta)$ and $D^x(\Delta)$ the numerical data (black) in Figs. 2.8(c) and (d) are not described by Eq. (2.43) and (2.44).

In (c) and (d) the semiclassical predictions (blue) with $\tau_D = \tau_{\rm cl}$ are illustrating these discrepancies. Our assumption that the correlators with increased $1/N$ order dependency show worse signal/noise ratios is partly confirmed, with the exception of $B^=(\Delta)$ in Fig. 2.8(a)-(b). In comparison to $C_2(\Delta)$ in Fig. 2.6(a)-(b) a faster convergence of $B^=$ to the semiclassical predictions in the hole range of Δ/d is visible. To progress in reaching universal forms of $C_2(\Delta)$ and in particular $C^=(\Delta)$ and $D^x(\Delta)$ an increase of number of averages seems reasonable. However, beforehand we will improve the system shape.

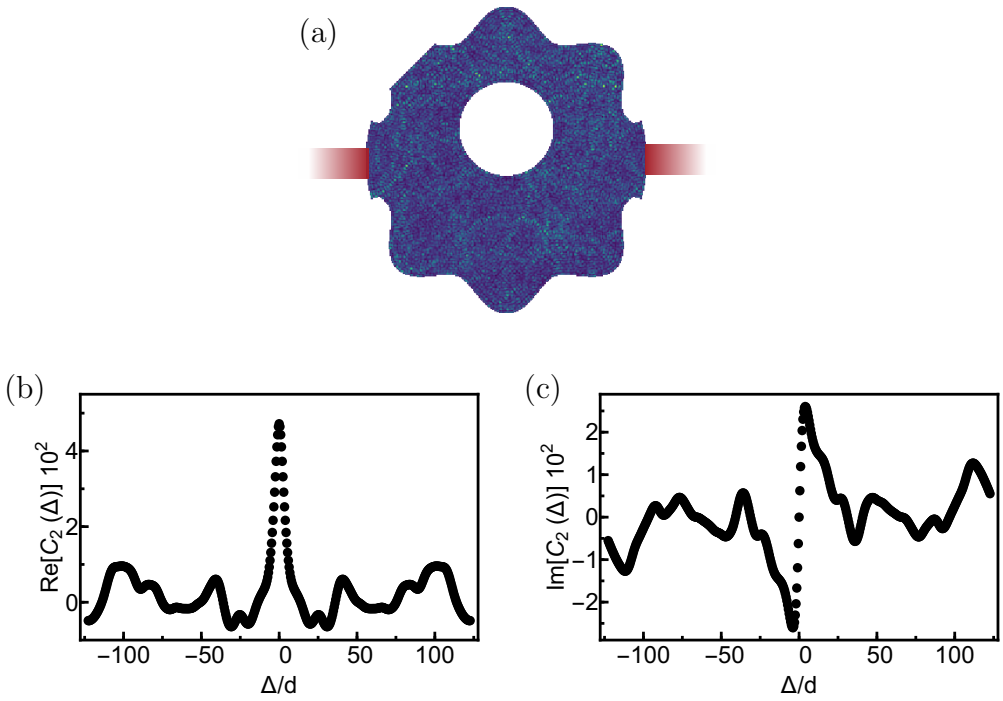

Figure 2.9: Adaption of the cavity to an undulating boundary yields less fluctuations in $C_2(\Delta)$. The real (a) and imaginary part (b) of $C_2(\Delta)$ for $N = 20$ and almost 3000 averages are less undulating compared to a Fig. 2.6(b)-(c).

2.3.3. Cavity with undulating boundary

The cavity constraint by a smooth boundary is now replaced by an undulating boundary as sketched in Fig. 2.9(a) with an representative LDOS again directly included. All system parameters besides the boundary form and the position of the obstacle are adopted from the previous system. $C_2(\Delta)$ is computed by the same averaging process as done in Fig. 2.6(b)-(c) and we illustrate it in Fig. 2.9(b)-(c) (black) separated in real and imaginary parts. The detailed comparison of the two-point correlators shows that the undulations for energies $\Delta/d > 25$ (where the semiclassical prediction yields zero) are lower for the system with an undulating boundary compared to the smooth one. Therefore the new system form improves the chaotic properties in the cavity.

Now we preform another adjustment, namely shrinking the lead widths such that the classical dwell time τ_{cl} is doubled compared to the previous setup with $\tau_{\mathrm{cl}} \approx 22\tau_{\mathrm{pass}}$. Then the correlators of interest are according to Eqs. (2.36), (2.43)-(2.44) and (2.51) exhibit a Lorentzian form of smaller width. Applying the same average leads to an two-point correlator in Fig. 2.10(a)-(b). The increased signal/noise ratio compared to Fig. 2.9(b)-(c) is justified by the $1/N$ dependency in semiclassical series. With this adjusted system parameters we preform further averages to generate two-point and four-point correlators where the forms predicted by the semiclassical approach is identifiable. In Fig. 2.10(c-d) the numerical results (circles) for $C_2(\Delta)$ agree with semiclassical predictions (line).

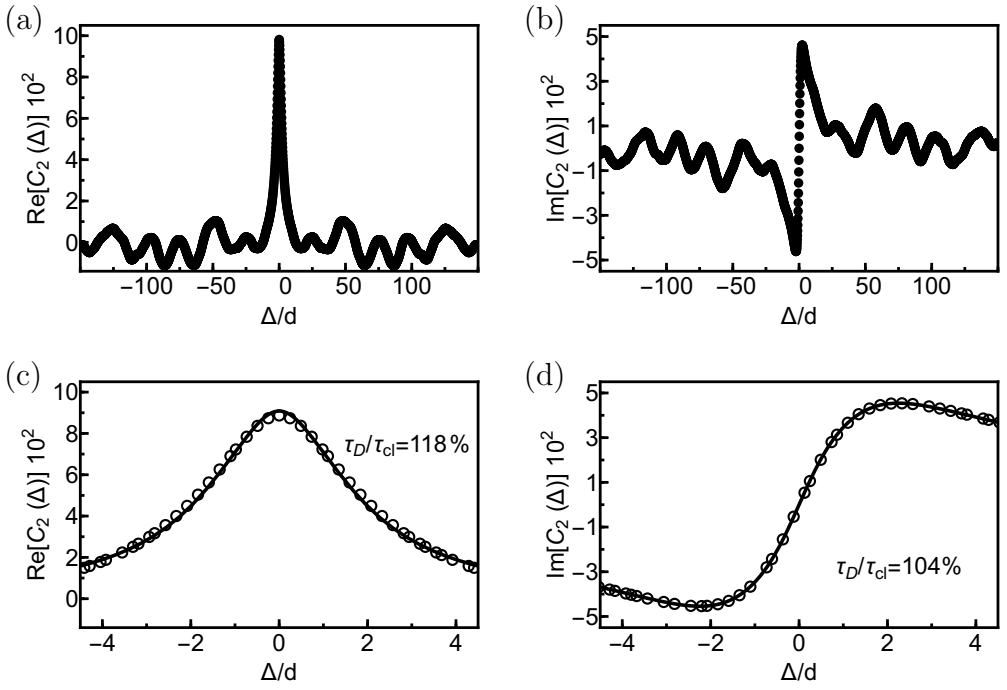

Figure 2.10: The system form of Fig. 2.9(a) with reduced lead widths yields $N = 10$ and a less undulating two-point correlator. The signal/noise ratio is reduced, whereby in (a) and (b) the real and imaginary part of the expected $C_2(\Delta)$ form is more pronounced. Averages over $3.5 \cdot 10^3$ mean energies, 100 disorder configurations and all possible channel combinations yield smooth real and imaginary parts of $C_2(\Delta)$ in (c) and (d) (circles). These are in excellent agreement to Eq. (2.36) (line).

Therefor in total $3.1 \cdot 10^7$ averages including varying $\bar{E}$, disorder and channel combination are preformed. Computing the four-point correlators also by including these strong averages, Fig. 2.11 illustrates the resulting data. The fast converging $B^{=}(\Delta)$ (circles) is in very good agreement with the semiclassical fit (line) for real and imaginary part plotted in (a) and (b). In Fig. 2.11(c)-(d) the numerical data for $C^{=}(\Delta)$ and $D^{x}(\Delta)$ (circles) reached a form, such that it coincides with expectations (line).

Reaching the low N limit

So far the semiclassical approach of the energy-dependent S-matrix correlators by series in orders of $1/N$ was explored for $N \gg 1$. Now we will investigate the numerical correlators and the semiclassical expansion for the lowest number of open modes possible, $N = 4$. Due to the restriction on distinct channels (a, b, c, d), the four-point correlators for $N < 4$ are given by additional diagrams and therefore experience a different form. The lead widths of the tight-binding setup is now reduced such that $N = 4$ propagating modes are available. By averaging over mean energies, disorder configurations and all available channel combinations, the smooth form of the three correlators of interest are

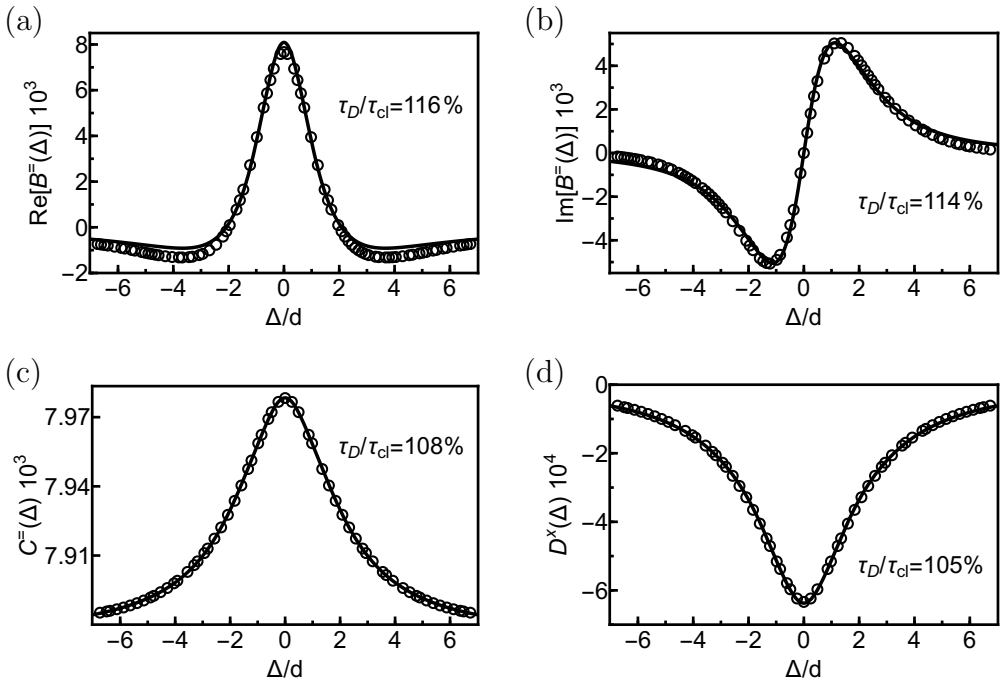

Figure 2.11: The billiard-shaped system with the undulating boundary and $N = 10$ yields four-point correlators of expected form. Adapting τ_D of the semiclassical predictions (line) to numerical results (circles) of $B^{=}(\Delta)$ for real (a) and imaginary part (b) gives convincing agreement. The same holds for $C^{=}(\Delta)$ and $D^{x}(\Delta)$ in (c) and (d).

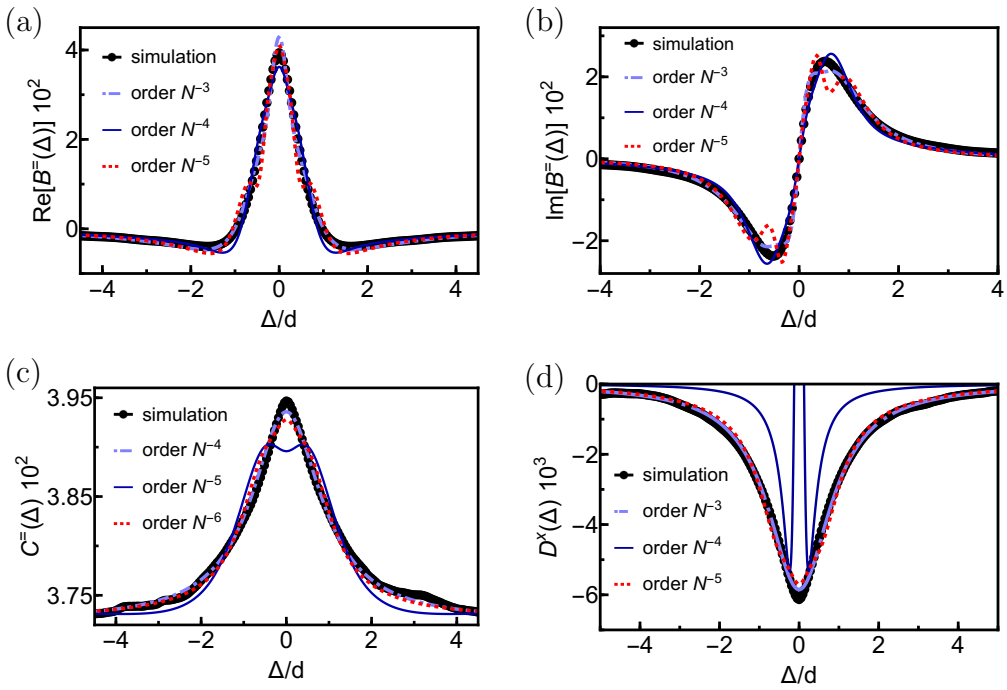

Figure 2.12: For $N = 4$, the numerical four-point correlators are partly aligned with semiclassical predictions. (a) and (b) show, that for $N = 4$ the $B^{=}(\Delta)$ convergence, such that all truncations of Eq. (2.51) align with numerical results of real and imaginary part (black). The alternating signs in Eqs. (2.43), (2.44) leads to undulations for different truncations in $C^{=}$ and D^{x}. Nevertheless, (c) and (d) illustrate the agreement of $C^{=}(\Delta)$ and $D^{x}(\Delta)$ correlators to simulations, when an uneven number of summands are devoted.

plotted in black in Fig. 2.12. For different truncations of the $1/N$ sums, the formula for $B^{=}(\Delta)$ is illustrated for real and imaginary part in (a) and (b). Thereby the dwell time τ_D and a multiplicative factor are fitted. The different truncations share the same over all agreement to numerics, besides on small differences. In case of $C^{=}(\Delta)$ and $D^{x}(\Delta)$ this changes. The alternating signs in Eqs. (2.43)-(2.44) are causing cancellations of summands and indicating slow convergence of the semiclassical expectation for every second term. The same fitting of τ_D and prefactors leads then to undulations for even number of terms, such that no satisfying alignment to the numerics is available. However, fitting of every uneven number of terms gives an approximation as illustrated by the blue dashed and red dashed lines in Fig. 2.12(c)-(d).

2.3.4. Comparison to microwave billiards and the Heidelberg approach

Besides the discussed methods, the semiclassical approach and the numerical tight-binding simulations, two more possibilities of studying universal energy-dependent S-matrix correlators are investigated in our manuscript [53]: The Heidelberg approach within RMT and the experimental realization by microwave billiards.

The former uses random k-dependent Hamiltonians $H(\boldsymbol{k})$,

$$H(\boldsymbol{k}) = \boldsymbol{k}\mathbb{1} - \mathcal{H},$$

whereby $\mathcal{H}$ is a $M \times M$-dimensional random matrix of the GOE. The S-matrix is then given by

$$\begin{aligned} S_{b,a}(E) &= \delta_{b,a} - 2\pi i \Gamma_{b,a}, \\ \Gamma &= W^\dagger \big(H(\boldsymbol{k}) + i\pi W W^\dagger\big)^{-1} W. \end{aligned} \tag{2.65}$$

Here the coupling between the system, described by the hermitian matrix $H(k)$ and the leads is represented by the $M \times N$ real matrix W with Gaussian distributed entries with zero mean [82]. The poles of $S_{b,a}$ are then coinciding with eigenvalues of the effective Hamiltonian of the open system $\mathcal{H}(\boldsymbol{k}) + i\pi W W^\dagger$. The Bohigas-Giannoni-Schmidt conjecture confirms the accordance between these RMT originated eigenvalues and the ones arising in chaotic systems [83].

The latter one is an experimental realization by microwave billiards, which uses the equivalence between the 2D Schrödinger equation with Dirichlet boundary conditions to the stationary Helmholtz equation [70]

$$-\Big(\frac{\partial^2}{\partial x^2} + \frac{\partial^2}{\partial y^2}\Big)\chi_n = \frac{\omega_n^2}{c^2}\chi_n, \tag{2.66}$$

with speed of light c [84–86]. The electric field amplitude χ_n has to vanish at the boundary in the same way as the electronic counterpart. The cavity is formed by metallic plates and the coupling to leads is established by $N = 4$ antennas with microwave cables attached[5]. By fitting the two-point correlator $C_2(\Delta)$ to the experimental data, one finds a total number of open modes $N \approx 9 - 10$. The experimental data is comparable to quantum graphs when absorption is introduced by a small imaginary part of wavenumber k [82]. In Fig. 2.13 the experimental four-point correlators are plotted (black dots) and indicate agreement to fits of the semiclassical predictions (black lines) for all four-point correlators. In analogue to our previous investigations a rescaled value $\epsilon = \Delta/D$, with resonance spacing D of the quantum graph is used. Again the experiments show for $B^=(\Delta)$ a faster convergence in comparison to $C^=(\Delta)$ or $D^x(\Delta)$. Fig. 2.13 also illustrates the RMT result using the Heidelberg approach (red dots) in comparison to semiclassical adapted formulas (red lines) for $N = 4$ (with additional absorption) or $N \approx 9 - 10$

[5] For frequencies lower than $\frac{c}{2d}$, with d being the distance of two plates in z-direction, the 2D Helmholtz equation in Eq. (2.66) is valid.

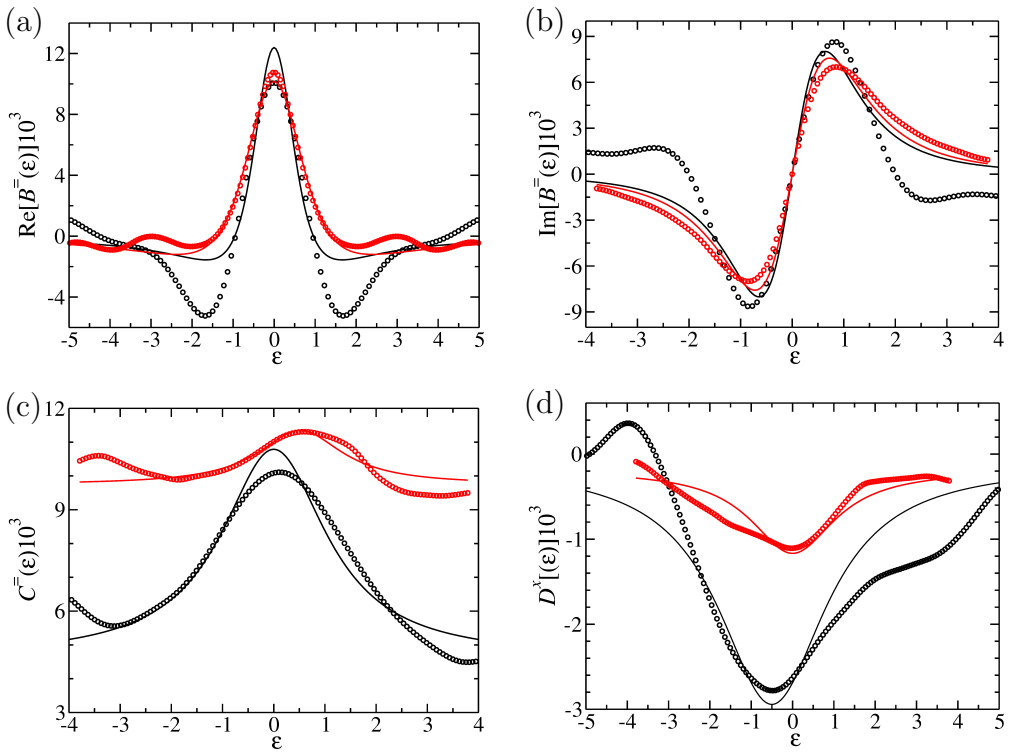

Figure 2.13: The data achieved from experimental microwave billiards (black dots) coincide with semiclassics (black lines) with $N \approx 9 - 10$, while fitting the dwell time and a prefactor for $B^{=}(\Delta)$, $C^{=}(\Delta)$ and $D^{x}(\Delta)$. The RMT results in the Heidelberg approach (red dots) agree also with semiclassical analyzes (red lines) from Eqs. (2.43), (2.44) and (2.51) with $N = 9$.

(without absorption). Here, also the RMT data show the best convergence for $B^{=}(\Delta)$. Therefore the fast convergence of $B^{=}$ in comparison to C_2 and other four-point correlators is undeniable. It seems thereby symptomatic, that all investigated methods share the same convergence properties for S-matrix correlations.

2.4. Summary

In this chapter we investigated correlations in chaotic systems relevant for EQO of HOM-type by semiclassical and numerical investigations, published in Ref. [53]. In sec. 2.1 we introduced the studied system and linked the two-particle probability to four-point S-matrix correlations following Ref. [23]. To compute the relevant energy-dependent four-point S-matrix correlators, the basic idea and state of art is provided in Ref. [29, 52, 62]: The semiclassical approach to the S-matrix yields a summation of classical trajectories. Therefore in two-point correlators trajectory pairs and in four-point correlators quadruplets are the relevant objects to consider. From this starting point, we investigate the complex combinatorics of these objects, such that our implemented method can deal with large number of relevant trajectories and therefore provides an approximation for low number N of open modes. Correlators with a known first order approximation are thus computed to significant higher accuracy. In addition we investigate an four-point S-matrix correlator where so far not any approximations are available. In sec. 2.2 we describe the computation by stepwise increasing the complexity of S-matrix correlators, from energy-independent two-point correlators to energy-dependent four-point ones, leading to an applicable technique to evaluate the correlators semiclassically. Finally, in sec. 2.2.5 a series expansion in $1/N$ for the four-point S-matrix correlators is achieved. For each order in $1/N$ we provide for both, unitary and orthogonal symmetry class the number of contributing quadruplets. Out of that, the four-point correlators are computed up to N^{-7} (orthogonal case) or N^{-6} (unitary case). Besides the pure computational results, sketches of quadruplets given rise to the first order contributions to $D^x(\Delta)$ and $C^=(\Delta)$ are provided us with an intuitive picture. The large amount of contributions is on the one hand dealing with a large number of semiclassical diagrams, on the other hand enabled us to predict an infinite series for vanishing energy difference. We prove the convergence of these series to RMT predictions for all investigated correlators in both symmetry classes, orthogonal and unitary.
Besides this analytical approach, we established numerical tight-binding systems in billiard-shaped form, where universal signatures of quantum chaos are expected. To begin with, two methods of approximating the mean free path of (uncorrelated white) disorder are introduced, by that we were able in sec. 2.3.3 the system with weak disorder and a smooth boundary was implemented. By means of a phase correction of the transversal lead modes, we have access to energy-dependent S-matrices in tight-binding setups. Both, the alignment of an energy-dependent two-point correlator to semiclassical predictions and the agreement of S-matrix statistics to RMT are the first promising observations. By replacing the boundary by an undulating one, the two-point and the four-point correlators agree excellently with the semiclassical expansions. When reaching the low number of open modes regime the numerical correlators are still pronounced. The numerical fast converging correlator $B^=(\Delta)$ also exhibits convergence in different truncations of the semiclassical $1/N$ series. In contrast thereto, the alternating signs in the semiclassical expansions of the other four-point correlators are producing undulations for different truncations. Nevertheless the semiclassical predictions are in agreement with simulations when only considering uneven number of summands. By comparing

these results with data of a collaborating group in experimental microwave billiards and applying the Heidelberg approach in sec. 2.3.4, we exhaust all known techniques of describing universal energy-dependent S-matrix correlations.

3. Universal S-matrix correlations in topological insulators

In this chapter we will investigate universal S-matrix correlations, whereby the edge states of a topological insulator (TI) serve as waveguides, the detailed analysis for systems in the symmetry class AI in chap. 2 paves the way. The realization of the Hong-Ou-Mandel (HOM) effect in an quantum point contact (QPC) using chiral edge states arising from the integer quantum Hall effect is a keystone on the experimental side of EQO [87,88]. However, only one study in the context of chaos in TIs is present [89]. To start the discussion of this intermediate research field, in sec. 3.1 we solve for an infinite waveguide the corresponding Schrödinger equation, whereby the TI Hamiltonian is given by the Bernevig-Hughes-Zhang (BHZ) Hamiltonian [90]. The governing information enables us to adjust our numerical tight-binding model, such that the energy dependency of S-matrices is achievable. The formalism of many-body scattering theory in sec. 2.1 disregards the effects arising from the Fermi sea inclusion, moreover, it lacks the property of experimental measurability. To bypass these issues we extend and adjust in sec. 3.2 the electronic coherence formalism introduced in Ref. [87, 91, 92] to energy-dependent S-matrices resulting in a current-current correlation of HOM-type $\Delta\bar{Q}_{\mathrm{HOM}}$. This preliminary work enables in sec. 3.3 the numerical computation of energy-dependent S-matrix corre-lations. In contrast to chap. 1 in which the Hamiltonian symmetry is of the COE, here we will concentrate on (broken) time-reversal symmetry with (without) $\mathcal{T}^2 = -1$. In sec. 3.3.3 the consequence of the correlator on $\Delta\bar{Q}_{\mathrm{HOM}}$ is consolidated.

3.1. Topological insulator waveguide

In the previous chapter, a phase correction of the transversal modes in the Kwant code was necessary, such that phase correlations of S-matrices were accessible. In accordance thereto such an intervention is also required when studying S-matrix correlations in TIs. Therefore we first deduce the solution of a TI waveguide and analyze the properties arising from time-reversal symmetry. The phase relation of transversal modes will afterwards specify the necessary correction.

The 2D BHZ-Hamiltonian in the basis of the electron and hole bands $|E1,\uparrow>, |H1,\uparrow>, |E1,\downarrow>$ and $|H1,\downarrow>$ is given by [90]

$$\hat{H}_{\mathrm{BHZ}} = \begin{pmatrix} \hat{h}_{2x2}(\hat{\boldsymbol{k}}) & \begin{matrix} 0 & -\Delta \\ \Delta & 0 \end{matrix} \\ \begin{matrix} 0 & \Delta \\ -\Delta & 0 \end{matrix} & \hat{h}^{*}_{2x2}(-\hat{\boldsymbol{k}}) \end{pmatrix} \tag{3.1}$$

with

$$\hat{h}_{2x2}(\hat{\boldsymbol{k}}) = \begin{pmatrix} C - (B+D)\hat{\boldsymbol{k}}^2 + M & A(\hat{k}_x + i\hat{k}_y) \\ A(\hat{k}_x - i\hat{k}_y) & C + (B-D)\hat{\boldsymbol{k}}^2 - M \end{pmatrix}, \tag{3.2}$$

$\hat{\boldsymbol{k}}^2 = \hat{k}_x^2 + \hat{k}_y^2$ and the default parameters given in Table 3.1.

A[meVnm]	B[meVnm^2]	C[meV]
364.5	-686	0

M[meV]	D[meVnm^2]	Δ[meV]
-10	-512	0

Table 3.1: The default values of the BHZ-Hamiltonian parameters are mostly penned by Ref. [90]. However, the influence of the bulk inversion asymmetry, accomplished in lowest order by the Dresselhaus spin-orbit coupling Δ, will as default be set to zero [93].

The goal is to solve the Schrödinger equation $\hat{H}_{\mathrm{BHZ}}\boldsymbol{\psi} = E\boldsymbol{\psi}$ for a 2D waveguide system with hard wall boundary conditions in y-direction, $|\boldsymbol{\psi}(x, y = \pm W/2)|^2 = 0$ and translation invariance in x-direction as depicted in Fig. 3.1(a). From now on we assume a vanishing spin-orbit coupling, $\Delta = 0$, which facilitates the situation by uncoupling the spin blocks. We first concentrate on the spin $|\uparrow\rangle$ electrons and later we will take the spin $|\downarrow\rangle$ also into account.
First imagine a system, which is infinite in $x-$ and y-direction. The plane wave ansatz

$$e^{ik_x x} e^{ik_y y} \boldsymbol{\phi}_{\uparrow}(k_x, k_y)$$

for solving

$$\hat{h}_{2x2}\, e^{ik_x x}\, \boldsymbol{\chi}_{\uparrow,E}(k_x) = E\, e^{ik_x x}\, \boldsymbol{\chi}_{\uparrow,E}(k_x) \tag{3.3}$$

results in four eigenvectors ($i \in \{1,2,3,4\}$)

$$\boldsymbol{\phi}_{\uparrow,i}(k_x, k_{y,i}) = \begin{pmatrix} a_i(k_x, k_{y,i}) \\ b_i(k_x, k_{y,i}) \end{pmatrix} = \begin{pmatrix} -M - E - (D-B)(k_x^2 + k_{y,i}^2) \\ A(k_x - ik_{y,i}) \end{pmatrix}$$

and an energy-momentum relation given by

$$k_{y,i}(k_x) = (\delta_{1i} + \delta_{2i} - \delta_{3i} - \delta_{4i})\sqrt{-k_x^2 - F + (\delta_{1i} - \delta_{2i} + \delta_{3i} - \delta_{4i})K}$$

with

$$K = \sqrt{F^2 - \frac{M^2 - E^2}{B^2 - D^2}},$$
$$F = \frac{A^2 - 2(BM + DE)}{2(B^2 - D^2)}.$$

Therefore one gets

$$k_{y,1} = -k_{y,3}, \qquad k_{y,2} = -k_{y,4},$$
$$a_1 = a_3, \qquad a_2 = a_4,$$

and the general solution of Eq. (3.3) has the form $e^{ik_x x}\boldsymbol{\chi}_{\uparrow,E}(k_x, y)$ with

$$\boldsymbol{\chi}_{\uparrow,E}(k_x, y) = \sum_{i=1}^{4} c_i e^{iyk_{y,i}} \begin{pmatrix} a_i \\ b_i \end{pmatrix}. \tag{3.4}$$

The solution for the waveguide illustrated in Fig. 3.1(a) with a finite width W needs to satisfy the Dirichlet boundary conditions

$$|\boldsymbol{\chi}_{\uparrow,E}(k_x, y = \pm W/2)|^2 = 0. \tag{3.5}$$

Therefore the restriction of the coefficients c_i is given by

$$\underbrace{\begin{pmatrix} a_1 e^{ik_{y,1}W/2} & a_2 e^{ik_{y,2}W/2} & a_3 e^{ik_{y,3}W/2} & a_4 e^{ik_{y,4}W/2} \\ b_1 e^{ik_{y,1}W/2} & b_2 e^{ik_{y,2}W/2} & b_3 e^{ik_{y,3}W/2} & b_4 e^{ik_{y,4}W/2} \\ a_1 e^{-ik_{y,1}W/2} & a_2 e^{-ik_{y,2}W/2} & a_3 e^{-ik_{y,3}W/2} & a_4 e^{-ik_{y,4}W/2} \\ b_1 e^{-ik_{y,1}W/2} & b_2 e^{-ik_{y,2}W/2} & b_3 e^{-ik_{y,3}W/2} & b_4 e^{-ik_{y,4}W/2} \end{pmatrix}}_{=:\mathcal{M}} \begin{pmatrix} c_1 \\ c_2 \\ c_3 \\ c_4 \end{pmatrix} = \begin{pmatrix} 0 \\ 0 \\ 0 \\ 0 \end{pmatrix}, \tag{3.6}$$

and the non-trivial result of the kernel $\mathrm{Ker}\,(\mathcal{M}) = \{\boldsymbol{c} \in \mathbb{C}^4 | \mathcal{M}\boldsymbol{c} = 0\}$ fulfills $\det(\mathcal{M}) = 0$. By that, three of four coefficients c_i are determined and the fourth is taking care of the normalization condition

$$\int_{-W/2}^{W/2} dy\, |\boldsymbol{\chi}_{\uparrow,E,n}(y)|^2 = 1. \tag{3.7}$$

The transcendental equation $\det(\mathcal{M}(E, k_x)) = 0$ gives rise to the quantization condition of k_x for given energy E. The transversal function $\boldsymbol{\chi}_{\uparrow,E,n}(y)$ describing different modes n in the analogy of $\sin(\pi n y/W)$ for the 2DEG. Solving $\det(\mathcal{M}(E, k_x)) = 0$ or the secular equation in Ref. [94] numerically for $W = 500$ nm leads to the bandstructure illustrated in Fig. 3.1(b). The quantization of bulk modes and the linear Dirac dispersion in the band gap of $[-10, 10]$ meV is thereby visible. In contrast to the 2DEG, the transversal functions with fixed n are dependent on k_x (or E) and hence change with varying k_x, as we shortly discuss now.

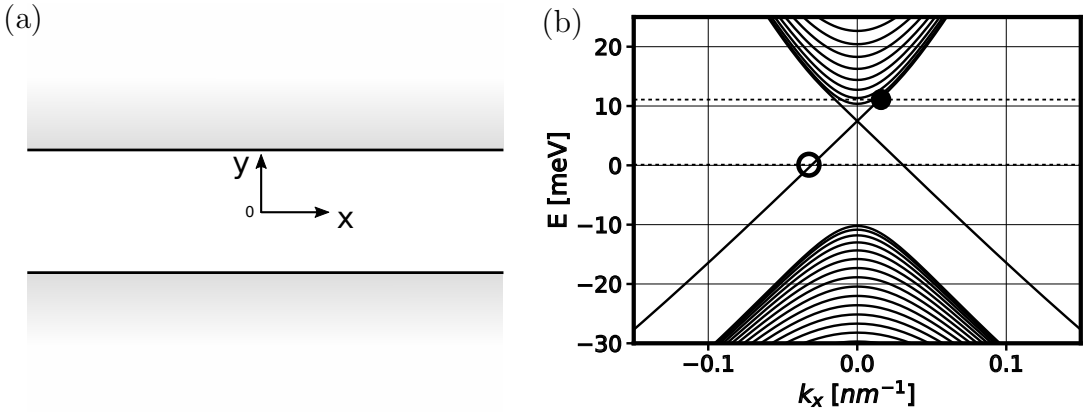

Figure 3.1: (a) The 2D waveguide setup with $W = 500$ nm and Dirichlet boundary conditions has a translational invariance in x-direction. Numerically solving the corresponding transcendental equation $\det(\mathcal{M}(E, k_x)) = 0$ with parameters used from Table 3.1 results in the bandstructure in (b). This setup induces a subband structure and a linear dispersion of the edge states in the bandgab $[-10, 10]$ meV. The two states marked as a circle (dot) are then plotted in Fig. 3.3(b) and (d).

Energy-dependent transversal modes

The eigenvectors of a hermitian matrix are orthogonal for distinct eigenvalues. It follows that the solutions $\boldsymbol{\chi}_{\uparrow,E,n}(y)$ for distinct energies E are orthogonal, too. For states intersecting with the dashed line in Fig. 3.2(a) we verified their orthogonality,

$$B'_{b,a} = \int_{-W/2}^{W/2} dy\, \boldsymbol{\chi}^{\dagger}_{\uparrow,E',a}(y)\, \boldsymbol{\chi}_{\uparrow,E,b}(y) \propto \delta(E' - E), \tag{3.8}$$

in Fig. 3.2(b). The probability density of the four transversal modes are plotted in Fig. 3.2(c). In contrast to the previous setups, the transversal modes in the TI are k_x-dependent and therefore not necessarily orthogonal in different modes at the same energy,

$$B_{b,a} = \int_{-W/2}^{W/2} dy\, \boldsymbol{\chi}^{\dagger}_{\uparrow,E,b}(y)\, \boldsymbol{\chi}_{\uparrow,E,a}(y) \neq \delta_{b,a}. \tag{3.9}$$

This is shown in Fig. 3.2(d) for two open and two evanescent modes (with $k_x \in i\mathbb{R}$). The probability density for these states is plotted in Fig. 3.2(e). This non-orthogonality makes a clear distinction with respect to the properties of Hamiltonians purely quadratic in momentum.

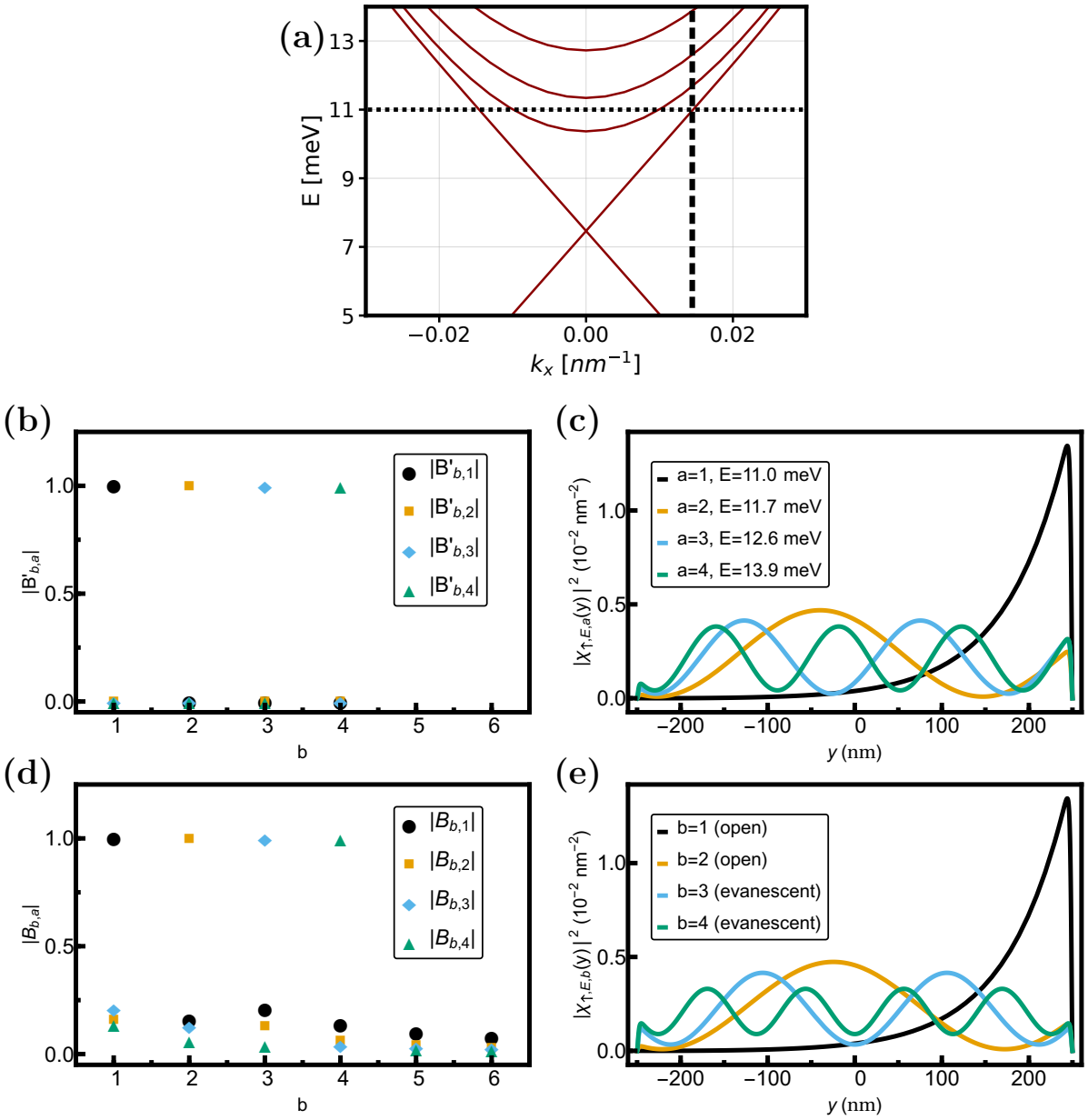

Figure 3.2: The TI transversal modes experience different properties than energy-independent modes of quadratic Hamiltonians. (a) In the bandstructure for width $W = 500$ nm, we concentrate on transversal modes at distinct (equal) energies, illustrated as dashed (dotted) lines. (b) For distinct energies the overlap $B'_{b,a}$ of transversal modes illustrated as intersections with the dashed line in (a) are orthogonal. The probability density of the four considered modes are plotted in (c). Due to the energy-dependency of $\boldsymbol{\chi}_{\uparrow,E,b}(y)$, the overlap $B_{b,a}$ in (d) is not delta-like. The probability density at constant energy (dotted line in (a)) is illustrated in (e). Thereby two modes are propagating ($k_x > 0$) and two evanescent (purely imaginary k_x).

Time-reversal symmetry and Kramers degeneracy

So far we only considered the solutions of Eq. (3.3), the spin $|\uparrow\rangle$ block. $\hat{H}_{\mathrm{BHZ}}$ is invariant with respect to the time-reversal symmetry operator $\mathcal{T}$ defined by

$$\mathcal{T} = i\sigma_y \otimes \mathbb{1}K = \begin{pmatrix} 0 & 0 & 1 & 0 \\ 0 & 0 & 0 & 1 \\ -1 & 0 & 0 & 0 \\ 0 & -1 & 0 & 0 \end{pmatrix} K, \tag{3.10}$$

with $\mathcal{T}^2 = -\mathbb{1}$, the Pauli matrix σ_y and complex conjugation operator K. This invariance, also holding for $\Delta \neq 0$ is expressed in the commutator relation $\mathcal{T}\hat{H}_{\mathrm{BHZ}}\boldsymbol{\psi} = \hat{H}_{\mathrm{BHZ}}\mathcal{T}\boldsymbol{\psi}$. The spin $|\uparrow\rangle$ solution in Eq. (3.4) can now be extended into the four-dimensional space of electron and hole bands,

$$\boldsymbol{\psi}_{\uparrow,E,n}(y) = \sum_{i=1}^{4} c_i e^{iy\,k_{y,i}} \begin{pmatrix} a_i(k_x) \\ b_i(k_x) \\ 0 \\ 0 \end{pmatrix}, \tag{3.11}$$

and give rise to the spin $|\downarrow\rangle$ solution by[1]

$$\boldsymbol{\psi}_{\downarrow,E,n}(y) = \mathcal{T}\boldsymbol{\psi}_{\uparrow,E,n}(y). \tag{3.12}$$

In Fig. 3.3 these solutions for the edge states are plotted for an energy in the bandgab and for $E = 11$ meV. These energies correspond to the blue and black dots in Fig. 3.1(b) with positive group velocity. Thereby the penetration depth into the bulk is rising for both spin states when increasing the energy. Our analysis is thereby in agreement to Ref. [95], wherein the edge states for energies in the bandgab are analytically solved.
By analyzing the implications of the underlying symmetry, further properties can be discovered. For a Hamiltonian with time-reversal symmetry $\mathcal{T}^2 = -1$, Kramers theorem gives an important inside: The spectrum is doubly degenerate, and the two states (Kramers pairs), here $\boldsymbol{\psi}_{\downarrow,E,n}(y)$ and $\boldsymbol{\psi}_{\uparrow,E,n}(y)$ are linked by time-reversal symmetry [96]. The overlap between this Kramers pair is vanishing and furthermore the forbidden backscattering between them is appearing: As long as time-reversal symmetry is preserved, any Hamiltonian $\hat{H}_{\mathrm{scatt}}$ with $\mathcal{T}\hat{H}_{\mathrm{scatt}} = \hat{H}_{\mathrm{scatt}}\mathcal{T}$ is not able to produce backscattering between the Kramers pair [95, 97]. This can be deduced by

$$\begin{aligned} \langle\boldsymbol{\psi}_{\downarrow}|\hat{H}_{\mathrm{scatt}}\mathcal{T}\boldsymbol{\psi}_{\downarrow}\rangle &= \langle\mathcal{T}\hat{H}_{\mathrm{scatt}}\mathcal{T}\boldsymbol{\psi}_{\downarrow}|\boldsymbol{\psi}_{\downarrow}\rangle = \langle\hat{H}_{\mathrm{scatt}}\mathcal{T}^2\boldsymbol{\psi}_{\downarrow}|\mathcal{T}\boldsymbol{\psi}_{\downarrow}\rangle \\ &= -\langle\boldsymbol{\psi}_{\downarrow}|\hat{H}_{\mathrm{scatt}}\mathcal{T}\boldsymbol{\psi}_{\downarrow}\rangle = -\langle\boldsymbol{\psi}_{\downarrow}|\hat{H}_{\mathrm{scatt}}\boldsymbol{\psi}_{\uparrow}\rangle = 0, \end{aligned} \tag{3.13}$$

whereby using the anti-unitary property of $\mathcal{T}$ [17]

$$\langle\boldsymbol{\psi}_{\downarrow}|\boldsymbol{\psi}_{\uparrow}\rangle = \langle\mathcal{T}\boldsymbol{\psi}_{\uparrow}|\mathcal{T}\boldsymbol{\psi}_{\downarrow}\rangle,$$

[1] Be aware that the equation $\boldsymbol{\chi}_{\downarrow}(k_x, y) = -i\sigma_y K\boldsymbol{\chi}_{\uparrow}(k_x, y)$ in Ref. [94] is misleading.

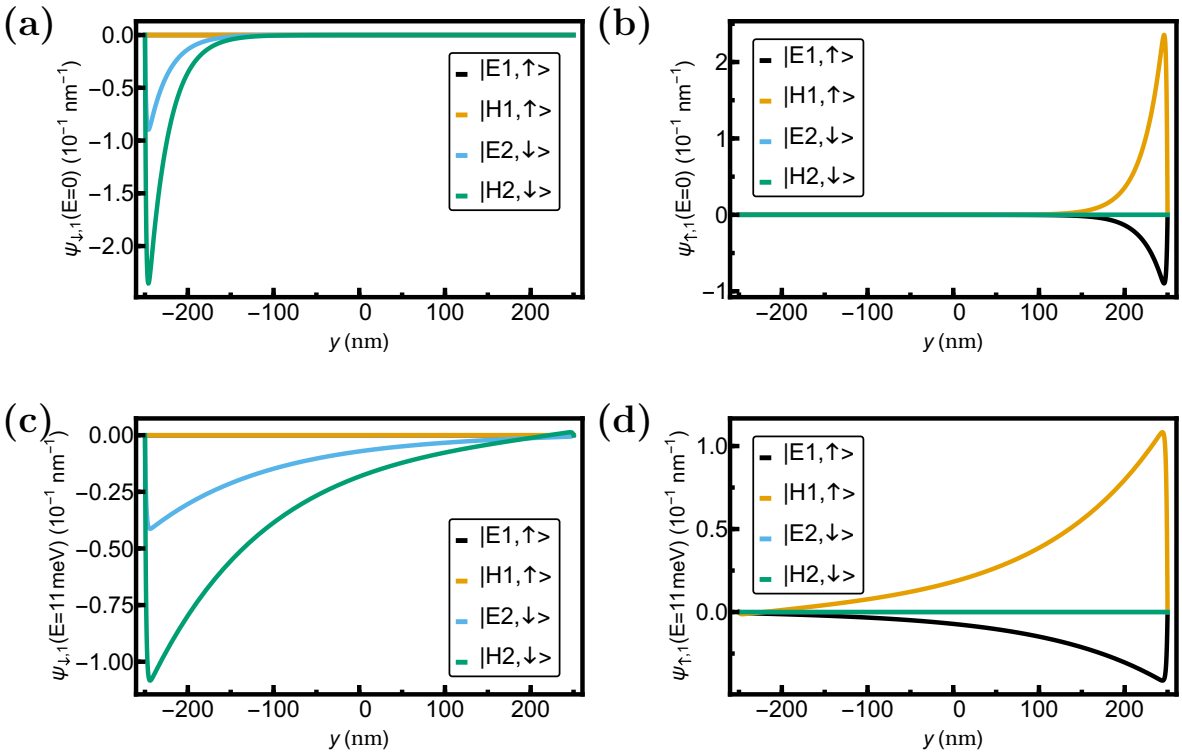

Figure 3.3: The analytically computed wave functions in Eqs. (3.11) and (3.12) at $E = 0$ meV and positive group velocity (circle in Fig. 3.1(b)) are pure edge states living on opposite edges. Here, the spin $|\downarrow\rangle$ (a) and spin $|\uparrow\rangle$ (b) states are illustrated. The penetration depth of the edge states $\psi_\downarrow$ (c) and $\psi_\uparrow$ (d) into the bulk is drastically increased for energies above the band gab, e.g. $E = 11$ meV (dot in Fig. 3.1(b)).

and the short notation $\boldsymbol{\psi}_\uparrow = \boldsymbol{\psi}_{\uparrow,E,n}$ ($\boldsymbol{\psi}_\downarrow = \boldsymbol{\psi}_{\downarrow,E,n}$). Another property originating from preserved time-reversal symmetry is the spin-momentum locking. The effect of $\mathcal{T}$ on a state of momentum $\boldsymbol{k}$ and spin $|\uparrow\rangle$ is

$$\mathcal{T}|\boldsymbol{k},\uparrow\rangle = |-\boldsymbol{k},\downarrow\rangle.$$

The spin of a state, propagating in one direction is perpendicular to the Kramers partner which is moving in the opposite direction. This so-called helical spin texture is responsible for the spin-momentum locking, wherein the spin is always coupled to a propagating direction [95].

Phase relation

Now, knowing the transversal modes described by Eq. (3.11), we are able to investigate the phase relation of transversal modes. The extended S-matrix $\tilde{S}$ is the solution of a system of linear equations originating from wave matching conditions of scattering states. The matrix of interest, S-matrix S is a submatrix of this extended S-matrix $\tilde{S}$, which takes not only open modes into account, but also evanescent ones. In general

it is crucial to compute first the extended S-matrix and then to extract the S-matrix S [98–103]. However, changing the phase of an evanescent transversal mode is only influencing $\tilde{S}$ elements depending on this particular mode. For this reason it is sufficient to only intervene in the open transversal modes of Kwant. As pointed out in sec. 2.3.2, the applied phase correction for Hamiltonians quadratic in momentum is accurate as long as transversal modes at different energies are not connected by physical relevant phases. Therefore, we will concentrate now on open transversal modes with the focus on changes in phases.

In Fig. 3.4 the phases $\phi(\dots)$ of $\boldsymbol{\psi}_{\uparrow,E,n}(y)$ are computed. Panel (a) and (b) illustrate the phases separated in electron and hole band contributions of the edge state $n = 1$ for seven energies. Both figures illustrate that no continuous change in phases are appearing. Solely when rising the energy to $E = 13$ meV, an abrupt shift is visible in (a) and (b). Considering the first bulk mode, $n = 2$ the electron and hole contributions are plotted in (c) and (d). Thereby no changes of phases are visible. To conclude, no continuous phase changes are present, when considering only energies in the bandgab ($|E| \leq 10$ meV) as we will assume in the TI leads later, not even abrupt changes are observable. It can therefore be followed, that the phase correction applied for the 2DEG in sec. 2.3.2 and 2.3.3 is utilizable also for TI leads.

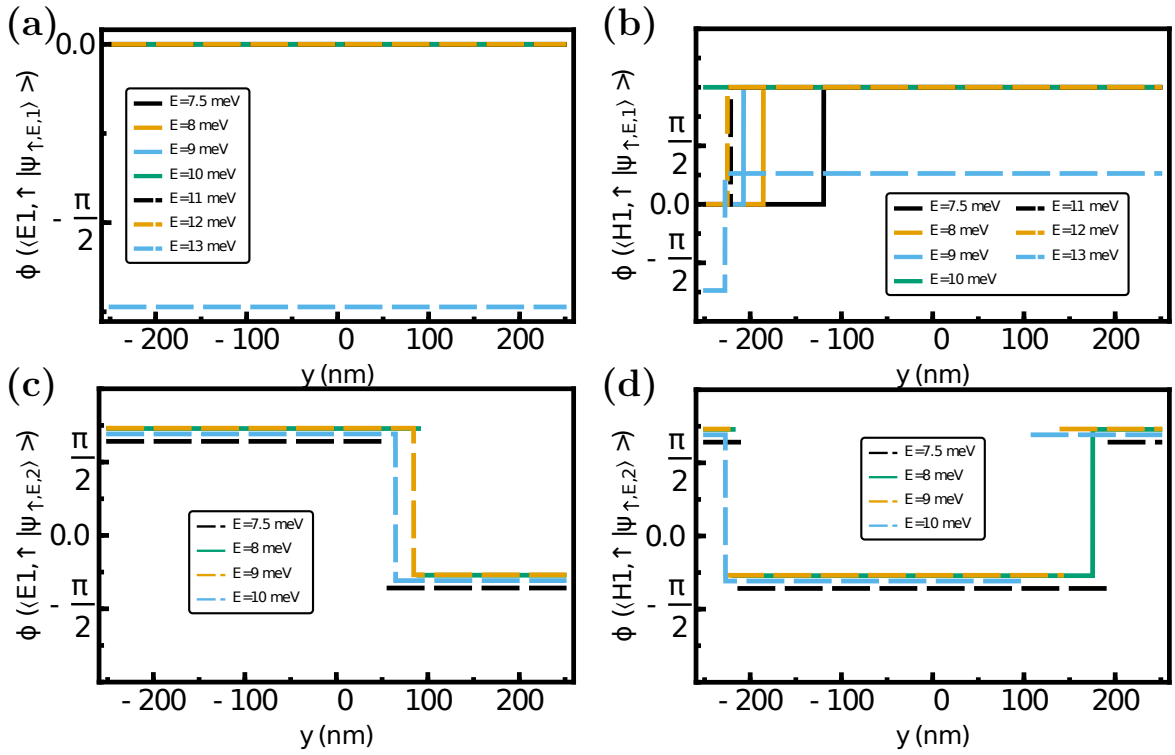

Figure 3.4: The phases ϕ of transversal modes $\boldsymbol{\psi}_{\uparrow,E,n}$ are studied for $n \in \{1, 2\}$ and varying energy. Panel (a) and (b) illustrate the phase of edge states ($n = 1$) whereby a separation in electron (a) and hole distributions (b) are made. For the first bulk mode in the conduction band ($n = 2$) in (c) and (d) the phases are plotted, too. Neither for edge states nor the first bulk mode continuous phase changes appear.

3.2. Current-current correlation

The formalism discussed in Ref. [23] (and revisited in sec. 2.1) is practicable for theoretical considerations and originates from investigations for photon detection [1], however an experimental realization to measure this observable is challenging in the present context of electron quantum optics (EQO). The inclusion of the Fermi sea is reasonable and an orientation towards time-dependent current measurements, too. In the framework of EQO, Ref. [87] established an electron coherence formalism for one-dimensional edge states. It was further developed and applied for quantum Hall edge states in quantum point contact (QPC) setups [91, 92, 104–106]. Here we will adapt this formalism to energy-dependent S-matrices and four open modes, $N = 4$ such that it is applicable for chaotic systems with one-dimensional edge states.

An incoming wavepacket in channel $i \in [1, 4]$ with a normalized waveform $\phi_i(E)$ is obtained by means of the creation operator $\hat{a}_i^\dagger$ by

$$|\phi_i\rangle = \int dE\ \phi_i(E)\, \hat{a}_i^\dagger(E)\, |F\rangle_\mu, \tag{3.14}$$

while the Fermi sea is given by $|F\rangle_\mu$ at the chemical potential μ and the creation and annihilation operators fulfill the anticommutation relations for fermions,

$$\{\hat{a}_i^\dagger(E), \hat{a}_j(E')\} = \delta_{ij}\, \delta(E - E'), \qquad \{\hat{a}_i^\dagger(E), \hat{a}_j^\dagger(E')\} = \{\hat{a}_i(E), \hat{a}_j(E')\} = 0. \tag{3.15}$$

The fermionic field operator $\hat{\Psi}_i(x, t)$ annihilates one electron at location x and time t,

$$\hat{\Psi}_i(x, t) = \frac{1}{\sqrt{h\, v}} \int d\epsilon\ e^{i\frac{\epsilon}{\hbar}(\frac{x}{v} - t)}\, \hat{a}_i(\epsilon), \tag{3.16}$$

with v being the constant velocity of the edge state. In the following we neglect the Coulomb interaction as also done in sec. 2.1. The current is given by

$$\hat{I}_i(x, t) = -ev\hat{\Psi}_i^\dagger(x, t)\hat{\Psi}_i(x, t) \tag{3.17}$$

and the first order electron (hole) coherence functions read [105]

$$G_i^e(t, t') = \langle\phi_i|\hat{\Psi}_i^\dagger(0, t')\hat{\Psi}_i(0, t)|\phi_i\rangle = \langle\hat{\Psi}_i^\dagger(0, t')\hat{\Psi}_i(0, t)\rangle, \tag{3.18}$$

$$G_i^h(t, t') = \langle\hat{\Psi}_i(0, t')\hat{\Psi}_i^\dagger(0, t)\rangle. \tag{3.19}$$

To proceed we fix the setup parameters for our purposes: The direct connection between location x and time t enables us to evaluate all operators at $x = 0$. With $N = 4$ open in- and outgoing channels and incoming wavepackets in $i = 1, 2$, we can write the annihilation operators as

$$\begin{pmatrix} \hat{a}_{\tilde{1}}(E) \\ \hat{a}_{\tilde{2}}(E) \\ \hat{a}_{\tilde{3}}(E) \\ \hat{a}_{\tilde{4}}(E) \end{pmatrix} = \begin{pmatrix} S_{1,1}(E) & S_{1,2}(E) & S_{1,3}(E) & S_{1,4}(E) \\ S_{2,1}(E) & S_{2,2}(E) & S_{2,3}(E) & S_{2,4}(E) \\ S_{3,1}(E) & S_{3,2}(E) & S_{3,3}(E) & S_{3,4}(E) \\ S_{4,1}(E) & S_{4,2}(E) & S_{4,3}(E) & S_{4,4}(E) \end{pmatrix} \begin{pmatrix} \hat{a}_1(E) \\ \hat{a}_2(E) \\ \hat{a}_3(E) \\ \hat{a}_4(E) \end{pmatrix} \tag{3.20}$$

with $\hat{a}_{\tilde{i}}$ ($i \in [1,4]$) representing operators in the outgoing channel $\tilde{i}$. The fermionic field operator in the outgoing channel $\tilde{3}$ can then be rewritten in terms of the annihilation operators in the incoming channels:

$$\hat{\Psi}_{\tilde{3}}(t) = \frac{1}{\sqrt{h\,v}} \int d\epsilon\; e^{-i\frac{\epsilon t}{\hbar}} \sum_{i=1}^{4} S_{3,i}(\epsilon)\hat{a}_i(\epsilon). \tag{3.21}$$

With Eq. (3.17) the current operator in the outgoing channel follows

$$\begin{aligned} \hat{I}_{\tilde{3}}(t) &= -ev\,\hat{\Psi}^{\dagger}_{\tilde{3}}(x=0,t)\hat{\Psi}_{\tilde{3}}(x=0,t) \\ &= -ev \sum_{i,j=1}^{4} \hat{\Psi}^{\dagger}_{\tilde{3},i}(t)\hat{\Psi}_{\tilde{3},j}(t), \end{aligned} \tag{3.22}$$

where

$$\hat{\Psi}_{\tilde{3},i}(t) = \frac{1}{\sqrt{h\,v}} \int d\epsilon\; e^{-i\frac{\epsilon t}{\hbar}}\, S_{3,i}(\epsilon)\hat{a}_i(\epsilon). \tag{3.23}$$

Taking into account $\delta\hat{I} = \hat{I} - \langle\hat{I}\rangle$ the current-current correlation reads

$$\sigma_{i,j}(t,t') = \langle\delta\hat{I}_i(t)\delta\hat{I}_j(t')\rangle = \langle\hat{I}_i(t)\hat{I}_j(t')\rangle - \langle\hat{I}_i(t)\rangle\,\langle\hat{I}_j(t')\rangle. \tag{3.24}$$

When inserting Eq. (3.22) into Eq. (3.24) we obtain

$$\begin{aligned} \sigma_{\tilde{3},\tilde{4}}(t,t') &= e^2v^2 \sum_{i,j=1}^{4} \left\langle \delta\hat{\Psi}^{\dagger}_{\tilde{3},i}(t)\,\delta\hat{\Psi}_{\tilde{4},j}(t') \right\rangle, \\ &\quad + e^2v^2 Q(t,t') \end{aligned} \tag{3.25}$$

$$Q(t,t') = \sum_{\substack{i,j=1 \\ j\neq i}}^{4} \left\langle \hat{\Psi}^{\dagger}_{\tilde{3},i}(t)\,\hat{\Psi}_{\tilde{3},j}(t)\hat{\Psi}^{\dagger}_{\tilde{4},j}(t')\,\hat{\Psi}_{\tilde{4},i}(t') \right\rangle, \tag{3.26}$$

whereby some summands in $Q(t,t')$ vanished (computed in app. B.1.1). In $Q(t,t')$ not only coherences due to the wavepacket interference contribute, but also Fermi sea effects. In app. B.1.2 we separate these contributions. They can be split into contributions of Hanbury-Brown-Twist (HBT) type and into one Hong-Ou-Mandel (HOM) type, schematically depicted in Fig. 3.5 in analogue to Ref. [92, p. 150]:

$$\Delta Q(t,t') = \Delta Q_{\mathrm{HBT},1}(t,t') + \Delta Q_{\mathrm{HBT},2}(t,t') + \Delta Q_{\mathrm{HOM}}(t,t'). \tag{3.27}$$

In app. B.1.3 we compute the averaged quantity

$$\Delta\bar{Q}_{\mathrm{HOM}} = \frac{2}{T_M} \int_{-\infty}^{\infty} d\tau \int_{0}^{T_M} d\bar{t}\,\Delta Q_{\mathrm{HOM}}(\bar{t}+\tau, \bar{t}-\tau) \tag{3.28}$$

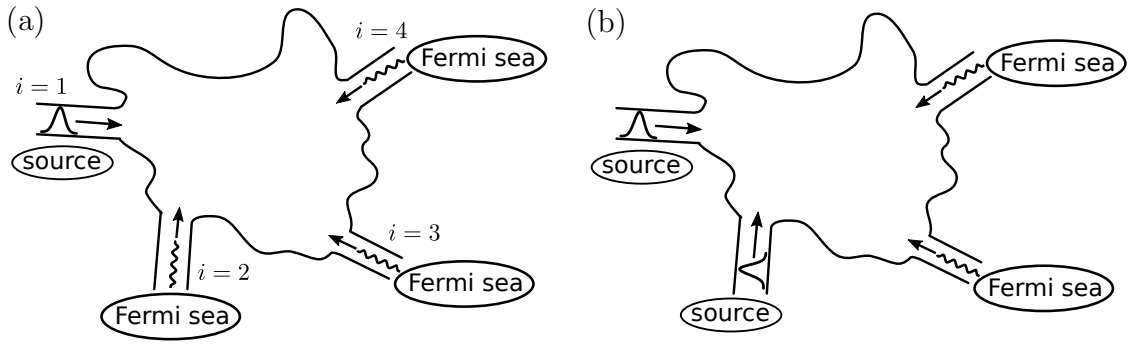

Figure 3.5: Panel (a) illustrates the Hanbury-Brown-Twist (HBT) geometry, in which the incoming wavepacket only interferes with the Fermi sea. (b) In the HOM geometry two incoming wavepackets are entering the setup, whereby two-particle correlations of both sources and Fermi sea contributions are present. A separation of these yields Eq. (3.27).

with the time duration of the measurement given by T_M explicitly. Here we concentrate on the result given by

$$\Delta\bar{Q}_{\mathrm{HOM}} = -\frac{16\pi^2}{T_M}\ \mathrm{Re}\Big[\int dEdE'\,\phi_1(E)\phi_2(E')\phi_1^*(E')\phi_2^*(E)\cdot S_{3,1}^*(E)S_{4,1}(E')S_{4,2}^*(E')S_{3,2}(E)\Big]. \tag{3.29}$$

With averaging over an ensemble (e.g. disorder) we recognize the D^x correlator:

$$\Delta\bar{Q}_{\mathrm{HOM}} = -\frac{16\pi^2}{T_M}\,\mathrm{Re}\Big[\int dEdE'\,\phi_1(E)\phi_2(E')\phi_1^*(E')\phi_2^*(E)\cdot\ D^x\left(\frac{E-E'}{2}\right)\Big]. \tag{3.30}$$

This equation is the final goal of linking the current-current correlation to the four-point correlations investigated in chap. 1. In comparison to Eq. (2.13), only marginal differences appear. Therefore the behavior of exponential tails when increasing the dwell time to wavepacket width τ_D/τ_s is expected, too. In sec. 3.3.3 we will address this in more detail.

3.3. Implementation of TI setups with universal correlations

The phase correction of TI edge states in the Kwant code established in sec. 3.1 paves the way to transfer the achievements of trivial TI states in sec. 2.3 now to S-matrix correlations in TIs. First we will focus on the S-matrix correlators and whereby start with one spin block of the BHZ Hamiltonian. Afterwards we introduce spin-orbit coupling in sec. 3.3.2. Finally, in sec. 3.3.3 the impact of these correlators on the current-current correlation will be established.

3.3.1. Concentrating on one spin subblock

To start with, we focus on a subblock of the BHZ Hamiltonian, namely the Hamiltonian $\hat{h}_{2\times2}(\hat{\boldsymbol{k}}) = \hat{h}_{TI}(\hat{\boldsymbol{k}})$ from Eq. (3.2), living in one spin-subspace $|E1,\uparrow\rangle$ and $|H1,\uparrow\rangle$. It is implemented for the four leads (with gate voltage $C = 0$), sketched red in Fig. 3.6(a) and the cavity (blue) obeys the 2DEG Hamiltonian

$$\hat{h}_m = \frac{\hbar^2}{2m^*}\hat{\boldsymbol{k}}^2 \begin{pmatrix} 1 & 0 \\ 0 & -1 \end{pmatrix} + V_g \begin{pmatrix} 1 & 0 \\ 0 & 1 \end{pmatrix} \tag{3.31}$$

with $V_g = -47$ meV and $\frac{\hbar^2}{2m^*} = -(B + D) = 1198$ meVnm^2 adapted to the effective mass of the $|E1,\uparrow\rangle$ TI-band. The time-reversal symmetry with respect to $\mathcal{T}$,

$$\mathcal{T} = i\sigma_y K = \begin{pmatrix} 0 & 1 \\ -1 & 0 \end{pmatrix} K$$

is thereby fulfilled for $\hat{h}_m$ and violated by $\hat{h}_{TI}$. It is important to note that this does not imply the S-matrix to obey the statistic of CUE. The interface lead-cavity with two different Hamiltonians generates additional non-chaotic scattering. Here we will only observe the statistical result and later focus on the explanation. Instead of using the complex formalism in Ref. [76] to compare the S-matrix elements, we generate 10^6 matrices of size $N \times N$ within the A symmetry class (representing the CUE ensemble class [21, 22]) using Kwant [72, 107, 108]. The distribution of absolute values of the S-matrix in Figs. 3.6 (b)-(c) plotted in blue shows promising consistency comparing with the RMT distribution of CUE (orange) and therefore indicates chaos in the cavity. As illustrated in Figs. 3.6(d)-(e), the uniform distribution of the angles is governed by RMT and numerics.

In the next step we produce the two- and four-point correlators of interest. The vanishing imaginary part of $D^x(\Delta)$ and $C^=(\Delta)$ is a property which was explained in Eq. (2.45) in sec. 2.2.5 and applies also here. The correlators are illustrated in Fig. 3.7 (black dots) with mean level density $d = \hbar^2/(m^*\mathcal{A})$ for a cavity of area $\mathcal{A}$. No semiclassical prediction for these setups are available, such that we compare the data to the semiclassical predictions (blue) of 1D Hamiltonians quadratic in momentum in the CUE class established in sec. 2.2.5. The known C_2 correlator from Ref. [60] in

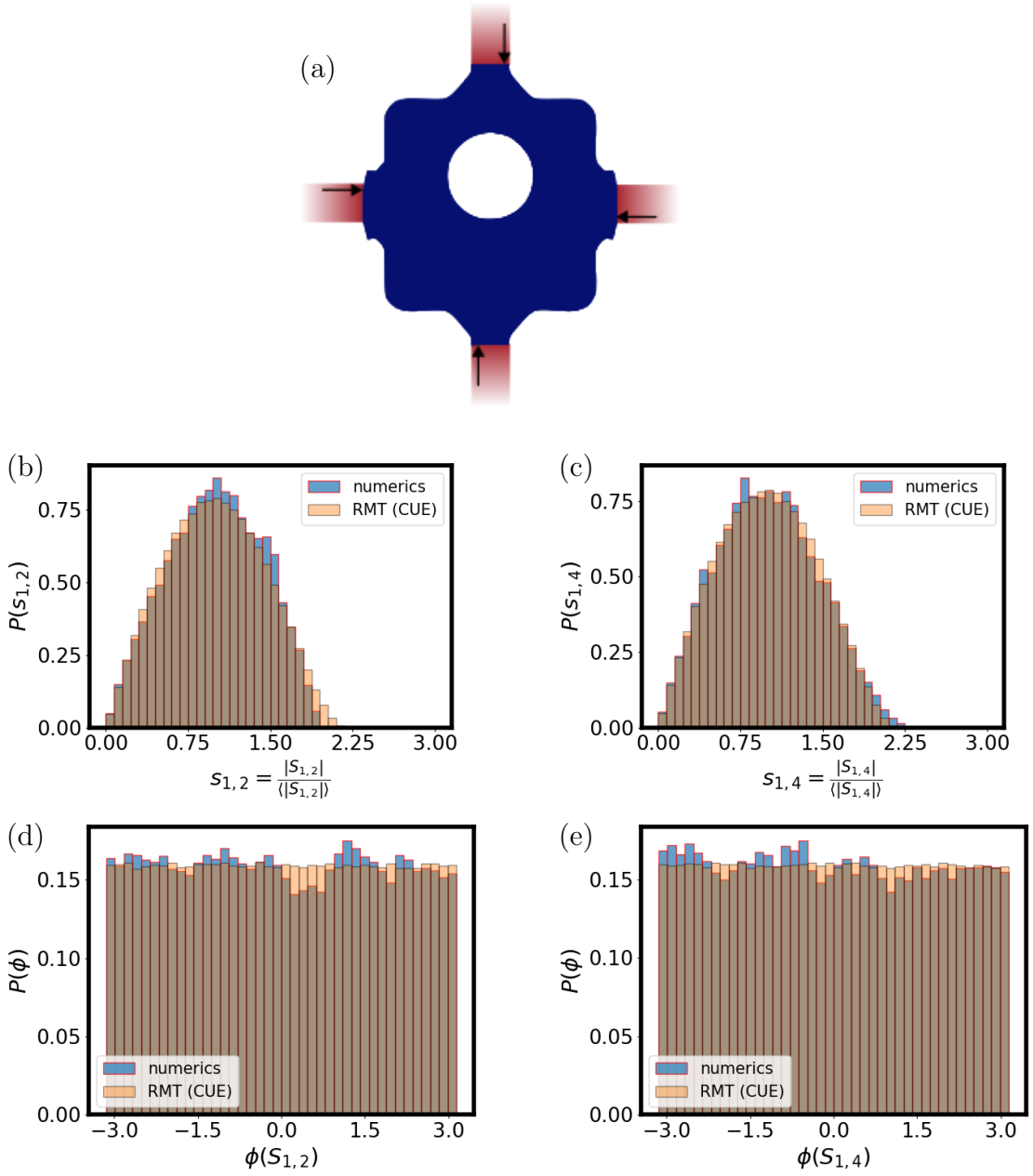

Figure 3.6: (a) The system, consisting of four TI leads (red) and one metallic cavity (blue) has $N = 4$ number of edge modes (black arrows). The statistics of $|S_{b,a}|$ (blue) in (b) and (c) illustrate consistency to RMT statistics in the CUE class of 10^6 matrices of size 4×4 (orange) [72, 107, 108]. The uniform distributions of angles $\phi(S_{b,a})$ in (d) and (e) are in agreement to RMT, too.

Eq. (2.37) and the results of the four-point correlators in Eqs. (2.52)-(2.54) are used. The dwell time is estimated in the following way: The number of open modes is set to $N = 4$ and the width of the leads are adapted to the effective penetration depth of the TI edge states in the leads. Due to our preliminary work in sec. 2.2.5 and sec. 2.3.3 we are aware of the fact that the S-matrix correlators are applicable for low number of open modes N. Therefore a dwell time in units of the passing time $\tau_{\text{pass}} = L/v_g$ is expected to be $\tau_{D,m}/\tau_{\text{pass}} \approx 11$. The comparison of the different correlators gives then an important information, shown in Fig. 3.7: Even when the effective lead widths and number of open modes are adjusted to correlator formulas (plotted blue), the correlators for the system with TI leads (in black) are notably different to the correlators for metallic leads by narrower widths. This corresponds to strongly increased dwell times when replacing a metallic lead by the TI lead. A rough estimation of the dwell time for the TI setup can be achieved when fitting $C_2(\Delta)$ with $N = 4$ to the data. We gain the adapted form (plotted in red) in Fig. 3.7(a), (b) with the dwell time given by $\tau_D/\tau_{\text{pass}} = 80 - 93$. The ratio of this dwell time and the dwell time expected for metallic leads is thus $\tau_D/\tau_{D,m} \approx 7 - 8.5$, demonstrating the significant increased survival probability in the cavity when TI leads are attached. This derivation is of course only valid, if the fundamental C_2 form in case of TI leads can be approximated by Eq. (2.37). The correlator shapes with TI leads do not differ from previously studied ones. However, the peaks around energy difference $\Delta = 0$ are strongly pronounced for the real parts of C_2, $B^=$ and D^x and mark the distinction between the two setups besides dwell time differences.

To proceed, we compute two-point and four-point correlators of a slightly deformed setup: In comparison to Fig. 3.6(a) we extend the waveguides (with $\hat{h}_m$) before connecting them to the TI leads as illustrated in the inset of Fig. 3.8(a). The comparison of the S-matrix correlators indicate that usually no difference between setups with long or short leads are noticeable. Here, we illustrate the alignment of $B^=(\Delta)$ in Fig. 3.8(a), (b) and of $D^x(\Delta)$ in Fig. 3.8(d) explicitly. The misalignment of $C^=(\Delta)$ in Fig. 3.8(c) originates from the unconverged correlator for short leads, that experiences drastic oscillations even for big energy differences Δ. We can conclude that the coupling of the TI edge states to the waveguide states (with about 17 open modes) in the metallic regime is as good as to the cavity itself. The transmission from the metallic waveguide to the TI lead is $1\,\frac{e^2}{h}$ and the reflection $17\,\frac{e^2}{h}$.
With this information we can draw an important conclusion: The substantial difference in the number of open modes is forcing an increase of the dwell time. An incoming electron from the TI lead enters the metallic waveguide and proceeds into the cavity. The reduced probability to leave the system due to the mode mismatch in the TI and metallic waveguides is then leading to the enhanced dwell time and therefore the reduced widths in S-matrix correlators observable in Fig. 3.7. This points out an significant difference to the previous studied cavity in chap. 1. Replacing in this setting the TI leads by the same Hamiltonian as in the cavity leads to more open modes and a decreased dwell time. For $\tau_E \gg \tau_D$ ergodicity is lost and universal S-matrix correlators would vanish.
From Fig. 3.8 and analysis of S-matrix elements we can deduce further information. The overlap of evanescent modes between different leads is marginal, otherwise the waveguide extension would result at least in different magnitudes of the S-matrix correlators. Thus

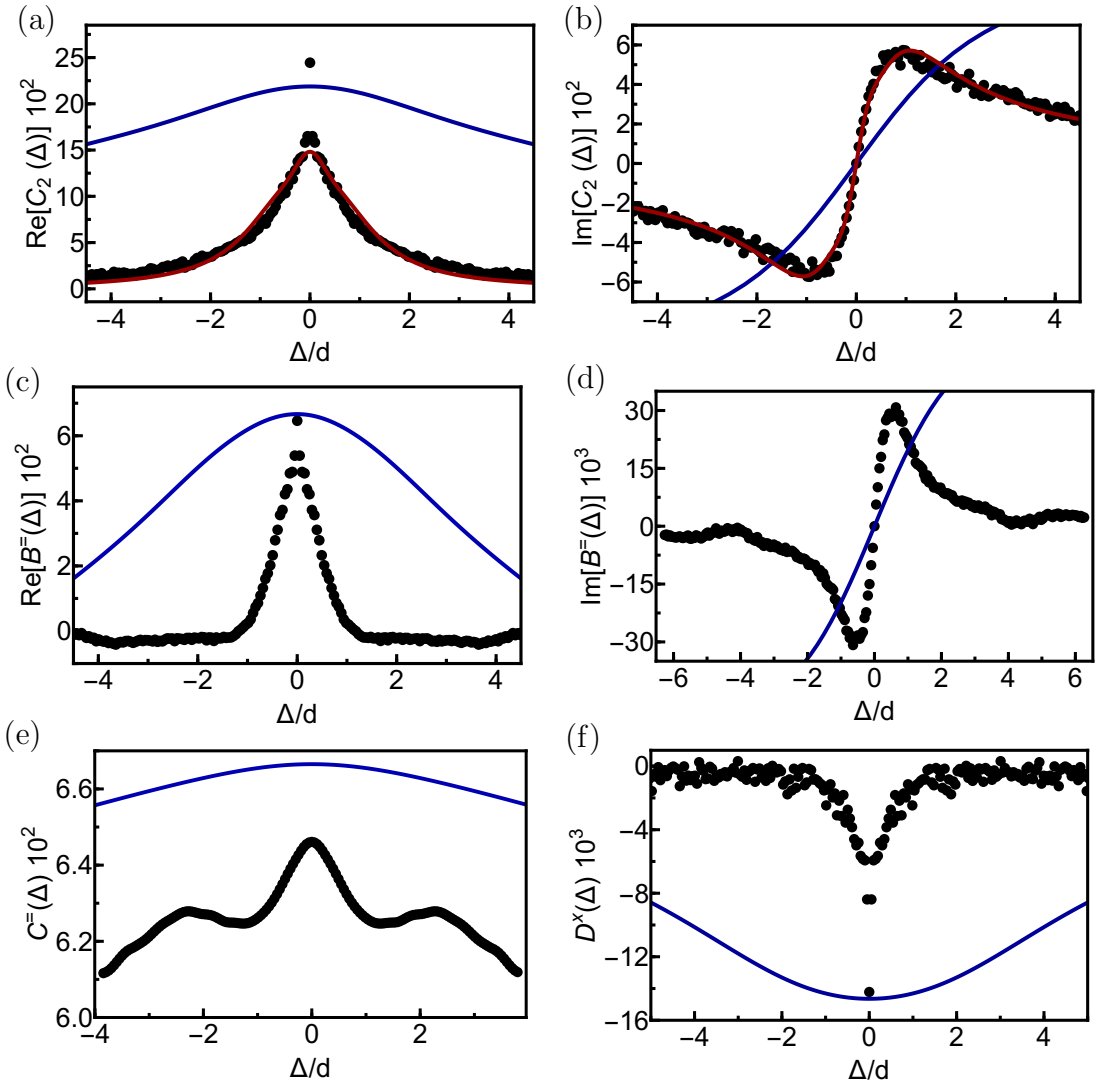

Figure 3.7: The system with TI leads illustrated in Fig. 3.6(a) has universal S-matrix correlators. The real part of $C_2(\Delta)$ a sharp peak around $\Delta = 0$ (black) in (a), whereby the imaginary part (black) has a more smooth form visible in (b). The semiclassical prediction for a setup with metallic leads, $N = 4$ and lead widths similar to the penetration depth of the TI edge state are plotted in blue. Adapting the dwell time in the semiclassical formula for $N = 4$ is plotted in red. The dwell time ratio of the red and blue function yields $\tau_D/\tau_{D,m} \approx 7 - 8.5$. For $B^=(\Delta)$ (black) in (c), (d), in which the real part contains also a strong gradient around $\Delta = 0$, the expectation for metallic leads (blue) are again corresponding to lower dwell times. In case of $C^=(\Delta)$ in (e) and $D^X(\Delta)$ in (f) the same holds. $D^x(\Delta)$ is again containing a strong gradient around $\Delta = 0$ and in addition more fluctuations than (a)-(e).

the S-matrix of the whole system S_t can be approximated by a composition of separate S-matrices, namely the S-matrix S_{wg} of the waveguide interface $\hat{h}_{TI}$, $\hat{h}_m$ and the S-matrix of the chaotic, metallic cavity S_c, such that multiple scattering is also taken into account [68]. The result describing one element of S_t consists of summands with different orders in S_c and several S_{wg} elements. In principle thereby the statistic of the S-matrix S_t can be approximated. The S-matrix statistics of S_t in Fig. 3.6 and the correlators in Fig. 3.7 however indicate multiple scattering, such that concentration on only first order scattering events are not sufficient enough. Depending on the detailed amplitudes in S_{wg}, the S-matrix S_t can obey the statistical properties of CUE, however it is not valid in general[2].
When considering two-point S-matrix correlators approximated by means of this composition, averaging over mean energy $\bar{E}$ is building a compound of the form $\langle S_{wg,ba}(\bar{E}+\Delta)S_{c,dc}(\bar{E}+\Delta)S^*_{wg,fe}(\bar{E}-\Delta)S^*_{c,hg}(\bar{E}-\Delta)\rangle$. Although the S-matrices S_{wg} are not significantly energy-dependent inside an energy range in which the number of open modes is constant, in the whole energy range relevant changes in S_{wg} appear. This prohibits a separation into products of the form $\langle S_{wg,ba}(\bar{E}+\Delta)S^*_{wg,fe}(\bar{E}-\Delta)\rangle$ and $\langle S_{c,dc}(\bar{E}+\Delta)S^*_{c,hg}(\bar{E}-\Delta)\rangle$. The elements of S_c obey the RMT statistics of COE and for $(h,g)=(d,c)$ the correlator will have the form of S-matrix correlators investigated in chap. 2. The separation would provide us with the benefit of partially known dependencies, however several higher orders of S-matrix correlators with different permutations of channels are appearing, too.

[2] A pure addition or multiplication of two elements of different matrices (each in the CUE) is not resulting in an CUE statistic.

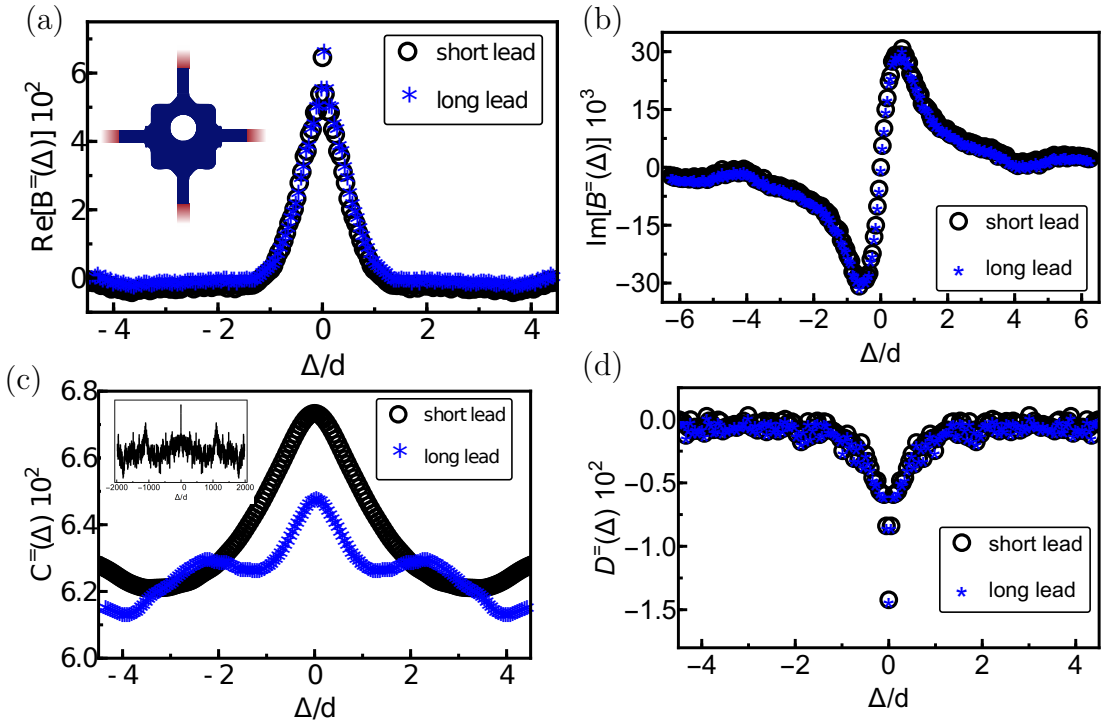

Figure 3.8: A metallic waveguide between TI leads and the metallic cavity is added. The inset of (a) is illustrating that. The difference of the appearing $B^{=}(\Delta)$ in comparison to the system of Fig. 3.6(a) is thereby marginal. However, for $C^{=}(\Delta)$ panel (c) illustrates a significant difference. The offdiagonal correlator $D^{x}(\Delta)$ in (d) is again coinciding for both system forms.

Replacing the 2DEG Hamiltonian $\hat{h}_m$ by $\hat{h}_{TI}$ with a gate voltage of $C = -47$ meV in the cavity, the entire system is violating time-reversal symmetry. The correlators (black) have similar forms in Fig. 3.9, whereby for comparison reasons we replot the results from Fig. 3.8 now in blue. The reflection and transmissions between a TI lead with $C = 0$ (with one open mode) and a lead with $C = -47$ meV (around 17 open modes) are equivalent to the previous studied waveguide with $\hat{h}_m$. Therefore, the decreased widths are not originating from increased mode mismatches but most likely from changed forms due to violating time-reversal symmetry and/or the usage of $\hat{h}_{TI}$ in the cavity. This is supported by the following observation: $D^x(\Delta)$ shows a very strong agreement for a metallic cavity with the correlator of a TI cavity. In contrast to this the other correlators are different for the two types of Hamiltonians in the cavity. The mode mismatch would lead to equivalent behaving for all correlators and is therefore not responsible for this effect.

Furthermore we compare the chaotic setup consisting purely of $\hat{h}_{TI}$ with RMT predictions of the CUE class in Fig. 3.10 [72, 107, 108]. Thereby we exclude the illustration of uniform distributed phases of the S-matrix and concentrate on the absolute values. As illustrated in Fig. 3.10(a)-(d), the agreement between both methods is convincing for all S-matrix elements.

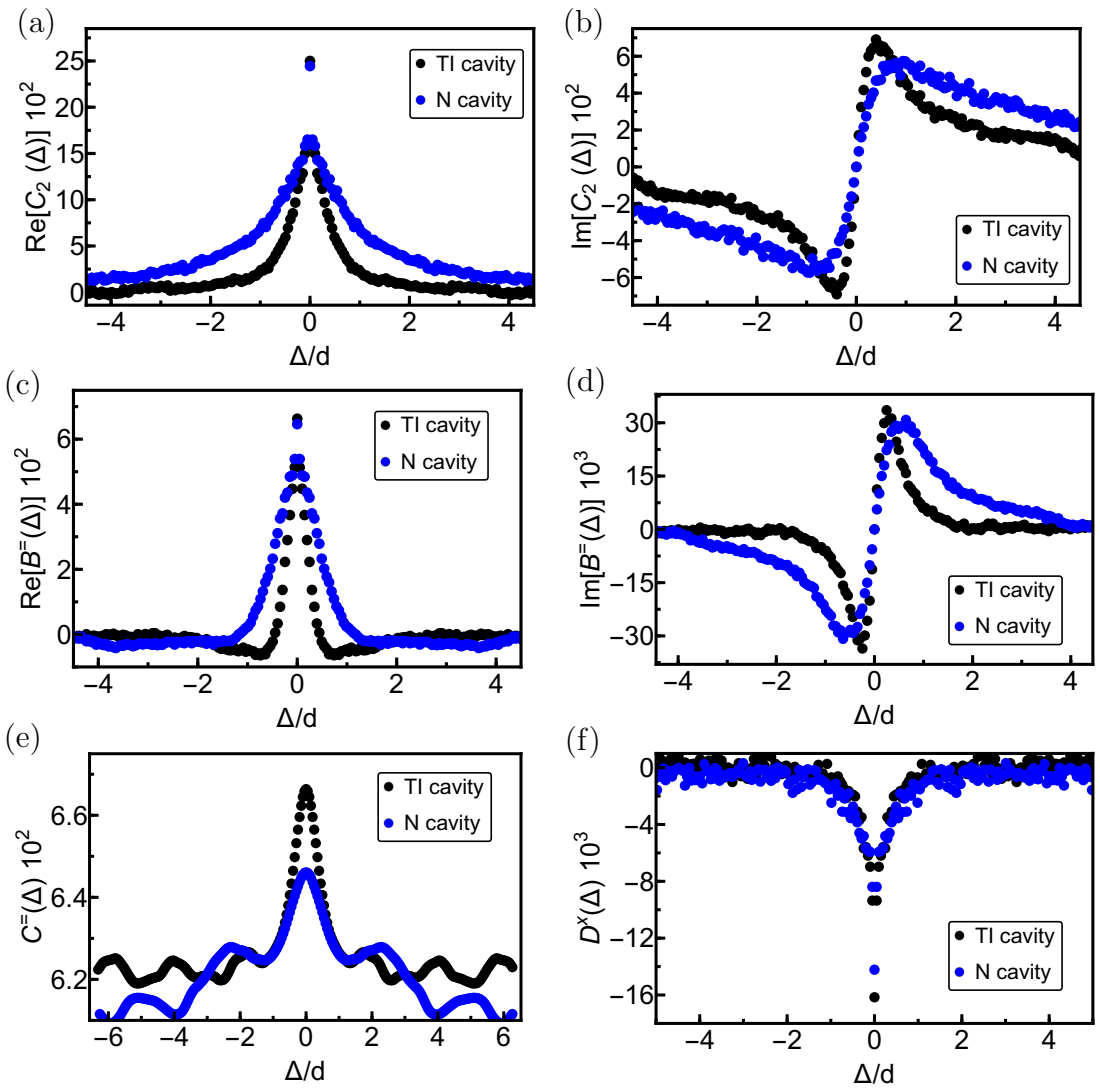

Figure 3.9: Replacing the Hamiltonian in the cavity from $\hat{h}_m$ to $\hat{h}_{TI}$ is affecting the two and four-point correlators slightly. In blue the correlators of a pure metallic cavity are shown (reprinted from Fig. 3.8), while the data plotted in black represents the pure TI based cavity. It is noticeable that $D^x(\Delta)$ is the least affected by this change.

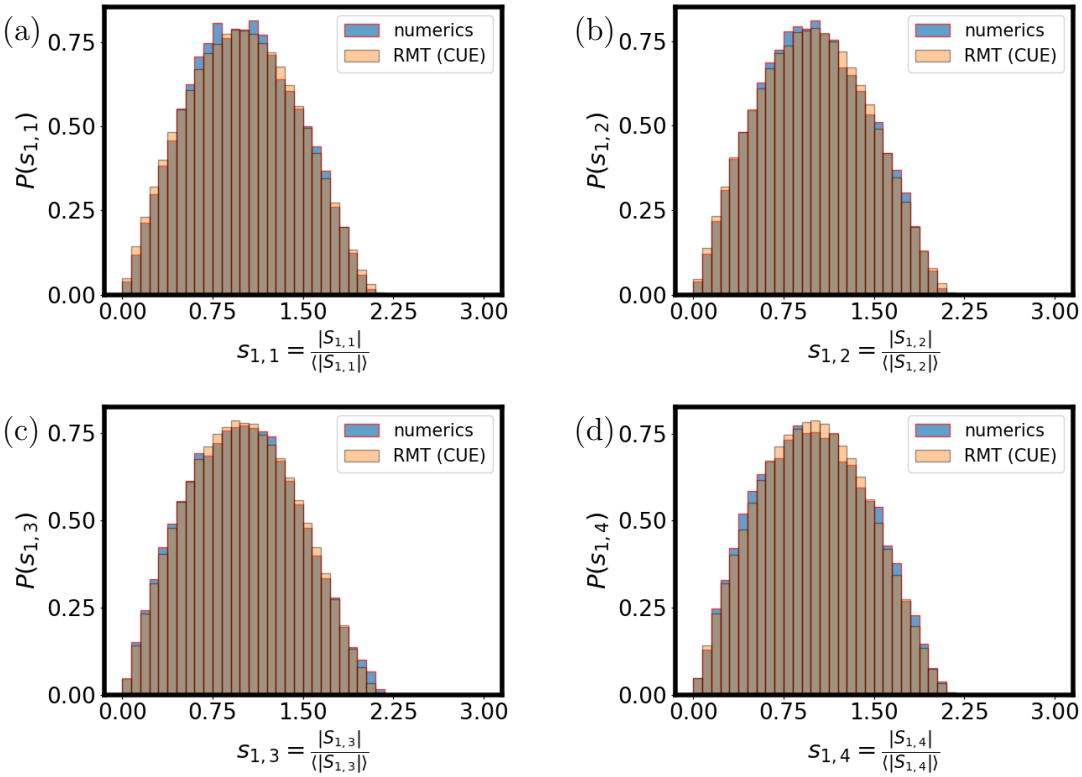

Figure 3.10: A chaotic cavity represented purely by $\hat{h}_{TI}$ produces S-matrix statistics in agreement with RMT of the CUE, whereby the absolute values are illustrated and the uniform distribution of phases are not depicted.

The experimental realization of setups depicted in the inset of Fig. 3.8 are challenging. More convenient is a setup with leads as broad as the scattering area itself. For this purpose we tune the broadness of the leads from $W_{\text{lead}}/W_{\text{sys}} = 15\%$ (Fig. 3.8) to 80% with an intermediate step of 50%. In the four lead setup with a width of 100%, the direct paths between two neighboring leads are dominating such that ergodicity is lost. In Fig. 3.11 the two-point correlator and the four-point correlators experience changes when the leads are broadened. In black we replot the data from Fig. 3.10, such that we can compare the three setups directly. An overall characteristic for all correlators is not visible, which is why we will discuss the differences for each correlator separately. The real part of $C_2(\Delta)$ experiences an reduced width for leads with increased broadness in the same way as the real part of $B^{=}(\Delta)$. The amplitudes at $\Delta = 0$ are almost equivalent for the three setups. For correlators obeying the semiclassical estimations received in chap. 2 this corresponds to an increased dwell time for a lead broadness of 80% in comparison to the setup with $W_{\text{lead}}/W_{\text{sys}} = 50\%$ and 15%. The data in Figs. 3.11(b) and (d) however is not explicit enough to fortify this conclusion. The widths are reduced when the leads are broadened but the amplitudes are simultaneously decreased. An adaption of the amplitudes indicate no significant difference in the widths. The $C^{=}(\Delta)$ experience different amplitudes but equivalent widths, too. The width of $D^{x}(\Delta)$ is certainly reduced for the setups $W_{\text{lead}}/W_{\text{sys}} = 50\%$ and 80%, while the amplitude at $\Delta = 0$ is almost stable under broadness changes. The data in Fig. 3.11 is not explicit enough to interpret changes in the dwell time. However tuning the lead broadness results in significant differences in the correlators, although the leads still consist of only open edge states with the same penetration depth.

Furthermore, the statistic of S-matrix absolute values changes when the ratio of widths is increased from 50% to 80%. As visible in Fig. 3.12 the agreement with RMT statistics of the CUE is partly lost. The misalignment to CUE is marginal for $|s_{1,i}|$ with $i \in \{1, 2, 3\}$, while indeed $|s_{1,4}|$ experiences an significant difference. The lead width is already broad enough to generate direct paths between neighboring lead modes, such that the statistic is modified. The statistic of $|s_{1,3}|$ (connecting mode 3 of the second neighboring lead to mode 1) is unchanged because the in- and outgoing modes are more separated, as illustrated in Fig. 3.11(d). This argument is fortified by the analogue statistic of $|s_{4,1}|$ in comparison to $|s_{1,4}|$.

3.3.2. Introducing spin-orbit coupling

The spin degree of freedom was not yet implemented, but certainly gives further interesting phenomena to investigate. We introduce this degree of freedom by the full 2D BHZ-Hamiltonian [90],

$$\hat{H}_{\text{BHZ}} = \begin{pmatrix} \hat{h}_{TI}(\hat{\boldsymbol{k}}) & \begin{matrix} 0 & -\Delta \\ \Delta & 0 \end{matrix} \\ \begin{matrix} 0 & \Delta \\ -\Delta & 0 \end{matrix} & \hat{h}^{*}_{TI}(-\hat{\boldsymbol{k}}) \end{pmatrix}, \tag{3.32}$$

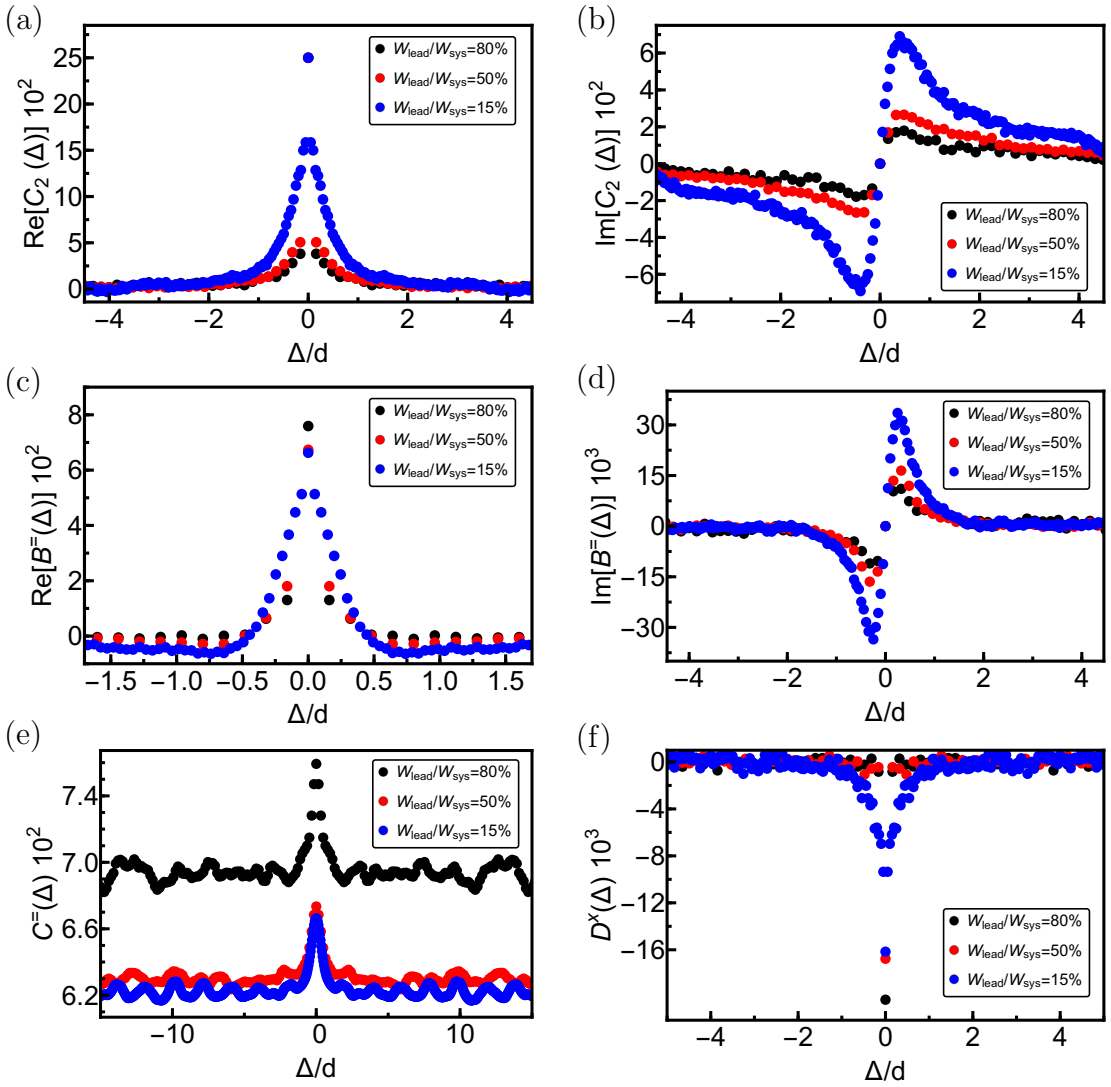

Figure 3.11: Increasing the width ratio $W_{\text{lead}}/W_{\text{sys}}$ step wise from 15%, 50% to 80% changes the form of the relevant correlators. An overall agreement to higher dwell times (corresponding to decreased widths) for $W_{\text{lead}}/W_{\text{sys}} = 80\%$ is only visible for $\text{Re}[C_2(\Delta)]$, $\text{Re}[B^{=}(\Delta)]$ and $D^{x}(\Delta)$. It is not fortified by the other correlators.

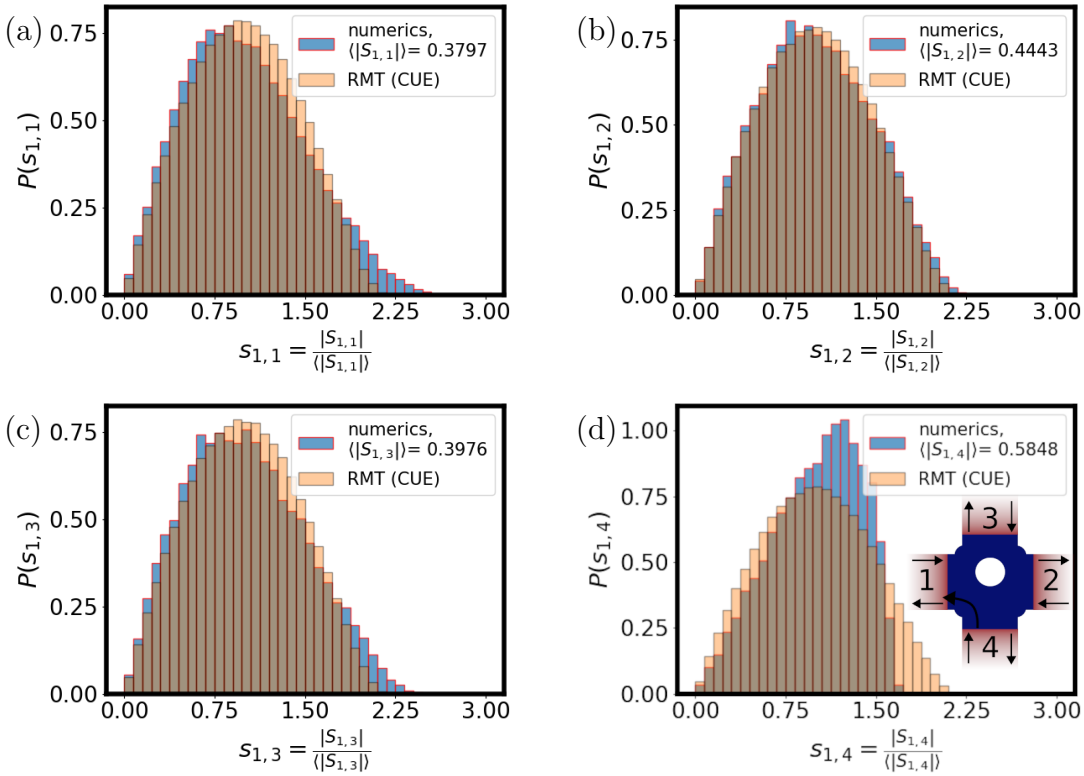

Figure 3.12: In contrast to the $W_{\text{lead}}/W_{\text{sys}} = 50\%$ or 15% setups the statistic of $|S_{b,a}|$ for the setup with $W_{\text{lead}}/W_{\text{sys}} = 80\%$ is not given by CUE. (a)-(c) illustrate marginal misalignments to RMT, however the statistics in panel (d) are significantly different. Rising probabilities of direct paths between the modes 1 and 4 of two neighboring leads are the explanation of this characteristic, illustrated in the inset of (d).

that follows from Eq. (3.1) in the basis of the electron and hole bands $|E1,\uparrow>, |H1,\uparrow>$, $|E1,\downarrow>$ and $|H1,\downarrow>$. The default Dresselhaus spin-orbit coupling strength is set to 1.6 meV in the cavity and zero in the leads [90]. For a waveguide and an energy in the band gab, $E \in [-10, 10]$ meV two incoming edge states with opposite spin are arising, as illustrated in Fig. 3.3. Thereby the two edge states are propagating at opposite edges of the waveguide into (out of) the central system. The extra spin degree of freedom enables us to reduce the number of leads from four to two and still remain with four open modes. The BHZ-Hamiltonian only fulfills time-reversal symmetry with $\mathcal{T}^2 = -1$, such that AII is the tenfold classification of the Hamitlonian and the S-matrix obeys $S^T = -S$ [21, 109]. The corresponding RMT ensemble is called circular symplectic ensemble (CSE).

In Fig. 3.13 the statistics of the setup with two leads are illustrated. The system shape is again given by Fig. 3.6 (a) with $W_{\text{lead}}/W_{\text{sys}} = 15\%$, however only two leads on opposite sides are present. As pointed out in sec. 3.1 for H_{BHZ} forbidden backscattering is present. In panel (a), a small discrepancy of the numerical data ($S_{ii} = 0$) is shown. The averaged value of $\langle |S_{11}| \rangle = 10^{-4}$ differs due to a necessary adjustment: The time-reversed partner states are energetically degenerate, such that Kwant chooses any arbitrary superposition of these states as the incoming and outgoing modes and the symmetry class of the S-matrix , $S^T = -S$ is not visible anymore. Therefore we introduce a small shift κ of the spin up Hamiltonian block in comparison to the spin down such that the chosen basis is given by time-reversed partner states:

$$\hat{H}_{\text{BHZ}} \to \hat{H}_{\text{BHZ}} + \kappa \begin{pmatrix} 1 & 0 & 0 & 0 \\ 0 & 1 & 0 & 0 \\ 0 & 0 & -1 & 0 \\ 0 & 0 & 0 & -1 \end{pmatrix}. \tag{3.33}$$

This slightly broken time-reversal symmetry is then responsible for the non-vanishing back reflection $S_{ii} \neq 0$. Statistics of the off-diagonal elements $|S_{i,j}|$ in Fig. 3.13 (b)-(d) are neither coinciding with the CSE ensemble nor with CUE, however phases are mostly equally distributed again. When increasing the spin-orbit coupling by a factor of two, no significant changes in the S-matrices are observable, such that the dwell time is expected to be high enough to provide spin mixing.

Regarding the S-matrix correlators, Fig. 3.14 illustrates these for two lead widths, $W_{\text{lead}}/W_{\text{sys}} = 15\%$ and 80%. $\text{Re}[C_2(\Delta)]$ and $\text{Re}[B^{=}(\Delta)]$ in (a) and (c) of Fig. 3.14 show a width decrease when the lead width is increased. The other correlators are not showing this width decrease. The same mechanism appeared for one spin block, where $\text{Re}[C_2(\Delta)]$ and $\text{Re}[B^{=}(\Delta)]$ experience a width decrease (Fig. 3.11). It is conspicuous for the cavity with spin-orbit coupling that $\text{Re}[B^{=}(\Delta)]$ and $D^x(\Delta)$ experience a delta-like form, such that a determination of the precise shape is not possible even when reducing Δ/d drastically. This effect is happening already for a width ratio $W_{\text{lead}}/W_{\text{sys}}$ for which the setup of Fig. 3.11 still experiences at detectable shape for both correlators. From Fig. 3.11 (d) we know, that the amplitude of $\text{Im}[B^{=}(\Delta)]$ reduces for increasing lead widths. Now, in Fig. 3.14 (d) we find again the same mechanism but with higher intensity. Thus the amplitude is reduced to the level of noise, such that no clear signature

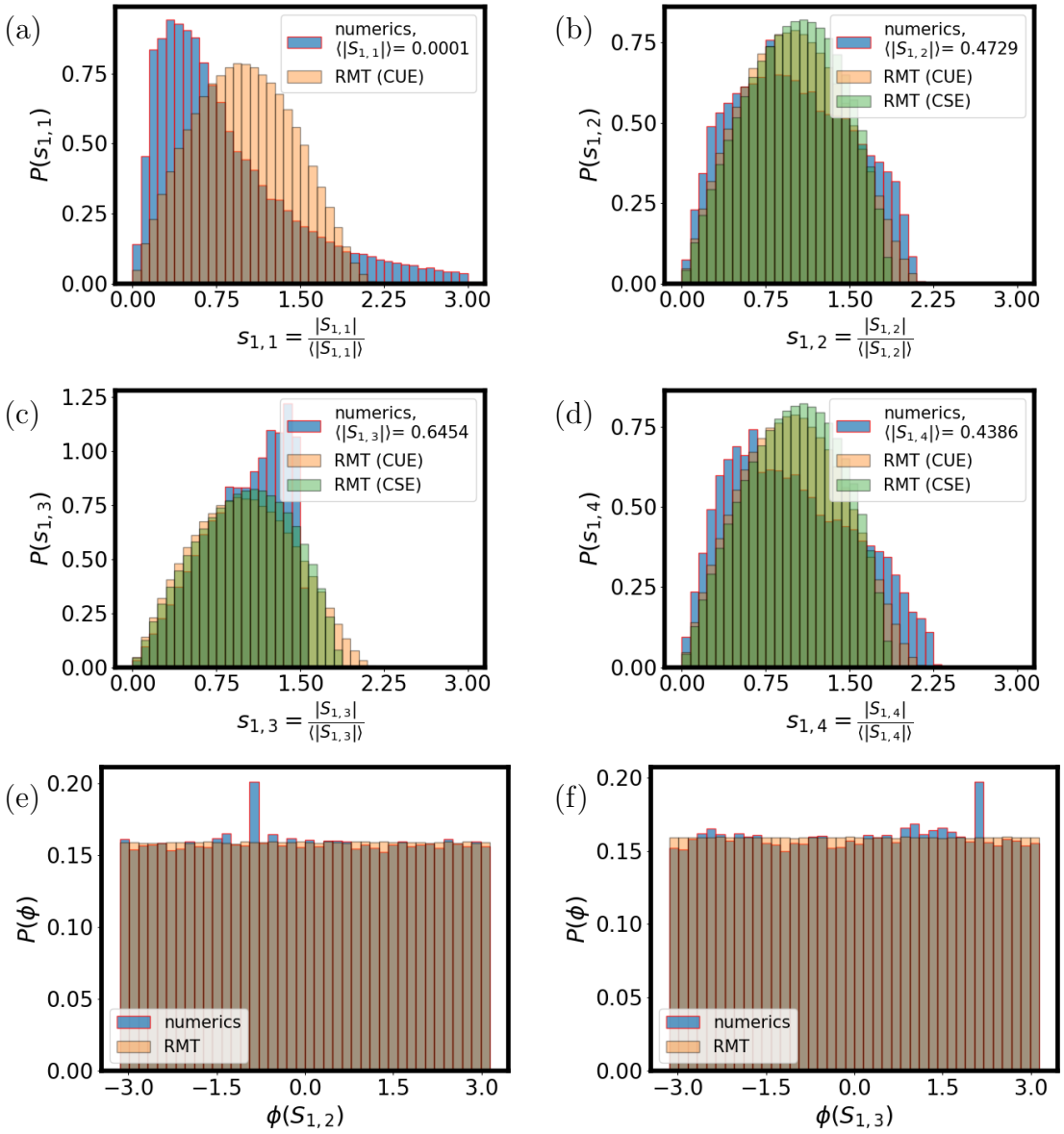

Figure 3.13: In case of the setup of Fig. 3.6 (a) but with only two leads on opposite sides, the extra spin degree of freedom generates four in-and outgoing modes. Absolute values of $S_{i,j}$ are just coinciding roughly with RMT statistics of the CSE. The non-vanishing back reflection, $S_{1,1} \neq 0$ results from numerical necessary adjustments. The other distributions share the characteristic of nearly equivalent averages $\langle |S_{i,j}| \rangle$, however significant difference to the CSE is noticeable. The statistic of phases are represented by illustrations (e) and (f). Both absolute values and phases are hints, that direct paths are perturbing the ergodicity.

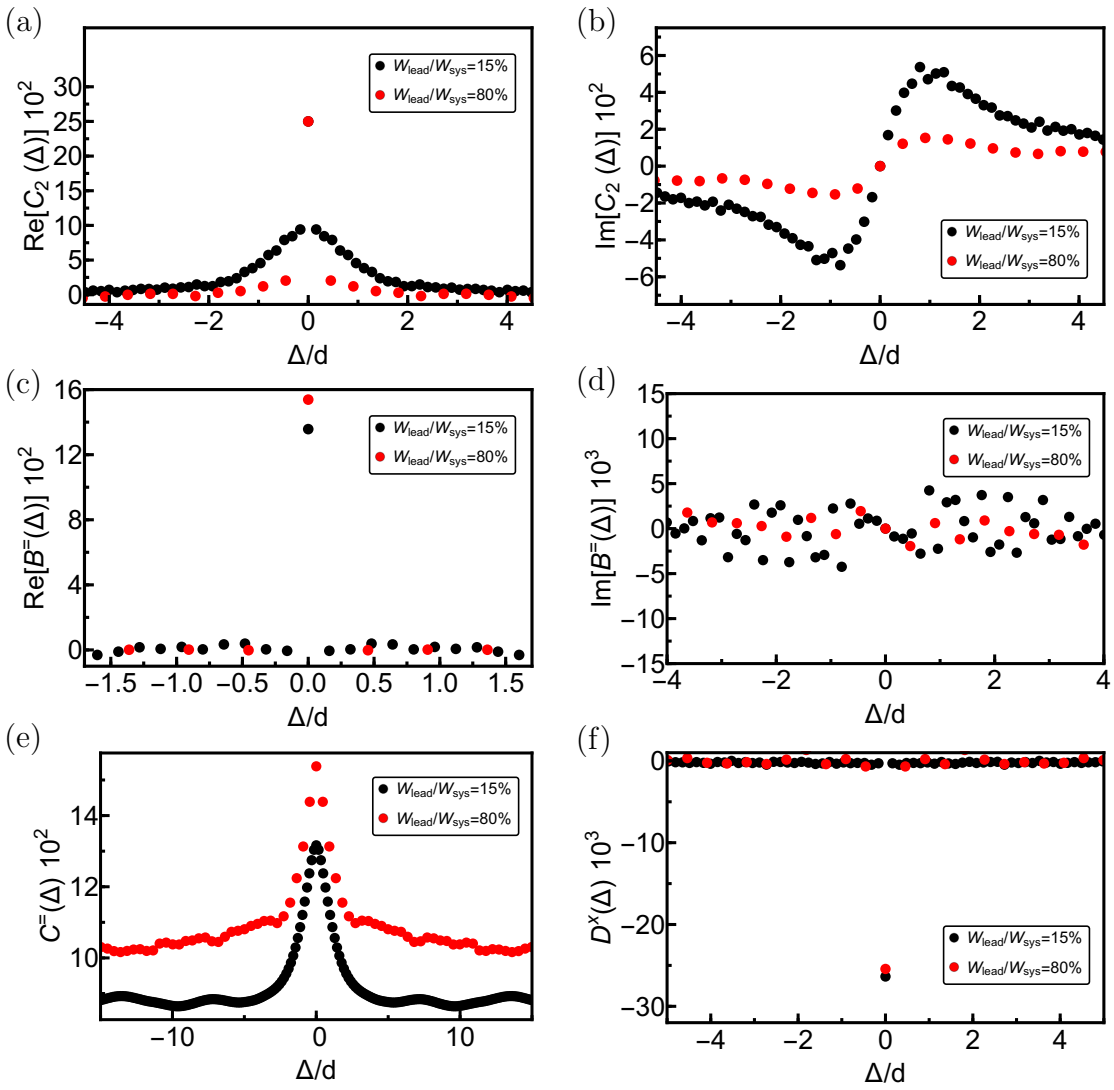

Figure 3.14: For a billiard-shaped setup with two leads, each hosting two edge states the lead width W_{lead} is varied. The delta-like shape of Re$[B^=(\Delta)]$ and $D^x(\Delta)$ for both lead widths is marking a significant difference to Fig. 3.11(c) and (f). Furthermore no clear shape of Im$[B^=(\Delta)]$ is visible. This can be caused by a reduced amplitude to noise ratio. The reduced amount of accessible outgoing modes due to forbidden backscattering can be a reason for the reduced widths of Re$[B^=(\Delta)]$ and $D^x(\Delta)$.

is visible. One possible explanation for the stronger width decrease in comparison to the four lead setup is based on the time-reversal symmetry: In the setup consisting of one spin block, the time-reversal symmetry is not fulfilled and therefore the backscattering is non-zero. Each incoming plane wave can exit the cavity in all outgoing modes. In contrast, with the application of both spin blocks, the time-reversal symmetry squares to -1 and backreflection is forbidden (or drastically reduced in the numerics). Each incoming mode has a reduced number of possible modes to exit, namely 3. This can be a reason for increase dwell times. Why only $\mathrm{Re}[B^{=}(\Delta)]$ and $D^x(\Delta)$ are experiencing this effect is one open question, here, more investigations in this direction are necessary to support this argument.

3.3.3. Implications for current-current correlations

In the previous section we were able to determine $D^x(\Delta)$ for several setup configurations in non-trivial TIs. To study the impact of this on the current-current correlation depicted in sec. 3.2, we repeat Eq. (3.30):

$$\Delta\bar{Q}_{\mathrm{HOM}} = -\frac{16\pi^2}{T_M} Re\left[\iint_{-\infty}^{\infty} dE dE'\, \phi_1(E)\phi_2(E')\phi_1^*(E')\phi_2^*(E)\; D^x\left(\frac{E-E'}{2}\right)\right].$$

The formalism introduced in sec. 3.2 is intended for four lead setups, whereby each lead hosts one edge state. When neglecting interactions between particles as done in the overall thesis, the adaption to setups with two leads and still four open modes is only influencing the HBT contributions and not $\Delta\bar{Q}_{\mathrm{HOM}}$. Assuming Gaussian wavepackets,

$$\begin{aligned}\phi_1(t) &= \frac{1}{\sqrt[4]{\pi}\sqrt{\tau_s}} e^{-\frac{(t-\tau)^2}{2\tau_s^2}},\\ \phi_2(t) &= \frac{1}{\sqrt[4]{\pi}\sqrt{\tau_s}} e^{-\frac{t^2}{2\tau_s^2}},\end{aligned} \tag{3.34}$$

whereby the time delay τ between both wavepackets is included in ϕ_1 and the width of both packets is given by τ_s. For an off-diagonal correlator given by

$$D^x(\Delta) = \frac{1}{4^3\left(1+\frac{4\Delta^2\tau_D^2}{\hbar^2}\right)}, \tag{3.35}$$

as expected for trivial TIs with $N = 4$ open modes, the resulting current-current correlation of HOM type is illustrated in Fig. 3.15. In the same manner as the probability in Eq. (2.13) experiences a transition from a Gaussian shape to a form with exponential tails when tuning the ratio τ_D/τ_s from 0.5 to 5. The $D^x(\Delta)$ correlator for non-trivial TIs shares this Lorentzian form in principle, however we observe an increased dwell time τ_D (corresponding to reduced widths), such that the ratio τ_D/τ_s is also increased and will therefore result in a more flat current-current correlation $\Delta\bar{Q}_{\mathrm{HOM}}$ as depicted in blue. For chaotic cavities with TI edge states as in-and outgoing waveguides, $\Delta\bar{Q}_{\mathrm{HOM}}$ shows an time delay τ independent form over a huge τ range. Therefore the signal to noise ratio is drastically reduced, however even at big time delays, $\tau \gg \tau_s$ an effect on $\Delta\bar{Q}_{\mathrm{HOM}}$ is visible.

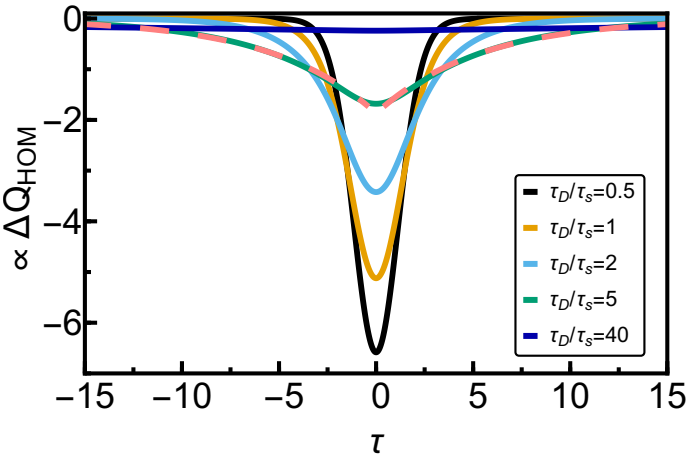

Figure 3.15: The current-current correlation of HOM-type $\Delta\bar{Q}_{\mathrm{HOM}}$ depends strongly on the ratio of dwell time and width of the incoming wavepacket τ_D/τ_s, in the same way as the probability studied in Eq. (2.13) of sec. 2.1 does [23]. For Gaussian wavepackets, the shape transforms from a Gaussian form to a form with exponential tails when tuning $\tau_D/\tau_s = 0.5 \to 5$, whereby an exponential fit (dashed pink line) is illustrating this. For non-trivial TIs the highly reduced width of $D^x(\Delta)$ is then influencing the ratio to even higher values, such that the shape is flattened as illustrated in blue.

3.4. Summary and outline

To numerically study universal S-matrix correlations of non-trivial TIs in Kwant a phase correction of the in-and outgoing lead modes is essential. Therefore we started with the analytical solution of the corresponding Schrödinger equation of an infinite waveguide lead. The solution achieved for edge and bulk modes of the BHZ Hamiltonian displays the expected Kramers degeneracy and forbidden backscattering due to time-reversal symme-try with $\mathcal{T}^2 = -1$. An abrupt phase change of edge modes when passing the threshold of the band gap is observed. However, no continuous phase changes are identified when considering energies in the band gab. This enables us to apply the same phase correction as investigated in chap. 1 for 2DEG setups.

The formalism of probabilities adapted to study the electronic HOM effect is rooted in previous investigations in optics, however for the electronic counterpart it is more convenient to use a formalism based on current operators. The applied formalism in the second quantization involves the Fermi sea and comprises an experimentally feasible observable. We extend this electron coherence formalism to energy-dependent S-matrices and four open modes. The resulting current-current correlation can be separated in Hanbury-Brown-Twist and Hong-Ou-Mandel type of correlations. The former consists of wavepacket-Fermi sea interference terms and the latter originates from interferences of two wavepackets, thus encoding indistinguishability correlation in the spirit of the optical HOM effect.

To proceed, we computed numerical S-matrix correlations for one spin block of the BHZ Hamiltonian using the tight-binding method. The system consists of four leads, each hosting one helical edge state, and a billiard-shaped cavity intersecting these leads. The correlators show similar forms as in case of a 2DEG model, however a reduced width is observable. A reduced width of the correlators is also partially accounted for by broadened leads. The alignment of the phase and absolute values of the S-matrix to the CUE ensemble is given for different setup configurations. When implementing the second spin block, the Dresselhaus spin-orbit coupling is also included. The arising two modes for each lead enable us to reduce the number of leads to two. The achieved S-matrix distribution of phase and absolute values are not in accordance to CSE, due to the scattering at the lead-cavity interfaces and direct paths disturbing this statistic. Only $D^x(\Delta)$ is contributing to the current-current correlation $\Delta\bar{Q}_{\mathrm{HOM}}$ and this correlator shows a delta-like form. As a consequence, $\Delta\bar{Q}_{\mathrm{HOM}}$ exhibits a form, almost independent on the time delay between the two wavepackets entering the chaotic cavity.

In the end, we want to give a short outlook on reasonable investigations in this context: The current-current correlation is experimentally accessible and extendable to temperature dependent phenomena or higher number of open modes. The proceeding to 2D in-and outgoing lead channels would give us the benefit of studying 2DEG setups or TI based setups with open bulk and edge modes. The most striking task is the theoretical development of S-matrix correlators for the numerical setups. For S-matrices in CSE, previous studies pave the way to study S-matrix correlators semiclassically [110–112]. However, the additional scattering occurring at the lead-cavity interfaces provides more complex phenomena. This also applies to the energy-dependent S-matrix correlators in the Heisenberg approach.

4. The quantum corral

4.1. Electron confinement a copper surface

To investigate the different perspectives and questions of the quantum corral we start in sec. 4.2 with the description of the default experimental situation, including the STM and AFM properties of major importance. Afterwards we introduce a simple model, the hard wall model, and solve it analytically in subsec. 4.3.2. The agreement between this model and the STM measurements from 1993 as well as the experimental results of Prof. Giessibls group is known [36,44,51]. A more detailed description can be made when using multiple scattering formalism and adjusting the scattering phase of an individual iron atom based on STM data. This adjustment becomes essential for understanding the level broadening mechanism or the LDOS for more complex corral forms [113–115]. Instead of changing the quantum corral form, adding an extra adatom into the corral is increasing the complexity. In sec. 4.4 we learn that also in case of extra adatoms, the inclusion of the scattering phases is relevant. Implementing this allows for correct predictions for all adatom positions tested in the quantum corral, but instead of an analytical approach we applied a tight-binding simulation [72]. Furthermore we will show that the symmetry of the Cu (111) bulk is directly influencing the first radial maxima of the LDOS around Fermi energy. The original quantum corral creates resonant states with a wave length of $\lambda_F = 3$ nm on a diameter of 14 nm, it seems reasonable to consider these mesoscopic states as orbitals of an artificial atom. Starting from that, Ref. [47] studied bonding between two corrals of multiple shapes made up by CO molecules instead of Fe atoms. In contrast to that, we will investigate the force characteristic of the mesoscopic wave function to the tip orbital in subsec. 4.5.1 using a quasi-classical ansatz for the Coulomb interaction. The fast decay of the force measured in experiments is conflicting with the theoretically achieved slow decaying Coulomb force [51]. The hypothesis of a chemical bonding between the artificial atom eigenstate and the tip orbital is therefore a more convincing approach, although this model needs a more in-depth analysis. The results of this analysis as presented here follows mainly our manuscript [51][1].

[1]

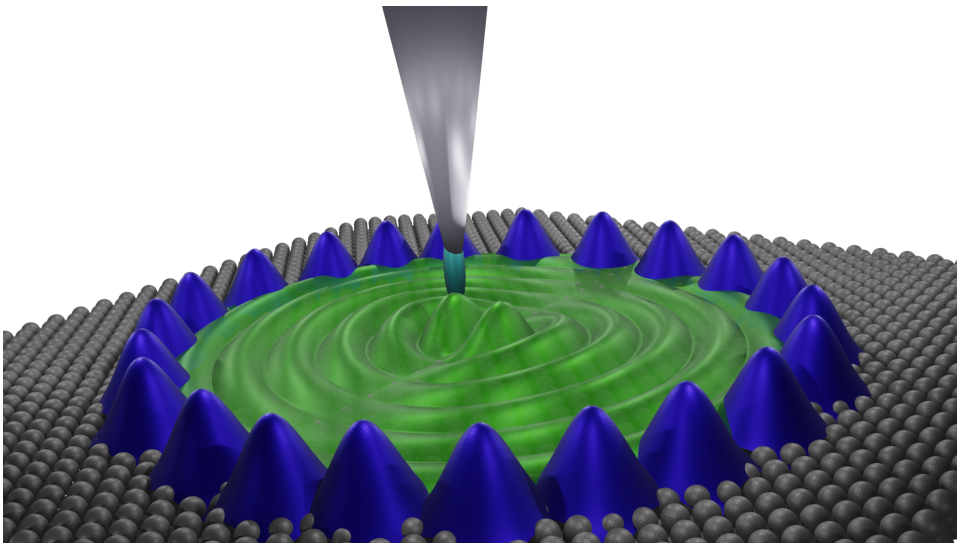

Figure 4.1: Schematic illustration of the experimental setup. In top of the Cu atoms (gray), the 48 Fe adatoms (blue) produce a standing wave pattern (green) of the electronic probability density interacting with the AFM tip.

4.2. Experimental setup

All the experimental data we will discuss in detail in the following sections were obtained in the group of Prof. Giessibl [51]. They used Cu (111) bulk material and on top they arranged 48 iron adatoms in circular form with the STM tip [35, 116] as sketched in Fig. 4.1. The radius $R = 7.13$ nm of the emerging form is chosen from the original experiment in Ref. [36]. All data was measured in ultrahigh vacuum and at a low temperature of $T = 5.7$ K with a combined STM/AFM. To understand and interpret the measured STM (AFM) data we first discuss some fundamental properties of these procedures.

4.2.1. Fundamental properties of STM and AFM measurements

The scanning tunneling microscope (STM) receives information about the surface structure of an electrically conducting substrate by the tunneling current [117]. For this purpose a bias voltage V is applied, whereby electrons from the tip can tunnel through the vacuum potential barrier to an unoccupied state of the substrate [44,118] or vice versa for a negative bias voltage. For small temperatures and a point-like tip, the measured current $I(\boldsymbol{r})$ can be written as

$$I(\boldsymbol{r}, eV) \propto \int_0^{eV} LDOS_{\text{tip}}(\epsilon)\, LDOS_{\text{surf}}(\boldsymbol{r}, \epsilon)\, d\epsilon, \tag{4.1}$$

with the local density of states of the surface (tip) named $LDOS_{\text{surf}}$ ($LDOS_{\text{tip}}$) and e being the elementary charge. For small bias voltages the LDOS of the tip can usually

be assumed to be constant in energy, such that the current is direct proportional to the integral of the $LDOS_{\text{surf}}$,

$$I(\boldsymbol{r}, eV) \propto \int_0^{eV} LDOS_{\text{surf}}(\boldsymbol{r}, \epsilon)\, d\epsilon. \tag{4.2}$$

A topographic measurement as used in Ref. [51] is keeping the current constant by adapting the tip height position via feedback loop. This measurement procedure is avoiding direct contact with e.g. the adatoms. To explore the level broadening of discrete eigenenergies of the surface it is common to study the conductance dI/dV for varying V,

$$\frac{dI}{dV}(\boldsymbol{r}, eV) \propto LDOS_{\text{surf}}(\boldsymbol{r}, eV). \tag{4.3}$$

Another used measurement procedure is the non-contact atomic force microscope (AFM)[2]. In contrast to the STM no current is needed such that the substrate can be isolating. A cantilever with stiffness k is oscillating in z-direction with a given frequency f_0 and amplitude A. If any external force $\boldsymbol{F}$ is acting on the cantilever tip, the frequency will change depending on the z-component of the force. This frequency shift Δf can be estimated by first order perturbation theory: [121]

$$\Delta f(\boldsymbol{r}) = -\frac{f_0}{\pi k A^2} \int_{-A}^{A} \frac{F_z(z-q)\, q}{\sqrt{A^2 - q^2}}\, dq = f - f_0. \tag{4.4}$$

Normally the tip was terminated by metallic atoms, e.g Cu. In 2009 L. Gross et al. used a CO molecule to terminate the tip, which enhanced the resolution significantly [122] due to the locally well defined termination of the tip [123]. Both tip types are used in the experiments of interest here. This information about the AFM and the STM is necessary and sufficient for upcoming sections but for further details about the STM we refer to Ref. [124] and for the AFM to Ref. [124, 125].

Now knowing the precise experimental configuration, we will investigate the applied theoretical approximation to describe the quantum corral by the first successfully used model, the hard wall model.

4.3. Hard wall model

4.3.1. Bandstructure of Cu substrate

To understand the origin of the first theoretical model of the quantum corral, we need to know the electronic structure of the Cu bulk material. The bandstructure of the Cu (111) substrate allows for a powerful simplification [126, 127]: The Fermi energy is lying in the band gap for momenta perpendicular to the surface. In this direction, no Bloch states

[2] Here a self sensing quartz cantilever and a qPlus sensor was used. More details on the experimental setting can be found in Ref. [51, 119, 120].

are available in a range of $[-0.9\text{ eV} + E_F, E_F]$. The arising Shockley surface states[3] exhibit exponential decay in the bulk and vacuum direction, meanwhile the motion in plane can be described by a 2DEG with an effective mass of $m^* = (0.38 \pm 0.02)m_e$ and a energy dispersion given by $E = \frac{\hbar^2}{2m^*}k_\parallel^2 - (440 \pm 10)$ meV [36,118,127,128]. This enables us to investigate the electronic confinement in the quantum corral by a single particle description in two dimensions.

4.3.2. Analytical approach

The approach that the boundary of the quantum corral can be mimicked by an infinitely high potential well in circular form, is resulting in the simplest description of the quantum corrals [36]. Here we will shortly repeat the analytics of this model with extending the model to 3D. The time independent Hamiltonian is defined by

$$H = -\frac{\hbar^2}{2m^*}\left[\frac{\partial^2}{\partial\rho^2} + \rho^{-1}\frac{\partial}{\partial\rho} + \rho^{-2}\frac{\partial^2}{\partial\phi^2} + \frac{\partial^2}{\partial z^2}\right] + V(\rho) + V_z(z) \tag{4.5}$$

and

$$V(\rho) = \begin{cases} -440\text{ meV} & \text{for } \rho \leq R \\ +\infty & \text{for } \rho > R. \end{cases} \tag{4.6}$$

The cylindrical coordinates are chosen such that ρ, ϕ are the variables in plane of the copper surface, while z represents the perpendicular direction. The potential in z-direction is represented by the work function $\Phi_0 = 4.94$ eV and the heaviside step function $\Theta(z)$ [129]: $V_z(z) = \Theta(z)(440\text{ meV} + \Phi_0)$. Here we already introduced a shifted energy scale, where the vaccum level lies at $+\Phi_0$ instead of 0 and the Fermi energy at $E_F = 0$ instead of $E_F = -\Phi_0$. The effective mass in the perpendicular direction is given by $m_z^* = m_e$ and in plane by a mass of $m^* = 0.38m_e$ [127]. The separation ansatz $\psi(\rho, \phi, z) = \chi_\rho(\rho)\chi_\phi(\phi)\chi_z(z)$ for the Schrödinger equation yields:

$$-\frac{\hbar^2}{2m^*}\left[\frac{\partial^2}{\partial\rho^2} + \rho^{-1}\frac{\partial}{\partial\rho} + \rho^{-2}\frac{\partial^2}{\partial\phi^2}\right]\chi_\rho(\rho)\chi_\phi(\phi) = (E - E_\perp - V(\rho))\,\chi_\rho(\rho)\chi_\phi(\phi), \tag{4.7}$$

$$-\frac{\hbar^2}{2m_z}\frac{\partial^2}{\partial z^2}\chi_z(z) = (E_\perp - V_z(z))\,\chi_z(z). \tag{4.8}$$

The only normalizable solution of Eq. (4.8) for the bound state $E_\perp = 0$ is

$$\begin{aligned} \chi_z(z) &= \sqrt{\frac{2}{\lambda_z}}e^{-z/\lambda_z} \\ \lambda_z &= \sqrt{\frac{\hbar^2}{2m_z^*(440\text{ meV } + \Phi_0)}} = 84.2\text{ pm}. \end{aligned} \tag{4.9}$$

[3]More detailed information about Shockley surface states can be found in Ref. [118].

The angular part of Eq. (4.7) is solvable by the ansatz

$$\chi_{\phi,l}(\phi) = c_1 e^{il\phi} + c_2 e^{-il\phi}.$$

Due to $\pm l$ degeneracy, any superposition is possible. We will choose here

$$\chi_{\phi,l}(\phi) = \frac{1}{\sqrt{2\pi}} e^{il\phi}$$

in which l is restricted by the requirement of single-valued functions:

$$\chi_{\phi,l}(\phi) = \psi_{\phi,l}(\phi + 2\pi) \quad \Rightarrow l \in \mathbb{Z}.$$

The radial solution of

$$-\frac{\hbar^2}{2m^*}\left[\frac{\partial^2}{\partial\rho^2} + \rho^{-1}\frac{\partial}{\partial\rho} - \frac{l^2}{\rho^2}\right]\chi_\rho(\rho)\chi_\phi(\phi) = (E - V(\rho))\,\chi_\rho(\rho)\chi_\phi(\phi)$$

can be written as

$$\begin{aligned} \chi_{\rho,l}(\rho) &= cJ_l(k\rho), \\ k &= \sqrt{\frac{2m^*(E - V(r))}{\hbar^2}} \end{aligned} \tag{4.10}$$

where $J_l(k\rho)$ is the Bessel function of first kind [130]. The singularity of the second solution, a Bessel function of second kind $Y_l(k\rho)$, for $\rho = 0$ is in conflict with our demand of well-behaving functions. To satisfy the boundary condition at $\rho = R$ the k-values depending on the n-th zero of the l-th Bessel function $z_{n,l} = z_{n,-l}$ has to fulfill:

$$J_l(kR) = 0 \Rightarrow k_{n,l} = \frac{z_{n,l}}{R} \tag{4.11}$$

$$\Rightarrow E_{n,l} = \frac{\hbar^2 z_{n,l}^2}{2m^* R^2} - 440 \text{ meV}. \tag{4.12}$$

The energies are thus double degenerate by $\pm l$. To summarize, the normalized solution of Eq. (4.5) is given by

$$\psi_{n,l}(\rho, \phi, z) = \frac{c}{\sqrt{\pi\lambda_z}} e^{il\phi} J_l(k_{n,l}\rho) e^{-z/\lambda_z} \tag{4.13}$$

where c is given by [131, p. 643]

$$c^{-2} = \frac{R^2}{2}\left[J_l^2(k_{n,l}R) - J_{l-1}(k_{n,l}R)J_{l+1}(k_{n,l}R)\right].$$

Each eigenstate $\psi_{n,l}(\rho, \phi, z)$ is therefore double degenerate for $\pm l$ and displays $n - 1$ nodes in radial direction. Due to the spin degeneracy each $E_{n,l}$ is populated by two electrons with antiparallel spin.

4.3.3. Comparison to STM measurements

Next we want to compare the eigenstates of the hard wall model with the current $I(\boldsymbol{r})$ measured by STM. The LDOS is given by a summation over all eigenstates at energy ϵ,

$$LDOS(\boldsymbol{r}, \epsilon) = \sum_{(n,l)} 2 \left|\psi_{n,l}(\boldsymbol{r})\right|^2 \delta(\epsilon - E_{n,l}), \tag{4.14}$$

while taking the spin degeneracy of two into account. The current $I(\boldsymbol{r})$ is in accordance with Eq. (4.2) depending on the LDOS by

$$I(\boldsymbol{r}) \propto \int_{E_F - eV}^{E_F} LDOS(\boldsymbol{r}, \epsilon)\, d\epsilon.$$

As shown in the previous section, the integrated LDOS has the same decay rate in z-direction at all positions on the surface plane. Thereby for the topographic measurement, where the tip height positions for constant current are detected, it is sufficient to compare the relative height with the 2D LDOS $\sigma_{\text{Fermi}}(\rho, \phi)$,

$$\sigma_{\text{Fermi}}(\rho, \phi) = \sum_{\nu} 2 \left| \frac{c}{\sqrt{2\pi}} e^{il\phi} J_l(k_{n,l}\rho) \right|^2, \tag{4.15}$$

were ν denotes all tuples (n, l) with energies in the chosen energy range $[E_F - eV, E_F]$. The $\pm l$ degenerate eigenvalues of the hard wall model calculated from Eq. (4.12) are illustrated in Fig. 4.2(a). For a bias voltage of $eV = 10$ meV the tuples (n, l) with energies in the relevant energy range are given by $\nu = \{(2, \pm 7), (4, \pm 2), (5, 0)\}$ and are marked in green. The summation over these states results in $\sigma_{\text{Fermi}}(\rho, \phi)$ shown in Fig. 4.2(b) and coincides qualitatively with the experimentally achieved topographic image in Fig. 4.2(c). In the experiment the Fe adatoms producing the quantum corral are clearly visible as bright spots[4]. A direct comparison of $\sigma_{\text{Fermi}}(\rho, \phi = 0)$ and angle-averaged STM data in Fig. 4.2(d) is persuasively showing the agreement between the hard wall model and the measured data, as already done in Ref. [36].

When studying other properties, e.g. the energy broadening of each individual state, the hard wall model with its discrete eigenenergies illustrates its own limitation. Already in Ref. [36] the dI/dV spectra identifies the finite lifetime of the surface states. A multiple scattering expansion gave more information [38]. Around 50% of an incident amplitude are getting transmitted through the boundary build up by the adatoms and stay on the surface. 25% are getting absorbed into the bulk after being scattered at the adatoms. Therefore only 25% are getting reflected back into the corral. According to Ref. [36, 44] the adatoms are better described by a "black dot" with a scattering phase of the zero angular momentum state $\phi_{l=0} = i\infty$ than by perfectly reflecting walls as assumed in the hard wall model. In the following sec. 4.4 we will establish a new tight-binding system which features more agreements with experiments than the hard wall model by adapting the experimentally achieved scattering phase.

[4] The Fe atom at $(x, y) = (-1, -0.8)R$ is not influencing the appearing standing wave pattern, it is experimentally used as a backup when Fe atoms get lost.

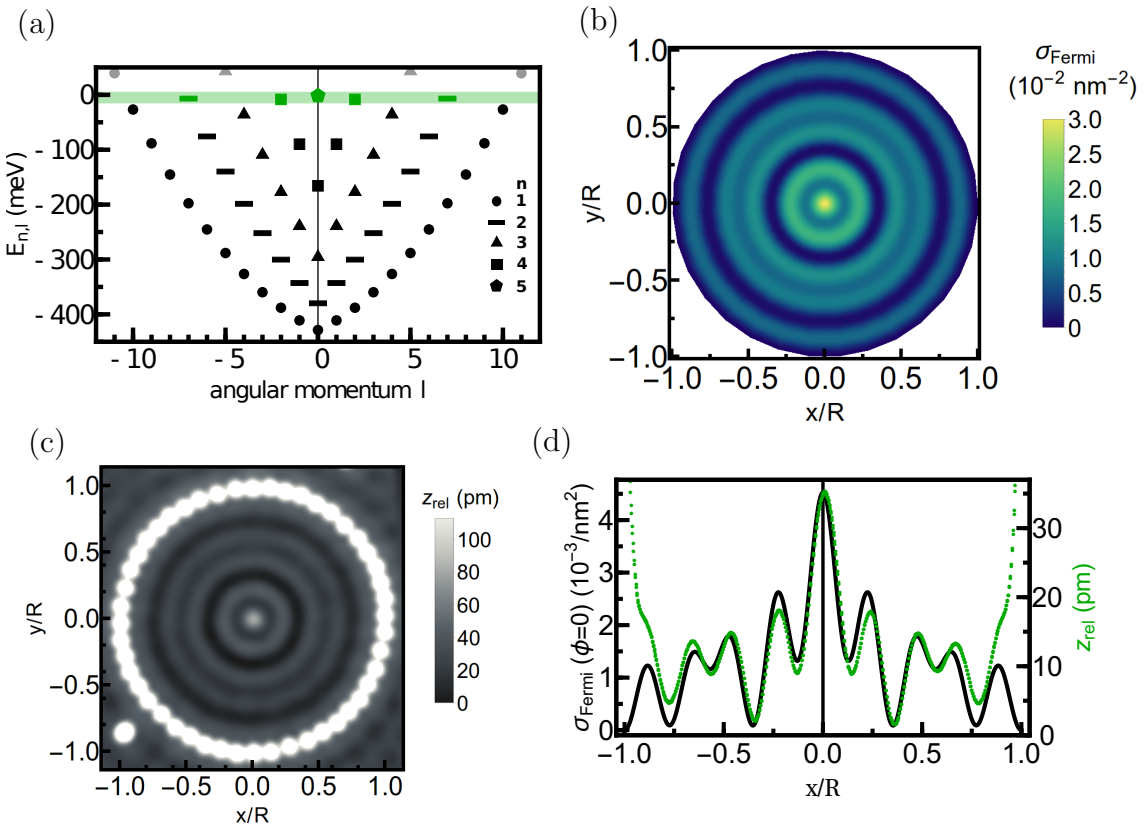

Figure 4.2: The hard wall model explains the topographic STM measurements for a quantum corral of radius $R = 7.13$ nm. In (a) we show the eigenvalues of the hard wall model where the double degeneracy for angular momentum $\pm l$ is visible. The energy range in which the STM with an applied voltage of $eV = 10$ meV is sensible, is illustrated as a green area. The summation of eigenstates in this range results in σ_{Fermi} shown in (b). A rotational symmetry and five radial maxima are clearly visible. The measured constant current data in (c) exhibits the same characteristic. A linescan for varying ρ in (d) displays the agreement between σ_{Fermi} and angle-averaged height data z_{rel} in more detail.

4.4. Modeling the quantum corral including the scattering phase

We want to investigate a new model to describe the quantum corral data received by STM measurements in more detail as the hard wall model. For that, the crucial input is the scattering phase. The common method to do so is called the multi scattering approach. Here, the electron is incoming from the tip and scattered at the adatoms of the surface. The interference of in- and outgoing amplitudes is then generating fluctuations of the LDOS. The imaginary part of the retarded Green's function is proportional to the LDOS and is calculated by assuming only spherically symmetric (s-wave) scattering [36–38]. This approach was successfully applied to different corral shapes, from billiard, parabolas to half circles [37, 114, 115, 132]. In contrast to that, we will establish a new model of the quantum corral using a tight-binding approximation by the software package Kwant [72]. The 2D Hamiltonian achieved by the neglect of all z-dependency in Eq. (4.5) is discretized on a grid and by introducing a coupling to leads it gives access to the LDOS. A fast implementation, convenient handling and broad spectrum of features are the advantages of this method. To include a detailed scattering mechanism, we will first adapt the experimental scattering phase to our numerical setup. Then, in sec. 4.4.2 we calculate the LDOS for a quantum corral hosting another Fe adatom inside and find convincing agreement to experiments for all positions of this extra adatom. The strength of our chosen approach is also confirmed by determining the Cu (111) symmetry (sec. 4.4.3). We will not cover this here, but the same approach yields agreement to experiments on a quantum corral build out of CO molecules instead of Fe atoms [133].

4.4.1. Scattering phase adaption

In this work we will stick to a real scattering phase, which is known to provide a satisfying standing wave pattern for $\phi_{l=0} = -80°$ in accordance to experiments [36, 38].

It is not our goal to describe the complex interplay between the adatom and the Cu substrate at the adatom. Our ambition is the description of the standing wave pattern influenced by the adatoms. An adatom is simulated by a circular potential well,

$$V(\rho) = \begin{cases} 0 & \text{for } \rho \geq R_{\text{ad}} \\ a & \text{for } \rho < R_{\text{ad}}, \end{cases} \tag{4.16}$$

while the potential strength is chosen such that the resulting LDOS coincides with the experiments. For this purpose we first need to know the regime for a and R_{ad} where the scattering phase is in the vicinity of $\phi_{l=0} = -80°$. For purely real scattering phases, the results are invariant for $\phi_{l=0} + \pi$ and therefore $\phi_{l=0} = +100°$ is also a possible choice. To find the principle dependency of the scattering phase on the free parameters, one uses 2D scattering theory. The relevant equation is given by Eq. (28) in Ref. [134]. A mistake in writing in Ref. [134] forces us to recapture the derivation, done in appendix C. The

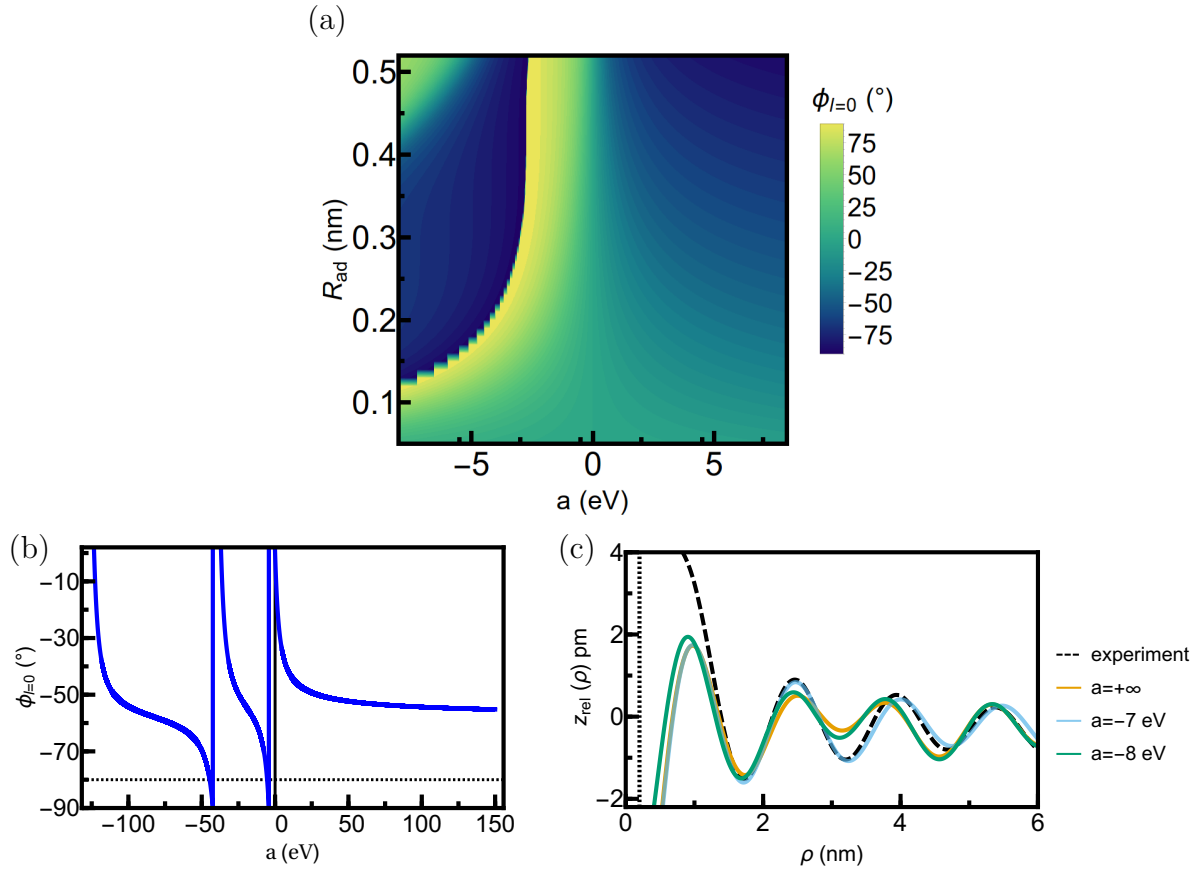

Figure 4.3: To simulate the scattering at each adatom, we adjust the parameters of the circular potential well. In (a) the resulting scattering phase of Eq. (4.17) for varying potential strength a and radius R_{ad} is shown. To reach a scattering phase of $\phi_{l=0} = -80°$, either we chose $a > 0$ and a diameter of more than 1 nm or an attractive potential well with a radius in $R_{ad} \in [0.1, 0.5]$ nm. To fulfill the s-wave approximation $a < 0$ is necessary. In (b) the 2D scattering theory yields the scattering phase $\phi_{l=0}$ for a given radius of the adatom $R_{\text{ad}} = 0.2$ nm and varying potential strength a by Eq. (4.17). The intended scattering phase of $\phi_{l=0} = -80°$ is illustrated by the dashed line. For $a \in [-8, -4]$ eV this can be achieved. In (c) we adjust this further: The topographic STM measurement for one single adatom gives the linescan profile shown in black whereby we can fit the numerical LDOS of different potential strengths to it. The potential strength of $a = -7$ eV results in the most convincing agreement.

correct formula is plotted in Fig. 4.3(a) for varying radius R_{ad} and potential strength a:

$$\tan\phi_{l=0} = \frac{-\tilde{k}J_0(kR_{\mathrm{ad}})J_1(\tilde{k}R_{\mathrm{ad}}) + kJ_0(\tilde{k}R_{\mathrm{ad}})J_1(kR_{\mathrm{ad}})}{-kY_0(\tilde{k}R_{\mathrm{ad}})J_1(kR_{\mathrm{ad}}) + \tilde{k}Y_1(\tilde{k}R_{\mathrm{ad}})J_0(kR_{\mathrm{ad}})}. \tag{4.17}$$

Here, the momenta inside and outside of the potential well are given by $\tilde{k} = \sqrt{2m^*(E-a)}/\hbar$ and $k = \sqrt{2m^*E}/\hbar$. The exact radius of the potential well is not important, but it should be in the same order of magnitude as the approximate Fe atom size (≈ 0.27 nm [38]) such that the Fermi wavelength $\lambda_F \approx 3$ nm is much bigger than R_{ad}. Therefore the assumption of only s-wave scattering is valid. For a repulsive potential well ($a > 0$) the scattering phase is smoothly increasing when either R_{ad} or a is rising. For $R_{\mathrm{ad}} < 0.5$ nm, the maximal phase shift reachable is around $-55°$. Our intended phase $\phi_{l=0}$ can be achieved, but due to $R_{\mathrm{ad}} \not\ll \lambda_F$, it violates the s-wave approach. Therefore an attractive potential strength is required. For $a < 0$, the scattering phase instead displays discontinuities and sudden extreme values of $\phi_{l=0}$ generated by the bound states of the circular potential well. This is visible in Fig. 4.3(b) where we fixed the adatom radius $R_{\mathrm{ad}} = 0.2$ nm. The black dashed line illustrates the phase shift of $-80°$. The repeating structure allows for infinitely many negative potential strengths a, but we will concentrate on the regime $a \in [-8, -4]$ eV. The numerical implementation of this potential well is neither perfectly describing a circular potential well nor simulating the abrupt change in the potential strength exactly. For that reason in addition to the 2D scattering theory, we compare the LDOS arising from different potential strengths to the experiment to determine a more accurate value for a. In the STM measurement, a bias voltage (10 meV) is applied and instead of the circular form built by 48 adatoms, a single Fe adatom is positioned on the Cu (111) surface. A linescan of the resulting topographic STM image is illustrated in Fig. 4.3(c) by a black dashed line. When approaching the adatom with the tip, one needs to pass the additional height of the adatom. Therefore the relative height h_{rel} increases for $\rho \leq 1.2$ nm. This geometrical height difference to the surface is not included in our approach so that we compare the resulting LDOS in a range of $\rho \in [1.2, 6]$ nm. The vertical dashed line in Fig. 4.3(c) illustrates the radius R_{ad} of the simulated adatom. To compare the current with the numerical results, we fit a prefactor and an offset to the LDOS. This is done for every LDOS gained by individual potential strengths a and yields the three different lines in Fig. 4.3(c). With a potential strength of $a = -8$ eV and $a = +\infty$ the resulting LDOS are almost equivalent and slightly disagree with the experiment in the range of $\rho \in [2, 5]$ nm. A better agreement to the STM data in the range $\rho \in [1.2, 4.5]$ nm is illustrated for a potential strength of $a = -7$ eV. It is worth to mention that we do not succeed in determining a potential strength reproducing a more satisfying agreement. Possible an adaption of R_{ad} could enhance this further. Also the wave length of the numerical achieved LDOS appears bigger than the experimental one. Certainly, a slight modification in the range of uncertainty of the effective mass m^* or the energy shift (-440 meV) of the 2DEG can improve this. The description for scattering at individual adatoms when using a potential strength of $a = -7$ eV will now be tested for different situations. We will compare the STM measurements with the tight-binding model for the quantum corral with and without additional adatoms.

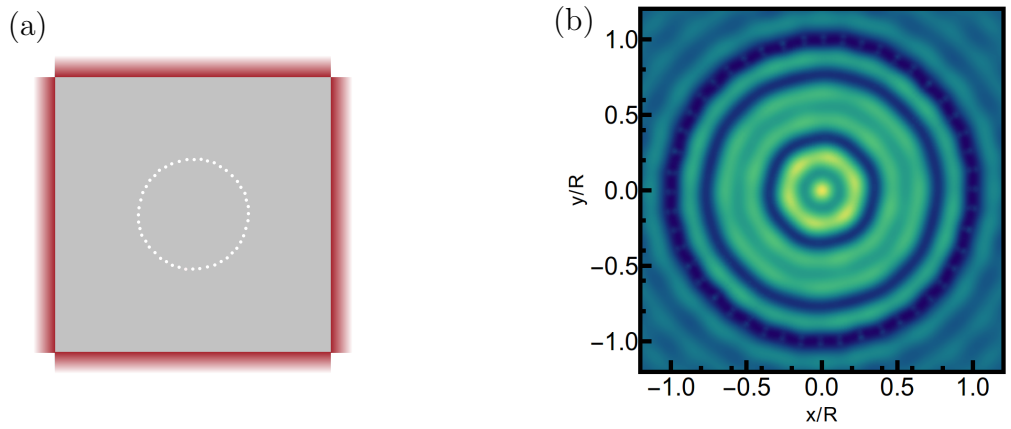

Figure 4.4: The adjusted phase model for the quantum corral exhibits the same undulations as the STM data. Panel (a) shows a sketch of the tight-binding implementation, at which the four leads are marked red and the Fe adatoms are illustrated by white circles. Panel (b) shows the numerically achieved LDOS in the quantum corral for the tight-binding model. A qualitative agreement to Fig. 4.2(c) is given. Reflection effects at the system-lead interface are minimized and therefore not visible.

4.4.2. Variation of adatom position

Every adatom, 48 for building the corral and one optional adatom inside the circle, is represented as a circular potential well with strength $a = -7$ eV in the tight-binding model. Whereby all Fe positions in the simulation are determined by the experimental setup. To avoid scattering at the artificial boundaries of a finite system, we use a large squarish system with the corral centered in the middle and connect the boundaries of that square to leads as sketched in Fig. 4.4(a). The implementation without an extra adatom inside yields the LDOS shown in Fig. 4.4(b). The qualitative agreement to the experiment in Fig.4.2(c) is clearly visible.

So far both the hard wall model and the tight-binding model with the adjusted phase give sufficient agreement to experimental data. Now we turn to setups with an additional adatom inside the corral. For the hard wall model the 48 Fe atoms building the corral are still simulated by the hard wall for $\rho \geq R$. The additional atom is described by a circular potential well but with infinite potential strength $a = +\infty$ [5]. For the radius of the potential well we choose also R_{ad}. Of course this choice is arbitrary and is only intended to show the discrepancy to an adjusted phase model. To solve the Schrödinger equation for this scenario perturbation theory is one possible choice. We will instead use a tight-binding model without leads. Diagonalising this Hamiltonian and summing the eigenvectors in the operating energy range of $[E_F - 10\text{ meV}, E_F]$ yields the LDOS of the hard wall model. The comparison of the hard wall model and the model

[5]Simulations show that using a circular potential well with radius R_{ad} and $a = +\infty$ also for each adatom building the corral is not influencing the resulting LDOS.

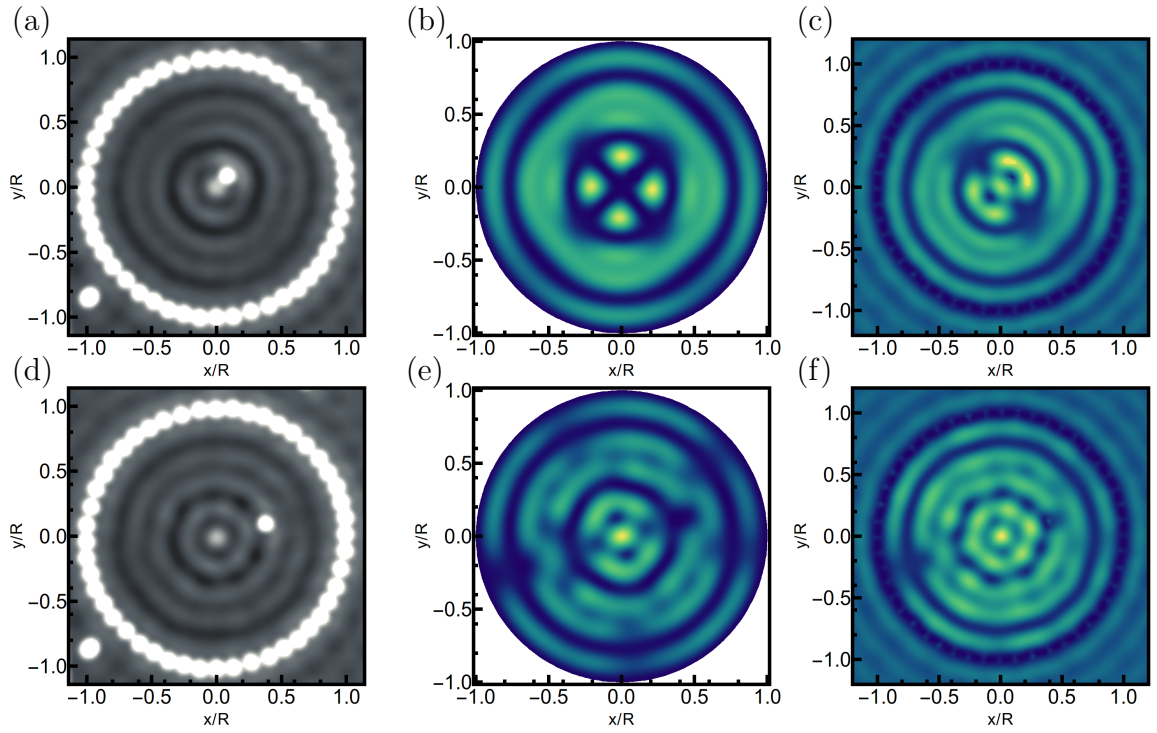

Figure 4.5: The topographic experimental data, the hard wall model and the adjusted phase model display different agreements. In the first row, the STM data for an additional Fe adatom at $\rho_{\mathrm{ad}} = 1.2\,R = 0.88$ nm (a) exhibits drastic differences to the solution of the hard wall model shown in (b). The characteristic undulations are more in coincidence with the LDOS of the adjusted phase model. Positioning the Fe atom at $\rho_{\mathrm{ad}} = 0.39\,R = 2.8$ nm gives rise to azimuthal ripples in the second radial minimum of the STM measurement shown in (d). The LDOS of the hard wall model shown in (e) does not share this undulation. The result of the adjusted phase model in (f) with a potential strength of $a = -7$ eV again qualitatively agrees with the experiment.

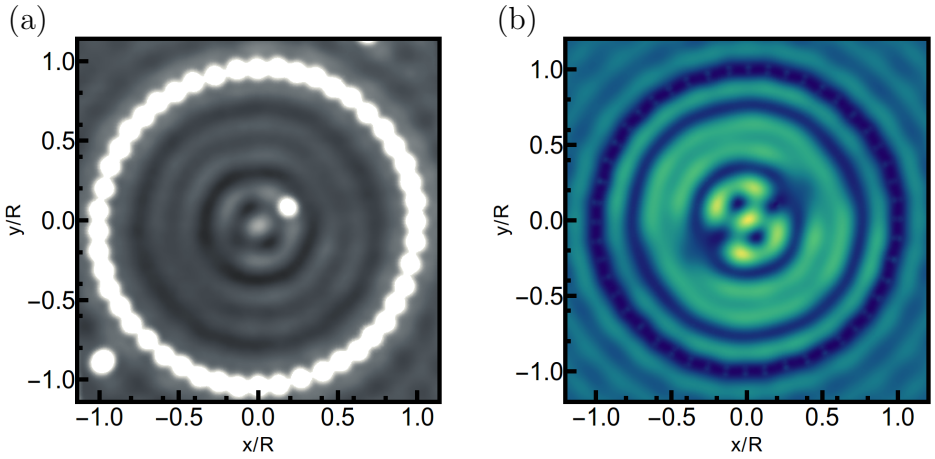

Figure 4.6: The topographic STM data for $\rho_{\mathrm{ad}} = 0.22\,R = 1.6$ nm in (a) qualitatively agrees with the tight-binding model with adjusted scattering phase in (b).

with finite potential strength to experiments is shown in Fig. 4.5. Here we select two ($\rho_{\mathrm{ad}} = 1.2\,R = 0.88$ nm and $\rho_{\mathrm{ad}} = 0.39\,R = 2.8$ nm) of several adatom positions where the hard wall model fails. For $\rho_{\mathrm{ad}} = 1.2\,R$ the LDOS of the hard wall model in (b) exhibits in the first radial maxima an angular period of $\pi/2$, a signature not present in the STM data shown in (a). The qualitative agreement to the adjusted phase model in (c) on the contrary is definitely visible. The increased amplitudes of the second radial maximas next to the adatom are in both images present. When moving the adatom to $\rho_{\mathrm{ad}} = 0.39\,R = 2.8$ nm the topographic data in (d) shows undulations of the second minimum in radial direction. This oscillation also appears when using the adjusted phase model as plotted in (f). Again in the LDOS of the hard wall model shown in (e) this characteristic is not observable. We conclude that due to discrepancies between the scattering phase of the hard wall model and the actually measured one, the hard wall model is only applicable when no Fe adatom is positioned in the quantum corral, otherwise the resulting LDOS does not share the same characteristics as the topographic STM measurements.

To confirm the shown agreement of the new model with experiments we now investigate the setup for two more adatom positions. In Fig 4.6 we compare the data for $\rho_{\mathrm{ad}} = 0.22\,R = 1.6$ nm where the measured relative height z_{rel} in (a) shares again the same undulations as the LDOS achieved by the adjusted phase model shown in (b). The azimuthal and radial undulations coincide qualitatively.

Moving the Fe adatom to $\rho_{\mathrm{ad}} = 0.57\,R$ gives rise to a different oscillation in the LDOS. In Fig 4.7 the STM data in (a) coincides qualitatively with the numerical results of the adjusted phase model in (b). Linescans of both data sets shown in (c), where we vary the angle ϕ and fix ρ to $\rho = \rho_{\mathrm{ad}}$, illustrate the same azimuthal undulations with a period of $\pi/7$. A rough but intuitive explanation of this periodicity can be given by the hard wall model: As already pointed out in Fig. 4.2, without the adatom inside the corral the Bessel functions shown in Fig 4.7(d) are solutions of the hard wall model in the energy range the

STM is sensitive. When the extra adatom is positioned at $\rho_{\mathrm{ad}} = 0.57/R$, as sketched by the black dashed line, the degenerate Bessel states with $(n, l) = (2, \pm 7)$ are most affected. They will form new states of the form $\sin(l\phi)$ and $\cos(l\phi)$, whereas the one with high amplitudes at the adatom position will be lifted up in energy. This state lying above E_F is then not occupied any more and thus not affecting the STM signal. Meanwhile the other state is generating the azimuthal oscillations with a period of $\pi/l = \pi/7$. Of course this is just an argumentation to understand the arising undulations, estimations about the energy shift of each state have to be done more carefully, e.g by perturbation theory or as chosen here a tight-binding implementation.

In the linescan of the STM data shown in Fig. 4.7(c) the amplitude of this oscillation is decreasing with increasing distance to the adatom positioned at $(x_{\mathrm{ad}}, y_{\mathrm{ad}}) = (0.55, 0.014)R$. This characteristic is not visible in the LDOS achieved by the adjusted phase model. Reasons for this can be diverse: The scattering phase adaption is not exact and a small discrepancy can result in different interference patterns. Another possibility is the neglect of absorption effects into the bulk by using a purely real scattering phase. The implementation of these effects by imaginary self-energy, can shine some light on this disagreement.

The hexagonal structure of the first radial maxima in Fig.4.7(b) is a further visible characteristic. When positioning an adatom in the center of the quantum corral this is more pronounced and will be investigated in the following.

4.4.3. Determining the underlying copper symmetry

The surface of the Cu (111) face-centered cubic lattice is building a hexagonal grid with a rotational symmetry of 60° [135]. In Fig. 4.8(a) a top view of the first two Cu layers in blue and green is shown. A Fe atom, sketched in red, is most stable at swales of the Cu grid. When now positioning 48 Fe atoms on the Cu surface, the resulting quantum corral has specific geometrical properties: It is building a polygon of 24 sides, at which three possible distances between two neighboring Fe atoms, $a = \sqrt{12}d$, $b = \sqrt{13}d$ and $c = 4d$ with $d = 255$ pm arise [51]. The first quadrant of the quantum corral is displayed in Fig. 4.8(b) [136]. In the topographic STM data (c) and better visible in the tight-binding simulation (d) the first maxima appear in a hexagonal form. In the latter we see the alignment of the hexagon to the longest side c of the polygon of 24 sides. In the tight-binding simulation, the Cu substrate is not implemented, so no direct influence on the LDOS is possible. Only the exact Fe positions are reproduced in the simulation. The constraint of the Fe adatom positions stemming from the Cu substrate is a fact, which affects the numerical LDOS as visible in (d). This argument is however not applicable in general. When only states with low number of angular momentum l are involved, such that $180°/l \ll 60°$, the states can not adapt themselves to the Fe adatom structure. The resulting LDOS will not share the same symmetry as the Cu substrate. This is confirmed by further numerical investigations we made.

In the previous sections we analyzed the STM measurements in detail, while leaving the experimental AFM results from Ref. [51] aside. Now we will move our focus on this data, where the advanced measurement procedure give rise to new physical questions.

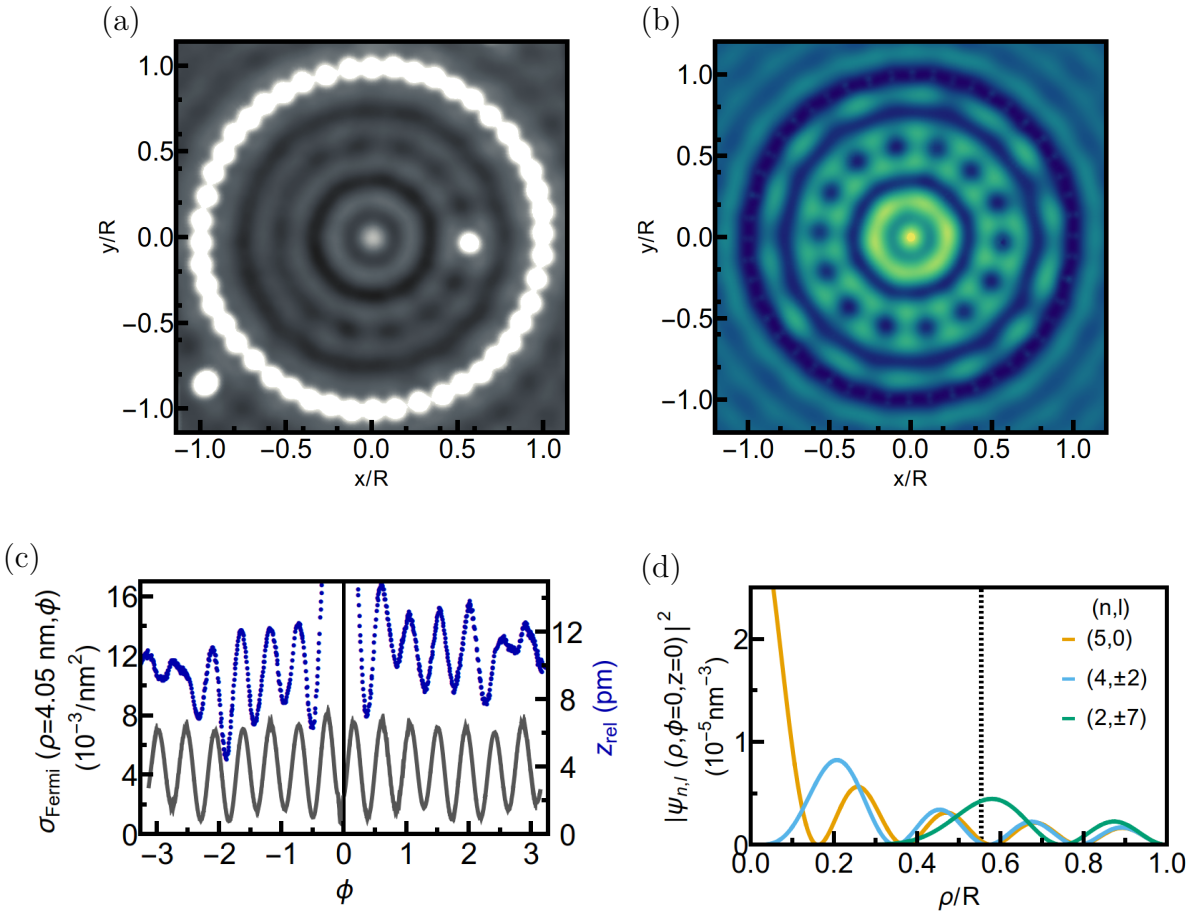

Figure 4.7: The topographic STM picture for $\rho_{\mathrm{ad}} = 0.57\,R = 4.05$ nm in (a) qualitatively agrees with the tight-binding model with adjusted scattering phase shown in (b). (c) shows angular linescans at $\rho = \rho_{\mathrm{ad}}$ of both data sets, which highlight the appearing undulation with period $\pi/7$. The hard wall solutions of the quantum corral without adatom are the Bessel functions shown in (d). The $(n, l) = (2, \pm 7)$ states, most affected by an adatom at ρ_{ad} (dashed line), will be perturbed and are therefore generating an undulation with period $\pi/7$.

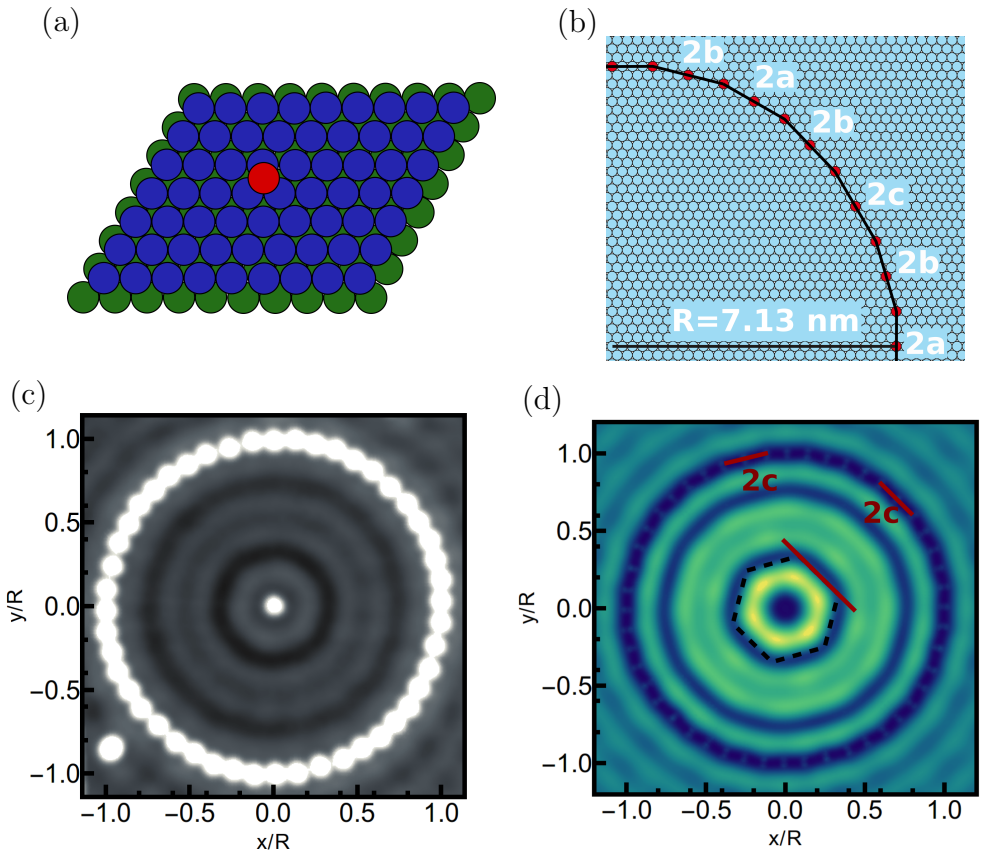

Figure 4.8: The Cu substrate symmetry is affecting the Fe adatom positions and therefore the resulting standing wave pattern. In (a) two layers (green, blue) of the Cu (111) hexagonal lattice are shown. The Fe adatom is most stable at swales of the Cu grid as illustrated in red. This constraint for the 48 Fe atom positions is affecting the geometric structure of the quantum corral. The corral forms a polygon with 24 sides, while three atoms are always connected by one strait line with a length of a, b or c. The first quadrant of this is shown in (b) [136], where the red circles again sketch the Fe atoms. When positioning an adatom at the center of the quantum corral, the topographic image in (c) and the numerically LDOS in (d) display a hexagonal structure in the first radial maxima.

4.5. Bonding properties between tip and quantum corral states

Properties of the quantum corral concerning STM measurements are intensively studied in the previous sections. However, one major aspect of the experimental data from Ref. [51] are the AFM measurements of the quantum corral. The atomically resolved AFM measurements of forces which are three orders of magnitude smaller than the typically measured ones, enable deeper analysis of the appearing forces. The strong decay of the involved forces between the mesoscopic surface state and the tip gives rise to several questions: Is this decay caused by electrostatic interactions between the tip and the surface states? Do the states of the artificial atom formed by the quantum corral interact with the tip orbitals via chemical bonding? If so, which corral states are building the analogy to open shell orbitals dominating the chemical bonds in molecule physics?

To get a deeper understanding of the appearing phenomena, we first need to clarify some basic facts. In the AFM measurements several forces are acting on the tip, all depending on the sample-tip distance. Far away from the surface the Van-der-Waals forces[6] dominate, replaced by the chemical bonding or Pauli repulsion when the distance is reduced [137, 138]. To decrease the influence of the Van-der-Waals forces, contrasts of Δf instead of Δf are used. They are oppositional defined by

$$\begin{aligned} \Delta f_{\mathrm{Cu}} &= \Delta f(\rho_{\mathrm{max1}}, z) - \left(\Delta f(\rho_{\mathrm{min1}}, z) + \Delta f(\rho_{\mathrm{min2}}, z)\right)/2 \\ \Delta f_{\mathrm{CO}} &= -\Delta f(\rho_{\mathrm{min1}}, z) + \left(\Delta f(\rho_{\mathrm{max1}}, z) + \Delta f(\rho_{\mathrm{max2}}, z)\right)/2. \end{aligned} \tag{4.18}$$

It is experimentally validated and supported by density functional theory (DFT), that the metallic tip is normally interacting with the surface states attractively [139], while the CO terminated tip is exhibiting a repelling interaction due to Pauli repulsion [140–142][7]. To observe the attractive or repulsive force one has to isolate the effects of the surface states by computing the contrast of the frequency shift. To deal only with positive contrasts of frequency shifts, they are defined as shown in Eq. (4.18). In accordance to Eq. (4.4) in sec. 4.2.1, an attractive (repulsive) force is influencing the frequency shift to negative (positive) values. So that the metallic (CO) tip is normally resulting in negative (positive) frequency shifts when interactions with surface states are considered. The Pauli repulsion of the CO tip is normally sensitive to the total charge density, so we first define the total charge density in the quantum corral setup: The 2D total charge density $\tilde{\sigma}$ is in analogy to the LDOS in sec. 4.3.2 given by

$$\tilde{\sigma}(\rho, \phi) = 2e \sum_{\mu} |c e^{il\phi} J_l(k_{n,l}\rho)|^2, \tag{4.19}$$

where μ is specifying all states (n, l) fulfilling

$$-440 \text{ meV} \leq E_{n,l} \leq 0. \tag{4.20}$$

[6] The Van-der-Waals force consists of (induced) dipol-(induced) dipol forces [124].
[7] Indeed for the CO terminated tip some exceptions of this are known [138, 143].

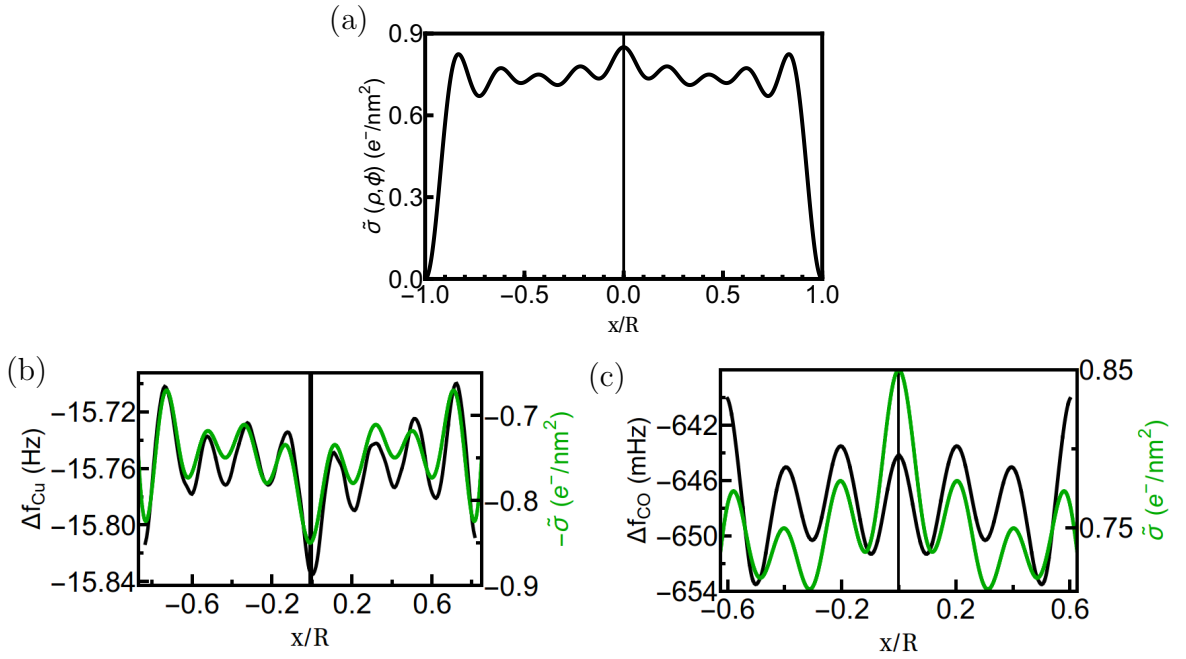

Figure 4.9: The measured frequency shift is proportional to the total charge density $\tilde{\sigma}$. In panel (a) we show a linescan of $\tilde{\sigma}$ for $\phi = 0$. In (b) the frequency shift govern by an AFM linescan for a metallic tip (black) agrees with $-\tilde{\sigma}$ illustrated in green. In (c) the principle agreement of the frequency shift (black) with a CO terminated tip and the total charge density (green) is displayed, however the maximum at the center is less pronounced.

The summation over all states is resulting in the total charge density $\tilde{\sigma}$ for which a linescan for $\phi = 0$ is displayed in Fig. 4.9(a).

In the experiment of Ref. [51] the frequency shift Δf for two different tips, a metallic Cu and a CO terminated one, is measured by AFM. The frequency shift Δf for varying ρ and fixed height $z_{\text{tip}} = 440$ pm ($z_{\text{tip}} = 410$ pm) is measured with a metallic (CO) tip and the resulting data is displayed in Fig. 4.9(b) respectively (c). Both frequency shifts are negative which illustrates that both tips experience a net attractive force due to Van-der-Waals interactions. In both cases the radial oscillations partly are described by the total charge density plotted in black. For a CO terminated tip there is less accurate agreement to $\tilde{\sigma}$ around $x/R = 0$. This can be explained by perturbation theory: When the metallic (CO terminated) tip is approaching the surface the attractive (repulsive) force perturbs the quantum corral energies $E_{n,l}$ of the 3D states $\psi_{n,l}(\rho, \phi, z)$ defined in Eq. (4.13) by $\Delta E_{n,l}$. Using first order perturbation theory, this energy shift is given by

$$\Delta E_{n,l} = \langle \psi_{n,l}(\rho, \phi, z) | V_{\text{tip}} | \psi_{n,l}(\rho, \phi, z)) \rangle,$$

whereby $\Delta E_{n,l}$ is negative (positive) for the metallic (CO) tip. A detailed analysis also

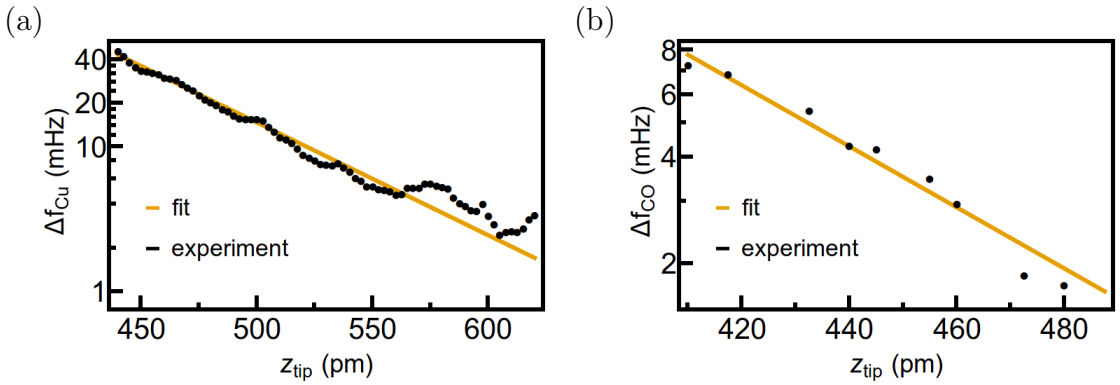

Figure 4.10: Measurements of the frequency shift result in exponential decaying contrasts. (a) shows the measured values (black) and an exponential fit with $\lambda_{\mathrm{Cu}} = 55.7$ pm in orange for a tip terminated by a single Cu atom. (b) shows an similar behavior for the experimental results plotted in black with a fitted decay rate of $\lambda_{\mathrm{C0}} = 50.4$ pm in orange with a CO terminated tip.

taking the energetic broadening into account [51] and gives approximate values of $\Delta E_{5,0}$,

$$\Delta E_{(5,0),\mathrm{Cu}} = -0.8 \text{ meV} \tag{4.21}$$
$$\Delta E_{(5,0),\mathrm{CO}} = +0.13 \text{ meV}, \tag{4.22}$$

for $\psi_{5,0}$ and a sample-tip distance of $z_{\mathrm{tip}} = 440$ pm ($z_{\mathrm{tip}} = 410$ pm) for the metallic (CO) tip. The proximity of the $(n, l) = (5, 0)$ state to the Fermi energy makes this state most sensible to the perturbation V_{tip}. Its main probability around $\rho = 0$ is then reasoning the arising discrepancy between $\tilde{\sigma}$ and Δf around $\rho = 0$. For the metallic tip the occupation of the $\psi_{5,0}$ state is slightly increasing. The positive shift in case of the Co terminated tip reduces the $\psi_{5,0}$ occupation and yields therefore a reduced magnitude around $\rho = 0$.

To summarize, the results shown in Fig. 4.9 present oscillations sensitive to the total charge density $\tilde{\sigma}$. For a small sample-tip distance the force of the metallic (CO) tip acting on the surface states is increasing (reducing) the $\psi_{5,0}$ occupation.

Measuring the frequency shift also for varying distances z gives further information about the appearing forces. When building the contrast as given by Eq. (4.18) the z-dependence of both tip types displays exponential decay shown in Fig. 4.10. As expected the contrast of the frequency shift is positive for both tip types. This implicates an attractive (repulsive) force between the surface states and the metallic (CO) tip in accordance to previous studies. In (a) the contrast Δf_{Cu} for the metallic tip can be described by an exponential function with a decay length of $\lambda_{\mathrm{Cu}} = 55.7$ pm for $z \in [450, 600]$ pm. In analogy Δf_{CO} in (b) has a decay length of $\lambda_{\mathrm{C0}} = 50.4$ pm for $z \in [410, 480]$ pm. Both decay rates are in the order of the decay length $\lambda_z = 84.2$ pm (see Eq. (4.9) in sec. 4.3.2) of the quantum corral surface states. What is reasoning such strong decays for the two fundamentally different tips?

We know that arising from dipole moments both tips are electrically charged by $q_{\mathrm{CO}} = -0.03e$ and $q_{\mathrm{Cu}} = +0.13e$ [144]. To exclude the possibility of a purely electrostatic

interaction we numerically calculate the Coulomb interaction between a charged point-like tip and the 2D surface states in a quasi-classical kind in sec. 4.5.1. This assumption of a point-like tip is valid, because the appearing atomic radii of $\alpha_{\mathrm{Cu}} = 132$ pm and $\alpha_{\mathrm{CO}} = 66$ pm are both significantly smaller than the radial wave length of the quantum corral eigenstates ($\lambda \approx 3$ nm) [145]. And besides, the surface-tip distance z fulfills $z \geq 132 \text{ pm} > \alpha_{\mathrm{Cu/CO}} + 2\lambda_z$ and therefore justifies a 2D description of the surface states. The resulting decay of $\Delta f_{\mathrm{Cu/CO}}$ in this approach is in conflict with the measured decay of the contrast from Fig. 4.10. Therefore we will investigate the overlap of the involved orbitals seeing that as the first step to describing the bonding using linear combination of atomic orbitals (LCAO) method in sec. 4.5.2.

4.5.1. Quasi-classical Coulomb interaction

The electric field of the surface charge density $\tilde{\sigma}(\rho', \phi')\delta(z')$ causes a Coulomb force acting on the point-like tip at position $\boldsymbol{r}$ with charge q_{tip}. This force vector is given by

$$\boldsymbol{F}(\boldsymbol{r}) = \frac{q_{\mathrm{tip}}}{4\pi\epsilon_0\epsilon} \int dV' \, \frac{\tilde{\sigma}(\rho', \phi')\delta(z')}{|\boldsymbol{r} - \boldsymbol{r}\,'|^2} \frac{\boldsymbol{r} - \boldsymbol{r}\,'}{|\boldsymbol{r} - \boldsymbol{r}\,'|} \,. \tag{4.23}$$

The z-component, which is relevant for the AFM signal, reads

$$F_z(\boldsymbol{r}) = \frac{-2eq_{\mathrm{tip}}}{4\pi\epsilon_0\epsilon} \sum_{n,l}^{N} \int_0^R d\rho' \int_0^{2\pi} d\phi' \, \frac{\tilde{\sigma}(\rho', \phi')\rho' z}{|\rho^2 + \rho'^2 + z^2 - 2\rho\rho' \cos(\phi - \phi')|^{3/2}},$$

where the integral over z' is already evaluated. The ϕ independence of the charge density ($|\exp(il\phi')| = 1$) and the permittivity ϵ of vaccum ($\epsilon = 1$) simplifies F_z to

$$F_z(r, \phi = 0, z) = \frac{-2eq_{\mathrm{tip}} z}{4\pi\epsilon_0} \sum_{n,l}^{N} \int_0^R d\rho' \rho' \left| c J_l\left(k_{n,l}\, \rho'\right)\right|^2 \int_0^{2\pi} d\phi' \frac{1}{|\rho^2 + \rho'^2 + z^2 - 2\rho\rho' \cos(\phi')|^{3/2}} \,. \tag{4.24}$$

The positive denominator in Eq. (4.24) for $\{\rho, \rho', z\} \in \mathcal{R}_0^+$ and $\phi' \in [0, 2\pi]$ gives rise to an expression in terms of the elliptic integral

$$\mathcal{E}(\rho) = \mathcal{E}(\pi/2, \rho) := \int_0^{\pi/2} \sqrt{1 - \rho \sin^2(\theta)} d\theta$$

resulting in

$$\int_0^{2\pi} d\phi' \frac{1}{|\rho^2 + \rho'^2 + z^2 - 2\rho\rho' \cos(\phi')|^{3/2}} = \frac{2}{\rho^4 + 2\rho^2(z^2 - \rho'^2) + (\rho'^2 + z^2)^2} \times \left[\sqrt{(\rho - \rho')^2 + z^2}\mathcal{E}\left(-\frac{4\rho\rho'}{(\rho - \rho')^2 + z^2}\right) + \sqrt{(\rho + \rho')^2 + z^2}\mathcal{E}\left(\frac{4\rho\rho'}{(\rho + \rho')^2 + z^2}\right)\right].$$

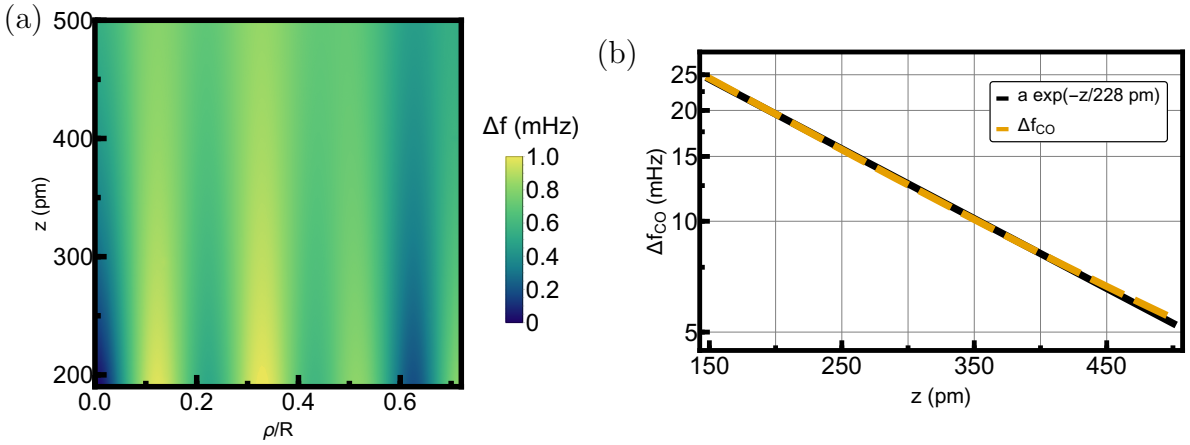

Figure 4.11: The Coulomb interaction between the charge density $\tilde{\sigma}$ and the tip is reducing the frequency of the AFM cantilever. The z-dependency of the contrast Δf_{CO} obeys an exponential law. (a) shows the radial dependence of the two-dimensional charge density $\tilde{\sigma}$ with a period in ρ-direction of approximately $0.25R = 1.7$ nm. (b) shows the contrast (orange) defined in Eq. (4.18) and an exponential fit (black) by $ae^{-z/b}$ with $a = (46 \pm 0.14)$ mHz and $b = (228 \pm 5.8 \cdot 10^{-5})$ pm.

Finally, the frequency shift Δf of the AFM cantilever at position $\boldsymbol{r}$ results from the z-direction of the Coulomb force through [121]

$$\Delta f(\rho, \phi = 0, z) = -\frac{f_0}{k\pi A^2} \int_{-A}^{A} \frac{F_z(\rho, \phi = 0, z - q)\, q}{\sqrt{A^2 - q^2}} dq. \tag{4.25}$$

Both, the integrals over ρ' in Eq. (4.24) and over q in Eq. (4.25) must be evaluated numerically. The AFM sensor has a cantilever stiffness of $k = 1800\mathrm{N/m}$, an oscillation amplitude of $A = 50$ pm and an oscillation frequency of $f_0 = 20.4$ kHz. The numerical solution of Eq. (4.25) for a CO terminated tip is plotted in Fig. 4.11. For a repulsive force, the frequency shift is negative as expected and undulates with changing ρ in the same manner as the charge density for small distances z. These oscillations smear out for rising sample-tip distance. When approaching the boundary $\rho = R$ the charge density outside of the quantum corral gets relevant. Due to the neglection of these charges, the frequency shift in that area is not physically relevant and is therefore not plotted. In Fig. 4.11(b) a fitting of $ae^{-z/b}$ on the contrast Δf_{CO} illustrates a decay rate $b \approx 228$ pm. This is in consensus with an elementary electrostatic estimation [146]: An oscillating charge density with a period $\lambda_F/2 = 1.6$ pm yields an approximated exponential decay rate of $\lambda_F/(4\pi) = 255$ pm with the Fermi wavelength is given by $\lambda_F = 2\pi\hbar/\sqrt{2m^* 440\ \mathrm{meV}} \approx 3$ nm. Certainly, b is more than one order of magnitude bigger than the experimental achieved value of $\lambda_{\mathrm{Cu}} = 55.7$ pm.

Two effects, which influence the electrostatics, need to be discussed. The Cu (111) bulk is not charged, therefore a compensating charge density exists below the surface. The distance of these two charge density layers d can be estimated by 15% of the Cu

bulk Fermi wavelength of 73 pm [147, 148]. Also for the second layer, with a shifted charge density by $d = 11$ pm, is the decay rate of 228 pm a good approximation. The summation of forces arising from the two layers yields still a frequency shift decreasing exponentially with $b \approx 228$ pm. A surface dipole layer thus is not affecting the decay ratio. Secondly, in case of a metallic tip only the tip charge is different. According to that, only the magnitude will be modified by a factor of $q_{\mathrm{Cu}}/q_{\mathrm{CO}} \approx -0.23$ and the decay length is unaffected.

It can be therefore concluded, even without discussing the magnitudes of the occurring force, that the quasi-classical model, using a quantum mechanical charge density and a classical Coulomb force description, does not explain the experimental achieved contrasts Δf_{Cu} and Δf_{CO}.

As already pointed out, when the sample-tip distance is reduced, the importance of chemical bonding increases. Therefore the next step would be a model to describe the chemical bonding between the surface states and the tip orbitals.

4.5.2. Description by LCAO method: An outlook

Four characteristics gained by the experiments are of major importance for a chemical bonding description. First, the force decays exponentially in orders of 50 pm and second the energy of the state in proximity to E_F for a metallic tip distance of $z = 440$ pm gets shifted to $E_{5,0} - 0.8$ meV. Third, all quantum corral states are contributing to this force and finally fourth, the force is attractive (repulsive) for the metallic (CO) tip. To start with a linear combination of atomic orbitals (LCAO) method for describing these effects, we will concentrate on the metallic tip here. From Ref. [149] it is known that the metallic tip in our relevant energy regime is mostly dominated by the s-orbital. This simplification is critical for the CO terminated tip where also p-like orbitals come into play. So we will not make any predictions for the CO terminated tip yet. The observation that all quantum corral states contribute to the force is an open question which we want to discuss here shortly. In molecule physics the chemical bonding between two atoms is initialized and caused by electrons of valence shells. If this shells are fully occupied and therefore called closed shell, the chemical reactivity is dramatically reduced (e.g. for noble gases). Open valence shells on the other hand are reactive and enable chemical bonding. The valence shell is thereby defined by the outermost shell [150]. In the artificial atom called quantum corral, we know from sec. 4.3.2 that all states are decaying in the relevant z-direction with the same decay length λ_z. So the valence shell consists of all $\psi_{n,l}$. In contrast to atoms, where the outermost orbitals typically correspond to the highest energies, the outermost quantum corral orbital's energies range from -440 meV to $E_F = 0$. And this is then influencing the occupation of each orbital. The orbitals with less energy are fully occupied, meanwhile the orbitals around Fermi energy are partially filled. The reactivity is therefore low for orbitals far away from E_F and high for orbitals around E_F. Now a contradiction arises: According to the valence shell argument, all orbitals $\psi_{n,l}$ contribute to the chemical bond, and thus give a frequency shift depending on the total charge density $\tilde{\sigma}$ as displayed in Fig. 4.9. The argument about the occupation rate is however suggesting a frequency shift depending

on the charge density around E_F in analogy to σ_{Fermi} from sec. 4.3.3. In a typical atom, the outermost orbitals also have the highest energy, so this problem does not appear. To clear this contradiction is one goal we want to achieve in the future by applying LCAO method. Now we want to link the first two force characteristics listed above to the LCAO method. To do so we will first capture the main information about this method. The huge scales which appear in the quantum corral setup, from single atomic tips to mesoscopic standing wave patterns with diameters of 14 nm, makes the application of DFT computationally very challenging. The LCAO method uses the atomic orbital ψ_i as basis functions to represent the accruing molecule orbitals χ_j. This implies that the molecule orbitals can be written as a linear superposition of the atomic orbitals. A variety of other basis functions, e.g. Slater or Gaussian-type, are known and common. The reason of choosing LCAO is firstly the knowledge about the analytical form of the atomic orbitals and secondly the advantage of a qualitative and intuitive picture. For detailed information about the basics of the LCAO method we refer to Ref. [151, 152]. The investigation of the LCAO method for chemical bonds between an artificial atom and an atomic tip orbital is still under development [153]. Here we will just sketch the functional dependence of the molecule orbitals by the atomic orbital overlaps where just two atomic orbitals are involved. The two orbitals we will consider here are the quantum corral eigenstate $\psi_1(\boldsymbol{r}) = \psi_{n,l}(\boldsymbol{r})$ with $(n, l) = (5, 0)$ (which has am eigenenergy $E_1 \approx E_F$) and a 1s-like orbital of a Cu terminated tip $\psi_2(\boldsymbol{r}, \boldsymbol{r}_{\text{tip}}) \propto \exp\left(\frac{-|\boldsymbol{r}-\boldsymbol{r}_{\text{tip}}|}{\beta_{\text{tip}}}\right)$ with the same eigenenergie $E_2 = E_1$. The tip orbital is centered around the tip position $\boldsymbol{r}_{\text{tip}}$. Similar to the decay length of the quantum corral state with $\frac{1}{\kappa} = 84.2$ pm known from sec. 4.3.2, β_{tip} is approximated by

$$\beta_{\text{tip}} = \sqrt{\frac{\hbar^2}{2m_e\Phi_0}} = 87.8 \text{ pm}. \tag{4.26}$$

The molecule orbitals are represented by a superposition of atomic orbitals,

$$\chi_i(\boldsymbol{r}) = c_{i,1}\,\psi_{5,0}(\boldsymbol{r}) + c_{i,2}\,\psi_2(\boldsymbol{r}) \qquad \forall i \in \{1, 2\}. \tag{4.27}$$

By using the variational theorem, the $c_{i,j}$ coefficients are varied such that the energies of the molecule orbital e_i are minimized [151]:

$$e_i = \frac{\langle\chi_i|H_{\text{eff}}|\chi_i\rangle}{\langle\chi_i|\chi_i\rangle}. \tag{4.28}$$

The effective single-particle Hamiltonian H_{eff} is built by taking the potential of both atoms into account. If $H_{1,1} = H_{2,2}$ is given, the theorem yields

$$\begin{aligned} e_1 &= \frac{H_{1,1} + H_{1,2}}{1 + \gamma_{1,2}}, \\ e_2 &= \frac{H_{1,1} - H_{1,2}}{1 - \gamma_{1,2}}, \end{aligned} \tag{4.29}$$

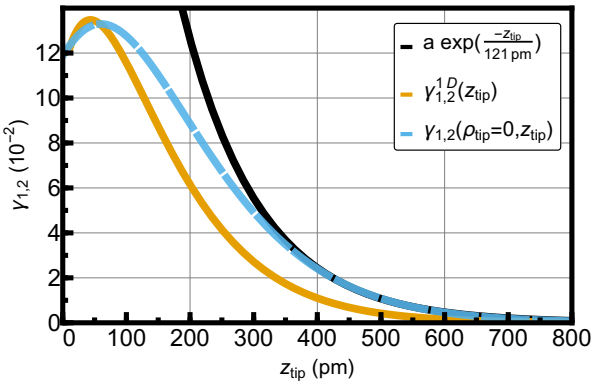

Figure 4.12: The overlap $\gamma_{1,2}$ for the quantum corral eigenstate with $(n,l) = (5,0)$, having a decay length of $\frac{1}{\kappa} = 84.2$ pm, and a 1s-orbital of the Cu terminated tip with $\beta_{\text{tip}} = 87.8$ pm, is illustrated (blue). The tip is for this purpose centered above the quantum corral ($\rho_{\text{tip}} = \phi_{\text{tip}} = 0$) and approaching the surface step wise. The fit of an exponential function $ae^{-z/\eta}$ (black) results in a decay length of $\eta = (121.49 \pm 0.18)$ pm. The validity of the model is given for $z \gtrapprox \beta_{\text{tip}}$. Additionally the overlap of two exponential functions, Eq. (4.31) (orange) are displayed for comparing reasons.

where e_1 and e_2 are the energies of the (anti-)bonding molecule orbital in a single-particle description. Here $H_{i,i'}$ is defined by $H_{i,i'} = \langle\psi_i|H_{\text{eff}}|\psi_{i'}\rangle$ and the overlap $\gamma_{1,2}$ by

$$\gamma_{1,2}(\boldsymbol{r}_{\text{tip}}) = \langle\psi_1(\boldsymbol{r})|\psi_2(\boldsymbol{r},\boldsymbol{r}_{\text{tip}})\rangle. \tag{4.30}$$

Eq. (4.29) shows the direct dependence of the single-particle molecule energies from $\gamma_{1,2}$ and an indirect one in $H_{i,i'}$. The sample-tip distance dependency is included in $H_{i,i'}$ and $\gamma_{1,2}$.

The analysis of the matrix elements $H_{i,i'}$ is still under current investigation [153]. We will now concentrate on the overlap $\gamma_{1,2}$, which we solve numerically. The solution of the three-dimensional integral of the overlap $\gamma_{1,2}$ for a tip position of $\rho_{\text{tip}} = 0, \phi_{\text{tip}} = 0$ and varying z_{tip} is illustrated in Fig. 4.12 in blue. With decreasing distance between the tip orbital and the quantum corral eigenstate, the overlap is increasing. Beyond a value of around $z = 87.8$ pm $= \beta_{\text{tip}}$, a relevant part of the tip orbital is located at $z \leq 0$ pm but the quantum corral eigenstates are only defined for $z \geq 0$ pm. Therefore the model is not applicable any more for $z \lesssim \beta_{\text{tip}}$. The z range of interest is $z \in [450, 600]$ pm given by the experiment shown in Fig.4.10(a). An exponential fit $\propto e^{-z_{\text{tip}}/\eta}$ to the overlap in this z-regime is displayed in black and yields $\eta = 121$ pm, a value more than a factor of two bigger than the experimental decay length of the contrast Δf_{Cu}. To confirm the principle behavior of $\gamma_{1,2}$ we also solve the overlap integral analytically for two one-dimensional

exponential functions, $\psi^{1D}_{\text{surf}}(z) \propto e^{-z/\lambda_z}$ and $\psi^{1D}_{\text{tip}}(z, z_{\text{tip}}) \propto e^{-|z_{\text{tip}}-z|/\beta_{\text{tip}}}$:

$$\begin{aligned}\gamma^{\text{1D}}_{1,2} &= \int_0^\infty dz\, \psi^{1D}_{\text{surf}}(z)\, \psi^{1D}_{\text{tip}}(z, z_{\text{tip}}) \\ &\propto \int_0^\infty dz\, e^{-z/\lambda_z} e^{-|z_{\text{tip}}-z|/\beta_{\text{tip}}} \\ &\propto \begin{cases} \frac{\lambda_z \beta_{\text{tip}}}{\lambda_z - \beta_{\text{tip}}} \left(e^{-z_{\text{tip}}/\lambda_z} - e^{-z_{\text{tip}}/\beta_{\text{tip}}}\right) + \frac{\lambda_z \beta_{\text{tip}}}{\lambda_z + \beta_{\text{tip}}} e^{-z_{\text{tip}}/\beta_{\text{tip}}} & \text{for } \lambda_z \neq \beta_{\text{tip}} \\ \left(\frac{\lambda_z}{2} + z_{\text{tip}}\right) e^{-z/\lambda_z} & \text{for } \lambda_z = \beta_{\text{tip}}. \end{cases}\end{aligned} \tag{4.31}$$

When adjusting the maximum of $\gamma^{\text{1D}}_{1,2}$ to $\gamma_{1,2}$, Eq. (4.31) shows a similar trend as the 3D overlap $\gamma_{1,2}$. In the 1D overlap we see that only in the limit $z_{\text{tip}} \gg \lambda_z, \beta_{\text{tip}}$ the overlap is following an exponential law with a decay rate of β_{tip}. Therefore it seems reasonable to have a decay length $\eta = 121\text{pm}$ bigger than the involved decay lengths β_{tip} and λ_z for $z \in [450, 600]$ pm. Of course the frequency shift resulting from bonding has a complex dependency on $\gamma_{1,2}$ and therefore needs more intensive studies.
This is the first step for a chemical bonding description by usage of the LCAO method of a 1s-orbital to an orbital generated by the artificial atom called quantum corral. The next step will be the calculation of single-particle molecule orbital eigenenergies $e_{1/2}$. The bonding molecule energy e_1 of the $\psi_{5,0}$ can than be compared to the experimentally achieved perturbed eigenenergy of Eq. (4.21),

$$e_1 \approx E_{5,0} - \Delta E_{(5,0),\text{Cu}} = -1.12 \text{ meV} \tag{4.32}$$

below E_F. In the future several aspects are important: From Fig. 4.9 we know that the experimental frequency shift of the Cu terminated tip is sensitive to the total charge density. So in principle all quantum corral states should be included. For that more detailed information about the involved tip orbitals for the energy regime of $[-440, 0]$ meV is required. The complexity is raised even higher when including Coulomb interaction and the spins of individual electrons. In principle the many-body ground state offers then valuable clues on the bonding force given by the derivative of the many-body groundstate with respect to the sample-tip distance. Finally by Eq. (4.25) the appearing frequency shift resulting from chemical bonding can be calculated.

4.6. Summary and outline

In the quantum corral chapter we investigated several theoretical aspects of the experimental STM and AFM results published in our manuscript [51]. To begin with we concentrated on the STM measurements, where we analytically solved the single-particle hard wall model in three dimensions. In case of a quantum corral constructed by Fe atoms, this model is sufficient and gives an intuitive picture of the arising LDOS. When the quantum corral is perturbed by an additional iron atom positioned in the circular form, the hard wall model is not applicable any more. From previous studies we knew that the scattering phase is a crucial factor influencing the LDOS and therefore also

the measured topographic STM image. We established a new tight-binding model to simulate the standing wave pattern. For a circular potential well we first found a regime of the potential strength such that the correct scattering phase of one individual Fe adatom is expected. A more detailed adjustment of this strength gave a convincing agreement of the numerical LDOS and the topographic STM measurement. With that the tight-binding model was ready to be tested for the quantum corral made of 48 Fe adatoms. We found persuasive agreement to the experiment for the quantum corral without an adatom and for five adatom positions. Even more, the first radial maximum of the LDOS arising from a corral with a Fe atom at the center exhibited a hexagonal structure. This structure is directly governed by the detailed geometrical setting of the adatom positions, which is itself constrained by the underlying Cu (111) symmetry. Therefore this model describes the measured STM data in plenty of different configurations. We did not show the data, but the same model can be used for quantum corrals made of CO molecules, where only the potential strength of the circular well has to be adjusted. This model is thus a powerful tool to describe the standing wave pattern. In the future we want to extend this model by allowing also complex scattering phases to appear. A complex scattering phase is not only generating a specific standing wave pattern but also includes absorption effects at the adatom positions and can therefore describe the life times of the quantum corral states [132]. We plan to realize the complex scattering phase by a pure imaginary, infinite self-energy coupling to the 2D discretized Hamiltonian [68]. This would lead to different possible investigations, ranging from the level broadening effects due to absorbing channels to influences of the STM tip itself while measuring. As pointed out, the quantum corral formed by Fe atoms, similarly to the CO formed one, is too leaky to produce ergodic or even chaotic behavior. Replacing the Cu substrate by graphene or a topological insulator gives more promising candidates for achieving chaos in quantum corrals. To describe the arising patterns in these setups, our developed model can be customized.

Another main focus was the theoretical analysis of the AFM quantum corral measurements. The experiments displayed forces which strongly decay with increasing distance between the quantum corral surface states and the tip. Depending on the tip type, either Cu or CO terminated, the acting force is attractive or repulsive, but both tips experience forces depending on the total charge density of the quantum corral. To exclude a pure electrostatic effect, we numerically computed the frequency shift arising from a Coulomb force of a two-dimensional surface charge acting on the point-like AFM tip. The significant discrepancy between the decay length achieved by this force and the measured one, exclude the Coulomb force as the major influencing factor. The presumption of chemical bonding between the mesoscopic standing wave of the artificial atom and the tip orbitals got fortified. To describe a bonding we chose the LCAO model. First we argued that a contradiction appears when supposing that only not fully occupied orbitals contribute to the bonding. The appearing force would be dependent on the local density of states around Fermi energy and not on the total density as measured in the experiment. Due to the universal decay length in z-direction, the valence shell is specified by all corral orbitals such that this can be reasoning the observed dependency. A first step to a LCAO description was done by computing the overlap of one surface

state to a 1s-orbital like function of the metallic tip. The achieved overlap exhibits a decay length greater than the experimental values. However, the molecule orbital energies are also functional depended on other parameter, such that an final statement of the agreement between LCAO and experiment is not possible. The presumed chemical bonding between orbitals of the artificial atom and the AFM tip is an interesting field of research and certainly worth to study.

5. Conclusion

At the end of this thesis, a summary of the achieved results and possible perspectives for further developments is given. For a more detailed summary we refer to the end of each chapter.
The main focus of this thesis was the development of energy-dependent S-matrix correlations in (non-)trivial TIs responsible for an expected universal signature of indistinguishability expressed in the Hong-Ou-Mandel (HOM) effect in electron quantum optics (EQO). For this purpose we started in chapter 1 to link these objects to the HOM probability of detecting both electrons at the same exit. The development of a semiclassical approximation of energy-dependent four-point correlators was an important building block. Semiclassical, the S-matrix is approximated by a sum of trajectories fulfilling the classical equations of motion. The action difference of distinct trajectories that typically appears when calculating transport properties gives rise to a highly oscillating phase, such that only action differences in orders of $\hbar$ contribute after averaging. For identical trajectories with vanishing action difference this yields the first order contribution in inverse number of open modes N. More accurate description is available when also considering trajectory pairs (for two-point correlators) or quadruplets (for four-point correlators) with action differences in orders of $\hbar$. This appears in the so-called encounter regions, while on the other hand the action difference vanishes in the links. The one-to-one correspondence between closed orbit pairs and the trajectory pairs enables to formulate a closed form for energy-dependent two-point correlators. For quadruplets, however this simplification is not applicable anymore, as it can be presented in the following way: In case of one pair, both trajectories are always passing each link and each encounter. For quadruplets trajectories can intersect in an encounter, however not all four trajectories have to pass this encounter and/or pass an link. This freedom is challenging and forced us to compute step wise for each quadruplet the effective contribution. The huge amount of possible quadruplets and the canceling effect is computationally costly, and only for energy independent moments of the transmission a reduction is known. We were able to predict an infinite series for vanishing energy difference and proofed the convergence to a finite limit, such that the studied four-point correlators coincide with random matrix theory (RMT) predictions for COE and CUE. In the presence of time-reversal symmetry two correlators ($C^{=}(\Delta)$ and $D^{x}(\Delta)$) share the property of alternating signs for each contributing order in $1/N$, an effect that dominates for low number of open modes. The absence of time-reversal symmetry results in no alternating signs and therefore correlators converging faster. This analytical investigation is supported by numerical tight-binding simulations in 2DEGs.
In this context, we first introduced methods to compute the mean free path for Anderson disorder. Afterwards the first system consisting of two leads intersected by a disordered

cavity with smooth boundaries is implemented. The statistic of S-matrix elements is in accordance with a bivariate Gaussian. An upgraded setup with undulating boundaries yields clear and explicit correlator forms coinciding perfectly with the semiclassic treatment. Afterwards, reaching the low number of open modes regime gives new insights: The numerical result builds the backbone to investigate the semiclassical convergence properties. For $N = 4$, drastic oscillations of the analytical approaches are present, nevertheless taking only odd number of terms gives reasonable and convincing agreement to numerics. Thus the semiclassical approach is even reliable at the edge of validity, when convergence issues appear. Thanks to an collaboration, further approaches of studying S-matrix correlators were available, namely an experimental realization in microwave billiards and the numerical investigation using the Heidelberg approach. This complete range of methods is in agreement and build the basis for investigations in non-trivial TIs.
To address the task of S-matrix correlations in TIs, we start with solving the corresponding Schrödinger equation for a 2D waveguide using the Bernevig-Hughes-Zhang (BHZ) Hamiltonian. The result enables us to adjust the tight-binding setup, such that correlations between S-matrices at different energies are trustful and no spurious phases are occurring. In the next step we adjusted and extended the electron coherence formalism for energy-dependent S-matrices. Thereby we are able to predict the experimentally accessible current current correlation in terms of the S-matrix correlators. The Hanbury-Brown-Twist (HBT) contributions originate from interferences of one wavepacket with the Fermi Sea and can be separated from the HOM type $\Delta\bar{Q}_{\mathrm{HOM}}$. Furthermore the resulting formalism enables to study temperature dependent phenomena in this context, too. For the implementation of a billiard-shaped system, first only one spin block of the BHZ Hamiltonian is considered that breaks time-reversal symmetry. In consistency with RMT the statistic of S-matrix elements are given by CUE. The correlators of interest share in principle the same form as done in 2DEG systems, however reduced widths (corresponding to increased dwell times) are observable, most likely due to mode mismatches at the interface lead-cavity. Introducing spin-orbit coupling gives rise to the time-reversal symmetry with $\mathcal{T}^2 = -1$ and S-matrix elements expecting to obey CSE. However the scattering at the interface is dominant, such that the fidelity to CSE is not fulfilled. The main dependency of $\Delta\bar{Q}_{\mathrm{HOM}}$ is given by the four-point correlator $D^x(\Delta)$, itself aquiring a delta-like form. If the widths of the incoming wavepackets are not adapted, the current current correlation is therefore almost independent on the time delay and the shape of both wavepackets entering the setup. The experimental realization of chaotic cavities using TIs is certainly one key aspect to consider in the future. On the other hand theoretical investigations are necessary to improve the understanding of interface scattering and pure chaotic scattering in the cavity.

Contrary to EQO, there is a disposability of experiments when considering the quantum corral. Plenty of experiments are known and one, preforming first AFM measurements on this setup gave the motivation to our investigations in this field. First we introduced the quantum corral and explained the experimental basics of AFM and STM measurements, following by the use of the first theoretical model, the hard wall model for the standing

wave pattern in the local density of states. The success of this model for STM measurements is already known, however the novel data included STM measurements on quantum corrals perturbed by an additional iron adatom inside the circular form. The failure of the hard wall model in this context enforced us to investigate more deeply. The scattering phase adaption of our tight-binding model to the experimentally available data results in first numerical model successfully describing the standing wave pattern for all adatom positions that were measured. In addition we were able to ascribe the sixfold symmetry of the maxima to the subjacent Cu symmetry, however this effect is not applicable in general as verified by our investigations. At the end we concentrated on the AFM measurement, which experiences a contrast of the frequency shift exponentially decaying with the sample-tip distance. For the metallic and the CO terminated tip, the frequency shift is proportional to the total charge density from by the hard wall model. We computed the classical Coulomb interaction between the charge density in the quantum corral and the charged tip, yielding a decay length almost five times larger than the one measured by AFM. We excluded therefore the electrostatic interaction being the reason of the small decay length measured. In the next step we introduced the linear combination of atomic orbitals (LCAO) method to compute the chemical bonding between the mesoscopic standing waves of the quantum corral and the strongly localized tip. As an first contribution, the orbital overlap of the 1s-like metallic tip orbital and the highest occupied quantum corral state was computed. The decay length of the orbital overlap is at least twice the experimental decay length, however several more physical dependencies need to be included. The development of a model describing the chemical bonding between the mesoscopic charge density and the point-like tip using LCAO is scheduled for future works.

A. First appendix: correlations in trivial TIs

A.1. Convergence of the four-point correlators for vanishing energy difference

In subsec. 2.2.5 we provide for the orthogonal case a series for $D^x(\Delta = 0)$ and $C^=(\Delta = 0) = B^=(\Delta = 0)$ by Eqs. (2.48), (2.50). Here we will reformulate this recursive series of $\mathcal{F}_i$ and $\mathcal{G}_i$ in a closed form, such that the convergence of the correlators to RMT for $\Delta = 0$ is explicit. To start with we repeat the definition of $\mathcal{F}_i$:

$$\mathcal{F}_i = 3\mathcal{F}_{i-1} + 1, \qquad \text{with } \mathcal{F}_0 = 0.$$

With induction one can prove

$$\begin{aligned}\mathcal{F}_i - \mathcal{F}_{i-1} &= 3\mathcal{F}_{i-1} + 1 - \mathcal{F}_{i-1} \\ &= 2\mathcal{F}_{i-1} + 1 \\ &= 2(3\mathcal{F}_{i-2} + 1) + 1 \\ &= \cdots = 1 + \sum_{j=0}^{i-2} 2 \cdot 3^j,\end{aligned}$$

such that

$$\begin{aligned}\mathcal{F}_i - \mathcal{F}_0 = \mathcal{F}_i &= \sum_{k=1}^{i} \mathcal{F}_k - \mathcal{F}_{k-1} \\ &= \sum_{k=1}^{i} \left(1 + \sum_{j=0}^{k-2} 2 \cdot 3^j\right) = \frac{1}{2}(3^i - 1).\end{aligned}$$

This closed form for the factors $\mathcal{F}_i$ enables us to conclude the consensus to RMT:

$$\begin{aligned}D^x(\Delta = 0) &= \sum_{i=1}^{\infty} (-1)^i \frac{\mathcal{F}_i}{N^{i+2}} \\ &= \sum_{i=1}^{\infty} (-1)^i \frac{3^i - 1}{2N^{i+2}} \\ &= -\frac{1}{N(N+1)(N+3)}.\end{aligned} \tag{A.1}$$

For $B^{=}(0) = C^{=}(0)$, we know the factors $\mathcal{G}_i$ are defined by

$$\mathcal{G}_i = 3\mathcal{G}_{i-1} - 1; \qquad \text{with } \mathcal{G}_0 = 1.$$

We rewrite these as

$$\begin{aligned} &\mathcal{G}_i = \mathcal{F}_i + 1 \\ &\Rightarrow\ \mathcal{G}_i - \mathcal{G}_{i-1} = \mathcal{F}_i - \mathcal{F}_{i-1} = 1 + \sum_{j=0}^{i-2} 2 \cdot 3^j, \end{aligned}$$

which yields

$$\mathcal{G}_i = \frac{1}{2}(3^i - 1) + 1 = \frac{1}{2}(3^i + 1).$$

Then the series is given by

$$\begin{aligned} B^{=}(0) = C^{=}(0) &= \sum_{i=1}^{\infty} (-1)^i \frac{\mathcal{G}_i}{N^{i+2}} \\ &= \sum_{i=1}^{\infty} (-1)^i \frac{3^i + 1}{2N^{i+2}} \\ &= \frac{N+2}{N(N+1)(N+3)}, \end{aligned} \tag{A.2}$$

again in agreement to RMT predictions.

B. Second appendix: correlations in TIs

B.1. Detailed analysis of current-current correlation

B.1.1. Computing $Q(t,t')$

In this section we provide the detailed calculation to achieve Eq. (3.30) mostly following Ref. [92,104,105], but without assuming energy-independent S-matrices and expand the number of open modes to $N = 4$. Here we use the notation $\langle \dots \rangle$ for the expectation value with respect to $|\phi_i\rangle$ and $\langle \dots \rangle_\mu$ relating to the Fermi sea $|F\rangle_\mu$. Starting with $\hat{I}_{\tilde{3}}(t)$ in Eq. (3.22) we evaluate $\langle \hat{I}_{\tilde{3}}(t) \rangle$:

$$\hat{I}_{\tilde{3}}(t) = -ev \sum_{i}^{4} \hat{\Psi}^\dagger_{\tilde{3},i}(t)\hat{\Psi}_{\tilde{3},i}(t) - ev \sum_{\substack{i,j=1 \\ j\neq 1}}^{4} \hat{\Psi}^\dagger_{\tilde{3},i}(t)\hat{\Psi}_{\tilde{3},j}(t) \tag{B.1}$$

$$\Rightarrow -\frac{1}{ev}\langle \hat{I}_{\tilde{3}}(t) \rangle = \sum_{i=1}^{4} \langle \hat{\Psi}^\dagger_{\tilde{3},i}(t)\hat{\Psi}_{\tilde{3},i}(t) \rangle \tag{B.2}$$

while using the orthogonality of many-body states[1],

$$\begin{aligned}
&\langle \hat{\Psi}^\dagger_{\tilde{3},i}(t)\hat{\Psi}_{\tilde{3},j}(t) \rangle = \\
&\quad = \frac{1}{hv} \int dE dE'\, d\epsilon d\epsilon'\, e^{i\frac{t}{\hbar}(\epsilon-\epsilon')}\, S^*_{3,1}(\epsilon')S_{3,2}(\epsilon) \Big\langle \hat{a}_1(E')\hat{a}^\dagger_i(\epsilon')\hat{a}_j(\epsilon)\hat{a}^\dagger_1(E) \Big\rangle_\mu \\
&\quad = \frac{-1}{hv} \int dE dE'\, d\epsilon d\epsilon'\, e^{i\frac{t}{\hbar}(\epsilon-\epsilon')}\, S^*_{3,1}(\epsilon')S_{3,2}(\epsilon) \Big\langle F|\hat{a}_1(E')\hat{a}_j(\epsilon)\hat{a}^\dagger_i(\epsilon')\hat{a}^\dagger_1(E)|F \Big\rangle_\mu \\
&\quad \overset{i\neq j}{=} 0
\end{aligned} \tag{B.3}$$

and the commutator relation in Eq. (3.15). Analogue to Eqs. (B.1), (B.2) the quantities $\hat{I}_4(t)$ and $\langle \hat{I}_4 \rangle$ can be computed. Evaluating the current-current correlation $\sigma_{(\tilde{3},\tilde{4})}(t,t')$ by using the definitions

$$\hat{I}_{\tilde{j},i}(t) = -ev\, \hat{\Psi}^\dagger_{\tilde{j},i}(t)\hat{\Psi}_{\tilde{j},i}(t)$$
$$\sigma_{(\tilde{3},\tilde{4}),(i,j)}(t,t') = \Big\langle \delta\hat{I}_{\tilde{3},i}(t)\, \delta\hat{I}_{\tilde{4},j}(t') \Big\rangle$$

[1] This is visible by the uneven numbers of $\hat{a}_i$ and $\hat{a}^\dagger_i$. The choice of evaluating with respect to $|\phi_1\rangle$ or $|\phi_2\rangle$ is thereby irrelevant.

yields

$$\begin{aligned}\frac{1}{e^2v^2}\sigma_{(\tilde{3},\tilde{4})}(t,t') &= \sum_{i,j=1}^{4}\sigma_{(\tilde{3},\tilde{4}),(i,j)}(t,t') \\ &\quad + \underbrace{\sum_{\substack{i,j=1\\ j\neq i}}^{4}\sum_{\substack{i',j'=1\\ j'\neq i'}}^{4}\left\langle \hat{\Psi}^{\dagger}_{\tilde{3},i}(t)\hat{\Psi}_{\tilde{3},j}(t)\hat{\Psi}^{\dagger}_{\tilde{4},i'}(t')\hat{\Psi}_{\tilde{4},j'}(t')\right\rangle}_{=Q(t,t')}, \\ Q(t,t') &= \sum_{\substack{i,j=1\\ j\neq i}}^{4}\left\langle \hat{\Psi}^{\dagger}_{\tilde{3},i}(t)\hat{\Psi}_{\tilde{3},j}(t)\hat{\Psi}^{\dagger}_{\tilde{4},j}(t')\hat{\Psi}_{\tilde{4},i}(t')\right\rangle\end{aligned} \tag{B.4}$$

With the same argument as in Eq. (B.3) in $Q(t,t')$ only summands fulfilling $i = j' \wedge j = i'$ are not zero.

B.1.2. Separating HOM from HBT correlations

By applying Wicks theorem the remaining summands can be rewritten [154, 155][2]:

$$Q(t,t') = \sum_{\substack{i,j=1\\ j\neq i}}^{4} G^{e}_{(\tilde{3},\tilde{4}),i}(t',t)G^{h}_{(\tilde{3},\tilde{4}),j}(t',t), \tag{B.5}$$

with

$$\begin{aligned}G^{e}_{(\tilde{3},\tilde{4}),i}(t',t) &= \left\langle \hat{\Psi}^{\dagger}_{\tilde{3},i}(t)\hat{\Psi}_{\tilde{4},i}(t')\right\rangle, \\ G^{h}_{(\tilde{3},\tilde{4}),i}(t',t) &= \left\langle \hat{\Psi}_{\tilde{3},i}(t)\hat{\Psi}^{\dagger}_{\tilde{4},i}(t')\right\rangle.\end{aligned}$$

Each coherence function can be reformulated [92],

$$\begin{aligned}G^{e}_{(\tilde{3},\tilde{4}),i}(t',t) &= \Delta G^{e}_{(\tilde{3},\tilde{4}),i}(t',t) + G^{e}_{\mu,(\tilde{3},\tilde{4}),i}(t',t), \\ G^{h}_{(\tilde{3},\tilde{4}),i}(t',t) &= -\Delta G^{e^*}_{(\tilde{3},\tilde{4}),i}(t',t) + G^{h}_{\mu,(\tilde{3},\tilde{4}),i}(t',t)\end{aligned} \tag{B.6}$$

with

$$\begin{aligned}G^{e}_{\mu,(\tilde{3},\tilde{4}),i}(t',t) &= \frac{1}{hv}\int d\epsilon\, e^{i\frac{\epsilon(t'-t)}{\hbar}} S^{*}_{\tilde{3},i}(\epsilon)S_{\tilde{4},i}(\epsilon)\, f_{\mu}(\epsilon), \\ G^{h}_{\mu,(\tilde{3},\tilde{4}),i}(t',t) &= \frac{1}{hv}\int d\epsilon\, e^{i\frac{\epsilon(t-t')}{\hbar}} S^{*}_{\tilde{4},i}(\epsilon)S_{\tilde{3},i}(\epsilon)\,(1-f_{\mu}(\epsilon))\end{aligned}$$

[2] It is not obvious that it applies for the non-equilibrium states used here. We recommend Ref. [91] appendix C for detailed information about the application in this formalism.

for $i \in [1,4]$ and

$$\Delta G^{e}_{(\tilde{3},\tilde{4}),i}(t',t) = \begin{cases} \int dE dE'\, \phi_i^*(E')\phi_i(E)\, e^{\frac{i}{\hbar}(E't'-Et)} S^*_{\tilde{3},i}(E') S_{\tilde{4},i}(E) & \text{for } i \in \{1,2\} \\ 0 & \text{for } i \in \{3,4\}. \end{cases} \tag{B.7}$$

Here we used the fact that our wavepackets are entering the system in $i = 1$ and $i = 2$. We further assume that the wavepacket excitation is far apart from the Fermi sea with Fermi-Dirac statistic $f_\mu(\epsilon)$ at zero temperature, $\int d\epsilon\, f(\epsilon)\phi(\epsilon) \approx 0$. Inserting Eq. (B.6) into (B.5) we have access to $\Delta Q(t,t')$ given by

$$\begin{aligned} Q(t,t') &= \Delta Q(t,t') + \sum_{\substack{i,j=1 \\ j\neq i}}^{4} G^{e}_{\mu,(\tilde{3},\tilde{4}),i}(t',t)\, G^{h}_{\mu,(\tilde{3},\tilde{4}),j}(t',t), \\ \Delta Q(t,t') &= \Delta Q_{\mathrm{HBT},1}(t,t') + \Delta Q_{\mathrm{HBT},2}(t,t') + \Delta Q_{\mathrm{HOM}}(t,t'). \end{aligned} \tag{B.8}$$

The Handbury-Brown-Twist contribution depend on interferences between $\phi_i(E)$ and the Fermi sea,

$$\Delta Q_{\mathrm{HBT},i}(t,t') = \sum_{\substack{j=1 \\ j\neq i}}^{4} \left[\Delta G^{e}_{(\tilde{3},\tilde{4}),i}(t',t)\, G^{h}_{\mu,(\tilde{3},\tilde{4}),j}(t',t) - \Delta G^{e^*}_{(\tilde{3},\tilde{4}),i}(t',t)\, G^{e}_{\mu,(\tilde{3},\tilde{4}),j}(t',t) \right].$$

The contribution of interest here, $\Delta Q_{\mathrm{HOM}}(t,t')$ only dependent on $\Delta G^{e/h}$ by

$$\Delta Q_{\mathrm{HOM}}(t,t') = -\left[\Delta G^{e^*}_{(\tilde{3},\tilde{4}),1}(t',t)\, \Delta G^{e}_{(\tilde{3},\tilde{4}),2}(t',t) + \Delta G^{e^*}_{(\tilde{3},\tilde{4}),2}(t',t)\, \Delta G^{e}_{(\tilde{3},\tilde{4}),1}(t',t) \right]. \tag{B.9}$$

B.1.3. Time-averaged HOM contribution

The time averaged quantity

$$\Delta \bar{Q}_{\mathrm{HOM}} = \frac{2}{T_M} \int_{-\infty}^{\infty} d\tau \int_{0}^{T_M} d\bar{t}\, \Delta Q_{\mathrm{HOM}}(\bar{t}+\tau, \bar{t}-\tau)$$

with $\Delta Q_{\mathrm{HOM}}(t,t')$ given by Eq. (B.9) can be simplified by inserting $\Delta G^{e/h}$ from Eq. (B.7):

$$\begin{aligned}
\Delta\bar{Q}_{\mathrm{HOM}} = -\frac{2}{T_M}\int_{-\infty}^{\infty} dt \int_{-\infty}^{\infty} dt' \Big[& \Delta G^{e^*}_{(\tilde{3},\tilde{4}),1}(t',t)\,\Delta G^{e}_{(\tilde{3},\tilde{4}),2}(t',t) \\
& + \Delta G^{e^*}_{(\tilde{3},\tilde{4}),2}(t',t)\,\Delta G^{e}_{(\tilde{3},\tilde{4}),1}(t',t)\Big] \\
= \frac{-2(2\pi)^2}{T_M}\int d\boldsymbol{E} \Big[& \phi_1^*(E)\phi_1(E')\phi_2^*(E'')\phi_2(E''')\delta(E-E''')\,\delta(E'-E'')\cdot \\
& S^*_{3,1}(E)S_{4,1}(E')S^*_{4,2}(E'')S_{3,2}(E''') \\
& + \phi_2^*(E)\phi_2(E')\phi_1^*(E'')\phi_1(E''')\delta(E-E''')\,\delta(E'-E'')\cdot \\
& S^*_{3,2}(E)S_{4,2}(E')S^*_{4,1}(E'')S_{3,1}(E''')\Big] \\
= \frac{-16\pi^2}{T_M}\,\mathrm{Re}\Big[& \int dE dE'\,\phi_1^*(E)\phi_2(E)\phi_1(E')\phi_2^*(E')\cdot \\
& S^*_{3,1}(E)S_{4,1}(E')S^*_{4,2}(E')S_{3,2}(E)\Big].
\end{aligned}$$

C. Third appendix: the quantum corral

C.1. Scattering phase of a circular potential well

The Hamiltonian

$$H = -\frac{\hbar^2}{2m^*}\left[\frac{\partial^2}{\partial\rho^2} + \rho^{-1}\frac{\partial}{\partial\rho} + \rho^{-2}\frac{\partial^2}{\partial\phi^2}\right] + V(\rho)$$

with a circular potential well of the form

$$V(\rho) = \begin{cases} a & \rho \leq R_{\text{ad}} \quad \hat{=} \text{ region I} \\ 0 & \rho > R_{\text{ad}} \quad \hat{=} \text{ region II.} \end{cases}$$

gives rise to a solution of the form $\psi(\rho,\phi) = \psi_{\phi,l}(\phi)\, R_l(\rho)$ with two different radial solutions for regions I, II:

$$R_l(\rho) = \begin{cases} c_I\, J_l(\tilde{k}\rho) & \text{for region I} \\ c_{1,II}\, J_l(k\rho) + c_{2,II}\, Y_l(k\rho) & \text{for region II,} \end{cases}$$

with

$$\tilde{k} = \sqrt{\frac{2m^*(E-a)}{\hbar^2}},$$
$$k = \sqrt{\frac{2m^*E}{\hbar^2}}.$$

Thereby we demand a normalizable wave function in both regions, such that for region I the Bessel function of second kind, $Y_l(\tilde{k}\rho)$ is excluded. The angular part is given by

$$\psi_{\phi,l}(\phi) = \frac{1}{\sqrt{2\pi}} e^{il\phi}$$

with $l \in \mathbb{Z}$. When introducing the scattering phase in the general solution,

$$R_l(\rho) = A_l\left(\cos\delta_l J_l(k\rho) - \sin\delta_l Y_l(k\rho)\right)$$

and logarithmic derivatives matching at the interface $\rho = R_{\text{ad}}$ results in

$$\tan\delta_l = \frac{J_l(kR_{\text{ad}})\, \partial_\rho J_l(\tilde{k}\rho)|_{\rho=R_{\text{ad}}} - J_l(\tilde{k}R_{\text{ad}})\, \partial_\rho J_l(\tilde{k}\rho)|_{\rho=R_{\text{ad}}}}{Y_l(\tilde{k}R_{\text{ad}})\, \partial_\rho J_l(k\rho)|_{\rho=R_{\text{ad}}} - J_l(kR_{\text{ad}})\, \partial_\rho Y_l(\tilde{k}\rho)|_{\rho=R_{\text{ad}}}}.$$

For $l = 0$ and using the derivatives $\partial_x J_0(x) = -J_1(x)$ and $\partial_x Y_0(x) = -Y_1(x)$, we achieve

$$\tan\delta_0 = \frac{-\tilde{k}J_0(kR_{\text{ad}})\, J_1(\tilde{k}R_{\text{ad}}) + kJ_1(kR_{\text{ad}})\, J_0(\tilde{k}R_{\text{ad}})}{-kJ_1(kR_{\text{ad}})\, Y_0(\tilde{k}R_{\text{ad}}) + \tilde{k}J_0(kR_{\text{ad}})\, Y_1(\tilde{k}R_{\text{ad}})}. \tag{C.1}$$

Bibliography

[1] C. K. Hong, Z. Y. Ou, and L. Mandel, "Measurement of subpicosecond time intervals between two photons by interference", Phys. Rev. Lett. **59**, 2044 (1987).

[2] F. Marquier, C. Sauvan, and J.-J. Greffet, "Revisiting Quantum Optics with Surface Plasmons and Plasmonic Resonators", ACS Photonics **4**, 2091 (2017).

[3] G. Fujii, T. Segawa, S. Mori, N. Namekata, D. Fukuda, and S. Inoue, "Preservation of photon indistinguishability after transmission through surface-plasmon-polariton waveguide", Opt. Lett. **37**, 1535 (2012).

[4] S. M. Wang, S. Y. Mu, C. Zhu, Y. X. Gong, P. Xu, H. Liu, T. Li, S. N. Zhu, and X. Zhang, "Hong-Ou-Mandel interference mediated by the magnetic plasmon waves in a three-dimensional optical metamaterial", Opt. Express **20**, 5213 (2012).

[5] R. W. Heeres, L. P. Kouwenhoven, and V. Zwiller, "Quantum interference in plasmonic circuits", Nature nanotechnology **8**, 719 (2013).

[6] K. Toyoda, R. Hiji, A. Noguchi, and S. Urabe, "Hong–Ou–Mandel interference of two phonons in trapped ions", Nature **527**, 74 (2015).

[7] A. M. Kaufman, B. J. Lester, C. M. Reynolds, M. L. Wall, M. Foss-Feig, K. R. A. Hazzard, A. M. Rey, and C. A. Regal, "Two-particle quantum interference in tunnel-coupled optical tweezers", Science **345**, 306 (2014).

[8] F. Bouchard, A. Sit, Y. Zhang, R. Fickler, F. M. Miatto, Y. Yao, F. Sciarrino, and E. Karimi, "Two-photon interference: the Hong–Ou–Mandel effect", Reports on Progress in Physics **84**, 012402 (2021).

[9] B. T. Gard, K. R. Motes, J. P. Olson, P. P. Rohde, and J. P. Dowling, "An introduction to boson-sampling", in "From atomic to mesoscale: The role of quantum coherence in systems of various complexities", pp. 167–192 (World Scientific, 2015).

[10] E. Bocquillon, V. Freulon, J.-M. Berroir, P. Degiovanni, B. Plaçais, A. Cavanna, Y. Jin, and G. Fève, "Coherence and Indistinguishability of Single Electrons Emitted by Independent Sources", Science **339**, 1054 (2013).

[11] M. V. Berry and M. Tabor, "Level clustering in the regular spectrum", Proceedings of the Royal Society of London. A. Mathematical and Physical Sciences **356**, 375 (1977).

[12] H. Makino and N. Minami, "E(K, L) level statistics of classically integrable quantum systems based on the Berry–Robnik approach", Progress of Theoretical and Experimental Physics **2014** (2014).

[13] T. Prosen and M. Robnik, "Intermediate statistics in the regime of mixed classical dynamics", Journal of Physics A: Mathematical and General **32**, 1863 (1999).

[14] M. V. Berry and M. Robnik, "Semiclassical level spacings when regular and chaotic orbits coexist", Journal of Physics A: Mathematical and General **17**, 2413 (1984).

[15] H. Makino and S. Tasaki, "Level spacing statistics of classically integrable systems: Investigation along the lines of the Berry-Robnik approach", Phys. Rev. E **67**, 066205 (2003).

[16] M. V. Berry, M. Tabor, and J. M. Ziman, "Level clustering in the regular spectrum", Proceedings of the Royal Society of London. A. Mathematical and Physical Sciences **356**, 375 (1977).

[17] F. Haake, *Quantum signatures of chaos*, Springer Series in Synergetics (Springer, Berlin, Germany, 2010), 3 edition.

[18] M. L. Mehta, *Random Matrices*, Pure and Applied Mathematics (Amsterdam) (Academic Press, San Diego, CA, 2004), 3 edition.

[19] H. L. Montgomery, "Pair correlation of zeros of the zeta function.", Journal für die reine und angewandte Mathematik (Crelles Journal) **24**, 181 (1973).

[20] F. J. Dyson, "The threefold way. Algebraic structure of symmetry groups and ensembles in quantum mechanics", Journal of Mathematical Physics **3**, 1199 (1962).

[21] C. W. J. Beenakker, "Random-matrix theory of Majorana fermions and topological superconductors", Reviews of Modern Physics **87**, 1037 (2015).

[22] J. P. Dahlhaus, B. Béri, and C. W. J. Beenakker, "Random-matrix theory of thermal conduction in superconducting quantum dots", Phys. Rev. B **82**, 014536 (2010).

[23] J.-D. Urbina, J. Kuipers, S. Matsumoto, Q. Hummel, and K. Richter, "Multiparticle Correlations in Mesoscopic Scattering: Boson Sampling, Birthday Paradox, and Hong-Ou-Mandel Profiles", Phys. Rev. Lett. **116**, 100401 (2016).

[24] R. A. Jalabert, H. U. Baranger, and A. D. Stone, "Conductance fluctuations in the ballistic regime: A probe of quantum chaos?", Phys. Rev. Lett. **65**, 2442 (1990).

[25] H. U. Baranger, R. A. Jalabert, and A. D. Stone, "Quantum-chaotic scattering effects in semiconductor microstructures", Chaos: An Interdisciplinary Journal of Nonlinear Science **3**, 665 (1993).

[26] M. C. Gutzwiller, *Chaos in classical and quantum mechanics*, volume 1 (Springer Science & Business Media, 2013).

[27] K. Richter and M. Sieber, "Semiclassical Theory of Chaotic Quantum Transport", Phys. Rev. Lett. **89**, 206801 (2002).

[28] M. Novaes, "Energy-dependent correlations in the S-matrix of chaotic systems", Journal of Mathematical Physics **57**, 122105 (2016).

[29] S. Müller, "Periodic-orbit approach to universality in quantum chaos", arXiv preprint nlin/0512058 (2005).

[30] S. Müller, S. Heusler, P. Braun, F. Haake, and A. Altland, "Semiclassical Foundation of Universality in Quantum Chaos", Phys. Rev. Lett. **93**, 014103 (2004).

[31] F. Wegner, "The mobility edge problem: continuous symmetry and a conjecture", Zeitschrift für Physik B Condensed Matter **35**, 207 (1979).

[32] K. Efetov, "Super-symmetry in Disorder and Chaos, Cambridge Univ", Press, Cambridge (1997).

[33] R. A. Smith, I. V. Lerner, and B. L. Altshuler, "Spectral statistics in disordered metals: A trajectories approach", Phys. Rev. B **58**, 10343 (1998).

[34] R. S. Whitney, I. V. Lerner, and R. A. Smith, "Can the trace formula describe weak localization?", Waves in Random Media **9**, 179 (1999).

[35] D. M. Eigler and E. K. Schweizer, "Positioning single atoms with a scanning tunnelling microscope", Nature **344**, 524 (1990).

[36] M. F. Crommie, C. P. Lutz, and D. M. Eigler, "Confinement of electrons to quantum corrals on a metal surface", Science **262**, 218 (1993).

[37] M. Crommie, C. Lutz, D. Eigler, and E. Heller, "Quantum corrals", Physica D: Nonlinear Phenomena **83**, 98 (1995).

[38] E. Heller, M. Crommie, C. Lutz, and D. Eigler, "Scattering and absorption of surface electron waves in quantum corrals", Nature **369**, 464 (1994).

[39] H. Manoharan, C. Lutz, and D. Eigler, "Quantum mirages formed by coherent projection of electronic structure", Nature **403**, 512 (2000).

[40] W. De Haas, J. De Boer, and G. Van den Berg, "The electrical resistance of gold, copper and lead at low temperatures", Physica **1**, 1115 (1934).

[41] D. Porras, J. Fernández-Rossier, and C. Tejedor, "Microscopic theory for quantum mirages in quantum corrals", Phys. Rev. B **63**, 155406 (2001).

[42] M. Weissmann and H. Bonadeo, "A simple interpretation of quantum mirages", Physica E: Low-dimensional Systems and Nanostructures **10**, 544 (2001).

[43] Z.-G. Fu, P. Zhang, Z. Wang, and S.-S. Li, "Quantum corrals and quantum mirages on the surface of a topological insulator", Phys. Rev. B **84**, 235438 (2011).

[44] G. A. Fiete and E. J. Heller, "Colloquium: Theory of quantum corrals and quantum mirages", Reviews of Modern Physics **75**, 933 (2003).

[45] R. Y. Ağcalı, B. Atik, E. Bilgen, B. Karlı, and M. F. Danışman, "Leading to a Better Understanding of the Particle-in-a-Quantum-Corral Model", Journal of Chemical Education **96**, 82 (2018).

[46] R. X. Cao, B. F. Miao, Z. F. Zhong, L. Sun, B. You, W. Zhang, D. Wu, A. Hu, S. D. Bader, and H. F. Ding, "Two-dimensional quantum diffusion of Gd adatoms in nano-size Fe corrals", Phys. Rev. B **87**, 085415 (2013).

[47] S. Freeney, S. Borman, J. Harteveld, and I. Swart, "Coupling quantum corrals to form artificial molecules", SciPost Phys. **9**, 85 (2020).

[48] R. W. Robinett, "Quantum mechanics of the two-dimensional circular billiard plus baffle system and half-integral angular momentum", European journal of physics **24**, 231 (2003).

[49] M. J. Kelly, R. E. Palmer, and S. Crampin, "Electron states in quantum corrals", Philosophical Transactions of the Royal Society of London. Series A: Mathematical, Physical and Engineering Sciences **362**, 1149 (2004).

[50] E. J. Heller, "Bound-state eigenfunctions of classically chaotic Hamiltonian systems: scars of periodic orbits", Phys. Rev. Lett. **53**, 1515 (1984).

[51] F. Stilp, A. Bereczuk, J. Berwanger, N. Mundigl, K. Richter, and F. J. Giessibl, "Very weak bonds to artificial atoms formed by quantum corrals", Science **372**, 1196 (2021).

[52] S. Müller, S. Heusler, P. Braun, and F. Haake, "Semiclassical approach to chaotic quantum transport", New Journal of Physics **9**, 12 (2007).

[53] A. Bereczuk, B. Dietz, J. Che, J. Kuipers, J.-D. Urbina, and K. Richter, "Universal S-matrix correlations for complex scattering of wave packets in noninteracting many-body systems: Theory, simulation, and experiment", Phys. Rev. E **103**, 052209 (2021).

[54] R. Landauer, "Electrical resistance of disordered one-dimensional lattices", Philosophical magazine **21**, 863 (1970).

[55] M. Büttiker, "Four-terminal phase-coherent conductance", Physical review letters **57**, 1761 (1986).

[56] E. Ott, *Chaos in dynamical systems* (Cambridge university press, 2002).

[57] P. Gaspard, S. Chaos, and S. Mechanics, *Cambridge Nonlinear Science Series* (Cambridge University Press, 1998).

[58] G. M. Zaslavsky, *The physics of chaos in Hamiltonian systems* (world scientific, 2007).

[59] H. U. Baranger and P. A. Mello, "Reflection symmetric ballistic microstructures: Quantum transport properties", Phys. Rev. B **54**, R14297 (1996).

[60] J. Kuipers, "Semiclassics for chaotic systems with tunnel barriers", Journal of Physics A: Mathematical and Theoretical **42**, 425101 (2009).

[61] T. E. O. Ericson, B. Dietz, and A. Richter, "Cross-section fluctuations in chaotic scattering systems", Phys. Rev. E **94**, 042207 (2016).

[62] J. Kuipers, personal communication (Nov. 2019).

[63] P. Jacquod and R. S. Whitney, "Semiclassical theory of quantum chaotic transport: Phase-space splitting, coherent backscattering, and weak localization", Phys. Rev. B **73**, 195115 (2006).

[64] R. S. Whitney, "Suppression of weak localization and enhancement of noise by tunneling in semiclassical chaotic transport", Phys. Rev. B **75**, 235404 (2007).

[65] E. T. Copson, *Asymptotic Expansions*, Cambridge Tracts in Mathematics (Cambridge University Press, 1965).

[66] R. Wong, "I - Fundamental Concepts of Asymptotics", in R. Wong (ed.), "Asymptotic Approximations of Integrals", pp. 1–54 (Academic Press, 1989).

[67] G. Berkolaiko and J. Kuipers, "Universality in chaotic quantum transport: The concordance between random-matrix and semiclassical theories", Physical Review E **85**, 045201 (2012).

[68] S. Datta, *Electronic Transport in Mesoscopic Systems*, Cambridge Studies in Semiconductor Physics and Microelectronic Engineering (Cambridge University Press, 1995).

[69] P. Reck, *Quantum Echoes and revivals in two-band systems and Bose-Einstein condensates*, Ph.D. thesis, University Regensburg (2018).

[70] E. Akkermans and G. Montambaux, *Mesoscopic physics of electrons and photons* (Cambridge University Press, Cambridge, England, 2010).

[71] C. Gorini, personal communication (2018).

[72] C. W. Groth, M. Wimmer, A. R. Akhmerov, and X. Waintal, "Kwant: a software package for quantum transport", New J. Phys. **16**, 063065 (2014).

[73] D. Agassi, "The statistical theory of nuclear reactions for strongly overlapping resonances as a theory of transport phenomena", Physics Reports **22**, 145 (1975).

[74] B. Dietz, T. Friedrich, H. L. Harney, M. Miski-Oglu, A. Richter, F. Schäfer, and H. A. Weidenmüller, "Quantum chaotic scattering in microwave resonators", Phys. Rev. E **81**, 036205 (2010).

[75] Y. V. Fyodorov, D. V. Savin, and H.-J. Sommers, "Scattering, reflection and impedance of waves in chaotic and disordered systems with absorption", Journal of Physics A: Mathematical and General **38**, 10731 (2005).

[76] A. Nock, S. Kumar, H.-J. Sommers, and T. Guhr, "Distributions of off-diagonal scattering matrix elements: Exact results", Annals of Physics **342**, 103 (2014).

[77] T. Ericson, "Fluctuations of nuclear cross sections in the continuum region", Phys. Rev. Lett. **5**, 430 (1960).

[78] S. Kumar, A. Nock, H.-J. Sommers, T. Guhr, B. Dietz, M. Miski-Oglu, A. Richter, and F. Schäfer, "Distribution of Scattering Matrix Elements in Quantum Chaotic Scattering", Phys. Rev. Lett. **111**, 030403 (2013).

[79] E. Davis and D. Boosé, "On the variance of the fluctuating cross section", Phys. Lett. B **211**, 379 (1988).

[80] E. Davis and D. Boosé, "Higher moments of the fluctuating S-matrix within the stochastic model for compound-nucleus scattering", Zeitschrift für Physik A Atomic Nuclei **332**, 427 (1989).

[81] B. Dietz, H. Harney, A. Richter, F. Schäfer, and H. Weidenmüller, "Cross-section fluctuations in chaotic scattering", Phys. Lett. B **685**, 263 (2010).

[82] T. Kottos and U. Smilansky, "Periodic Orbit Theory and Spectral Statistics for Quantum Graphs", Annals of Physics **274**, 76 (1999).

[83] O. Bohigas, M.-J. Giannoni, and C. Schmit, "Characterization of chaotic quantum spectra and universality of level fluctuation laws", Phys. Rev. Lett. **52**, 1 (1984).

[84] A. Richter, "Playing billiards with microwaves—quantum manifestations of classical chaos", in "Emerging Applications of Number Theory", pp. 479–523 (Springer, 1999).

[85] H. Stöckmann, "Microwave billiards and quantum chaos", Scholarpedia **5**, 10243 (2010), revision #127194.

[86] B. Dietz and A. Richter, "Quantum and wave dynamical chaos in superconducting microwave billiards", Chaos: An Interdisciplinary Journal of Nonlinear Science **25**, 097601 (2015).

[87] C. Grenier, R. Hervé, G. Fève, and P. Degiovanni, "Electron Quantum Optics in quantum Hall edge channels", Modern Physics Letters B **25**, 1053 (2011).

[88] E. Bocquillon, V. Freulon, F. D. Parmentier, J.-M. Berroir, B. Plaçais, C. Wahl, J. Rech, T. Jonckheere, T. Martin, C. Grenier, D. Ferraro, P. Degiovanni, and G. Fève, "Electron quantum optics in ballistic chiral conductors", Annalen der Physik **526**, 1 (2014).

[89] A. Yar, "Quantum chaos dynamics on the surface of topological insulator attached to spiral multiferroic oxide in a magnetic field", Phys. Lett. A **387**, 127037 (2021).

[90] B. A. Bernevig, T. L. Hughes, and S.-C. Zhang, "Quantum Spin Hall Effect and Topological Phase Transition in HgTe Quantum Wells", Science **314**, 1757 (2006).

[91] C. Grenier, *Electronic quantum optics*, Theses, Ecole normale supérieure de lyon - ENS Lyon (2011).

[92] E. Bocquillon, *Electron quantum optics in quantum Hall edge channels*, Theses, Université Pierre et Marie Curie - Paris VI (2012).

[93] M. König, H. Buhmann, L. W. Molenkamp, T. Hughes, C.-X. Liu, X.-L. Qi, and S.-C. Zhang, "The quantum spin Hall effect: theory and experiment", Journal of the Physical Society of Japan **77**, 031007 (2008).

[94] B. Zhou, H.-Z. Lu, R.-L. Chu, S.-Q. Shen, and Q. Niu, "Finite Size Effects on Helical Edge States in a Quantum Spin-Hall System", Phys. Rev. Lett. **101**, 246807 (2008).

[95] S. Essert, *Mesoscopic Transport in Topological Insulator Nanostructures*, Theses (2016).

[96] E. P. Wigner, "Über die Operation der Zeitumkehr in der Quantenmechanik", in "The Collected Works of Eugene Paul Wigner", pp. 213–226 (Springer, 1993).

[97] H. A. Kramers, "Théorie générale de la rotation paramagnétique dans les cristaux", Proc. Acad. Amst **33** (1930).

[98] A. Szafer and A. D. Stone, "Theory of quantum conduction through a constriction", Phys. Rev. Lett. **62**, 300 (1989).

[99] C. Gorini, R. A. Jalabert, W. Szewc, S. Tomsovic, and D. Weinmann, "Theory of scanning gate microscopy", Phys. Rev. B **88**, 035406 (2013).

[100] C. Rouvinez and U. Smilansky, "A scattering approach to the quantization of Hamiltonians in two dimensions-application to the wedge billiard", Journal of Physics A: Mathematical and General **28**, 77 (1995).

[101] P. F. Bagwell, "Evanescent modes and scattering in quasi-one-dimensional wires", Phys. Rev. B **41**, 10354 (1990).

[102] E. Doron and U. Smilansky, "Semiclassical quantization of chaotic billiards: a scattering theory approach", Nonlinearity **5**, 1055 (1992).

[103] H. Schanz and U. Smilansky, "Quantization of Sinai's billiard—A scattering approach", Chaos, Solitons & Fractals **5**, 1289 (1995).

[104] A. Marguerite, *Two-particle interferometry for quantum signal processing*, Theses, Université Pierre et Marie Curie - Paris VI (2017).

[105] E. Bocquillon, V. Freulon, F. D. Parmentier, J. M. Berroir, B. Plaçais, C. Wahl, J. Rech, T. Jonckheere, T. Martin, C. Grenier, D. Ferraro, P. Degiovanni, and G. Fève, "Electron quantum optics in ballistic chiral conductors", Annalen der Physik **526**, 1 (2014).

[106] A. Marguerite, E. Bocquillon, J.-M. Berroir, B. Plaçais, A. Cavanna, Y. Jin, P. Degiovanni, and G. Fève, "Two-particle interferometry in quantum Hall edge channels", physica status solidi (b) **254**, 1600618 (2017).

[107] I. C. Fulga, F. Hassler, and A. R. Akhmerov, "Scattering theory of topological insulators and superconductors", Phys. Rev. B **85**, 165409 (2012).

[108] F. Mezzadri, "How to generate random matrices from the classical compact groups", arXiv (2006).

[109] C. W. J. Beenakker, "Random-matrix theory of quantum transport", Rev. Mod. Phys. **69**, 731 (1997).

[110] J. Bolte and S. Keppeler, "Semiclassical form factor for chaotic systems with spin $\frac{1}{2}$", Journal of Physics A: Mathematical and General **32**, 8863 (1999).

[111] O. Zaitsev, D. Frustaglia, and K. Richter, "Semiclassical theory of weak antilocalization and spin relaxation in ballistic quantum dots", Phys. Rev. B **72**, 155325 (2005).

[112] J. Bolte and D. Waltner, "Semiclassical theory of ballistic transport through chaotic cavities with spin-orbit interaction", Phys. Rev. B **76**, 075330 (2007).

[113] M. Crommie, C. Lutz, D. Eigler, and E. Heller, "Quantum interference in 2D atomic-scale structures", Surface Science **361-362**, 864 (1996).

[114] B. Donner, M. Kleber, C. Bracher, and H. J. Kreuzer, "A simple method for simulating scanning tunneling images", American Journal of Physics **73**, 690 (2005).

[115] B. Donner, *Simulation of quantum corrals*, Dissertation, Technische Universität München, München (2004).

[116] J. A. Stroscio and D. M. Eigler, "Atomic and Molecular Manipulation with the Scanning Tunneling Microscope", Science **254**, 1319 (1991).

[117] G. Binnig, H. Rohrer, C. Gerber, and E. Weibel, "Surface Studies by Scanning Tunneling Microscopy", Phys. Rev. Lett. **49**, 57 (1982).

[118] S. G. Davison and M. Stęślicka, *Basic theory of surface states*, volume 46 (Oxford University Press, 1992).

[119] F. J. Giessibl, "High-speed force sensor for force microscopy and profilometry utilizing a quartz tuning fork", Applied Physics Letters **73**, 3956 (1998).

[120] F. J. Giessibl, "The qPlus sensor, a powerful core for the atomic force microscope", Review of Scientific Instruments **90**, 011101 (2019).

[121] F. J. Giessibl, "A direct method to calculate tip–sample forces from frequency shifts in frequency-modulation atomic force microscopy", Applied Physics Letters **78**, 123 (2001).

[122] L. Gross, F. Mohn, N. Moll, P. Liljeroth, and G. Meyer, "The Chemical Structure of a Molecule Resolved by Atomic Force Microscopy", Science **325**, 1110 (2009).

[123] N. Moll, L. Gross, F. Mohn, A. Curioni, and G. Meyer, "The mechanisms underlying the enhanced resolution of atomic force microscopy with functionalized tips", New J. Phys. **12**, 125020 (2010).

[124] C. J. Chen, *Introduction to Scanning Tunneling Microscopy* (Oxford University Press, 2007).

[125] F. J. Giessibl, "Advances in atomic force microscopy", Rev. Mod. Phys. **75**, 949 (2003).

[126] W. Lawrence and B. Bragg, "XLII. The crystalline structure of copper", The London, Edinburgh, and Dublin Philosophical Magazine and Journal of Science **28**, 355 (1914).

[127] S. Kevan, "Evidence for a new broadening mechanism in angle-resolved photoemission from Cu (111)", Phys. Rev. Lett. **50**, 526 (1983).

[128] W. Shockley, "On the Surface States Associated with a Periodic Potential", Phys. Rev. **56**, 317 (1939).

[129] P. O. Gartland, S. Berge, and B. J. Slagsvold, "Photoelectric Work Function of a Copper Single Crystal for the (100), (110), (111), and (112) Faces", Phys. Rev. Lett. **28**, 738 (1972).

[130] R. Haberman, *Applied Partial Differential Equations - With Fourier Series and Boundary Value Problems* (Pearson Prentice Hall, New Jersey, 2004), fourth edition.

[131] I. S. Gradshteyn and I. M. Ryzhik, *Table of integrals, series, and products* (Academic press, 2014).

[132] M. J. Kelly, R. E. Palmer, and S. Crampin, "Electron states in quantum corrals", Philosophical Transactions of the Royal Society of London. Series A: Mathematical, Physical and Engineering Sciences **362**, 1149 (2004).

[133] M. Weiß, *Tunnelspektroskopie an einem Kohlenstoffmonoxid-Quantum-Corral*, Master's thesis, Universität Regensburg (2021).

[134] P. G. Averbuch, "Zero energy divergence of scattering cross sections in two dimensions", J. Phys. A **19**, 2325 (1986).

[135] S. Hunklinger, *Festkörperphysik* (De Gruyter Oldenbourg, 2017).

[136] F. Stilp, *Untersuchung der Eigenzustände eines Quantum Corrals aus Eisen-Adatomen auf Cu(111) mittels kombinierter Rasterkraft- und Rastertunnelmikroskopie*, Master's thesis, Universität Regensburg (2021).

[137] J. Lennard-Jones, "Processes of adsorption and diffusion on solid surfaces", Transactions of the Faraday Society **28**, 333 (1932).

[138] F. Huber, J. Berwanger, S. Polesya, S. Mankovsky, H. Ebert, and F. J. Giessibl, "Chemical bond formation showing a transition from physisorption to chemisorption", Science **366**, 235 (2019).

[139] M. Ternes, C. González, C. P. Lutz, P. Hapala, F. J. Giessibl, P. Jelínek, and A. J. Heinrich, "Interplay of conductance, force, and structural change in metallic point contacts", Phys. Rev. Lett. **106**, 016802 (2011).

[140] L. Gross, F. Mohn, N. Moll, P. Liljeroth, and G. Meyer, "The chemical structure of a molecule resolved by atomic force microscopy", Science **325**, 1110 (2009).

[141] N. Moll, L. Gross, F. Mohn, A. Curioni, and G. Meyer, "The mechanisms underlying the enhanced resolution of atomic force microscopy with functionalized tips", New J. Phys. **12**, 125020 (2010).

[142] N. Moll, L. Gross, F. Mohn, A. Curioni, and G. Meyer, "A simple model of molecular imaging with noncontact atomic force microscopy", New J. Phys. **14**, 083023 (2012).

[143] J. Berwanger, S. Polesya, S. Mankovsky, H. Ebert, and F. J. Giessibl, "Atomically Resolved Chemical Reactivity of Small Fe Clusters", Phys. Rev. Lett. **124**, 096001 (2020).

[144] M. Schneiderbauer, M. Emmrich, A. J. Weymouth, and F. J. Giessibl, "CO tip functionalization inverts atomic force microscopy contrast via short-range electrostatic forces", Phys. Rev. Lett. **112**, 166102 (2014).

[145] B. Cordero, V. Gómez, A. E. Platero-Prats, M. Revés, J. Echeverría, E. Cremades, F. Barragán, and S. Alvarez, "Covalent radii revisited", Dalton Trans. pp. 2832–2838 (2008).

[146] R. P. Feynman, R. B. Leighton, and M. Sands, "The Feynman Lectures on Physics. Vol. II.", (1963).

[147] A. Zangwill, *Physics at surfaces* (Cambridge university press, 1988).

[148] N. D. Lang and W. Kohn, "Theory of Metal Surfaces: Charge Density and Surface Energy", Phys. Rev. B **1**, 4555 (1970).

[149] M. Ellner, N. Pavliček, P. Pou, B. Schuler, N. Moll, G. Meyer, L. Gross, and R. Peréz, "The Electric Field of CO Tips and Its Relevance for Atomic Force Microscopy", Nano Letters **16**, 1974 (2016), pMID: 26840626.

[150] P. Kurzweil, *Chemische Bindung, Werkstoffe, Struktur*, pp. 69–114 (Springer Fachmedien Wiesbaden, Wiesbaden, 2020).

[151] T. A. Albright, J. K. Burdett, and M.-H. Whangbo, *Orbital interactions in chemistry* (John Wiley & Sons, Ltd, 2013).

[152] R. A. Evarestov, *Quantum Chemistry of Solids - LCAO Treatment of Crystals and Nanostructures* (Springer Science & Business Media, Berlin Heidelberg, 2013).

[153] M. Steinau, *Chemical bonding between artificial atom and AFM tip - an LCAO approach*, Master's thesis, Universität Regensburg (2022).

[154] A. L. Fetter and J. D. Walecka, *Quantum Theory of Many-Particle Systems* (McGraw-Hill, Boston, 1971).

[155] G.-C. Wick, "The evaluation of the collision matrix", Phys. Rev. **80**, 268 (1950).

List of publications:

- Bereczuk, A., Dietz, B., Che, J., Kuipers, J., Urbina, J. D., Richter, K "Universal S-matrix correlations for complex scattering of wave packets in non-interacting many-body systems: Theory, simulation, and experiment." Phys. Rev. E **103**, 052209 (2021)
- Stilp, F., Bereczuk, A., Berwanger, J., Mundigl, N., Richter, K., Giessibl, F. J. "Very weak bonds to artificial atoms formed by quantum corrals." Science **372**, 1196 (2021).

Acknowledgments

Several different persons have supported me on the way to my dissertation on a bright range of levels:

First, I want to thank Prof. Dr. Klaus Richter who has given me the opportunity of working in this research group. Owing to him, the atmosphere of the group is friendly and open minded, such that working their was highly enjoyable.
Furthermore, I want to thank apl. Prof. Dr. Juan Diego Urbina for being my supervisor and motivator. It was a pleasure to spend time at the black board with him discussing physics. Special thanks for his kindness, warmth and his attention to the overall social balance. I appreciated that despite his position level, he was always very approachable. For his patient kind of teaching me the semiclassical technique of computing S-matrix correlations thanks to Jack Kuipers.
Thanks to Prof. Dr. Franz J. Gießibl for the opportunity to study quantum corrals. This topic provides pleasant patterns, every time when computing the LDOS. In company with Prof. Dr. Franz J. Gießibl, Fabian Stilp, Julian Berwanger, Martin Steinau and Marco Weiss I enjoyed the discussions on experiments and the transfer to a theoretical model.
The support which I received when doing the research meanwhile raising two kids in sometimes tough ambience is not taken for granted, therefor I want to thank Prof. Dr. Klaus Richter, apl. Prof. Dr. Juan Diego Urbina and Doris Meier. Every cup of coffee is much more enjoyable when drinking it with this respectable colleagues.
Many thanks to Camilo Alfonso Moreno Jaimes, Micheal Barth and Vanessa Junk for proofreading of the thesis combined with enjoyable conversations.
Concerning private relations, the backbone of my support is build by my parents-in-law as the best and spontaneous day nannies, my parents and my brother, which believed in my physics study before I even thought about studying and finally my own small family, which is the greatest fortune I am pleased with. Kerstin, Marie and Maximilian, thanks for withstanding these stressful times.